Tourmaline of the Kragerø pegmatites

The source of boron and its implication for the melt formation of Sveconorwegian pegmatites

Erika De La Cruz

Master Thesis in Geosciences
Mineralogy, Petrology and Geochemistry programme
60 credits

Department of Geosciences
and
Natural History Museum

UNIVERSITY OF OSLO

June 2021

Tourmaline of the Kragerø pegmatites

The source of boron and its implication for the melt formation of Sveconorwegian pegmatites

Erika De La Cruz

Tourmaline of the Kragerø pegmatites.

The source of boron and its implication for the melt formation of Sveconorwegian pegmatites

http://www.duo.uio.no/

Abstract

In the Kragerø area in South Norway, tourmaline is commonly found in Sveconorwegian Nb-Y-F pegmatites. In general, magmatic tourmaline is rare in Nb-Y-F pegmatites. The local tourmaline enrichment in the Kragerø pegmatites, and consequently, the origin of Boron is under debate, since the Sveconorwegian basement is poor in B elsewhere. The tourmalines from the following pegmatites were investigated: (1) from the Bamble sector, the Kragerø pegmatites: Lindvikskollen, Tangen, Dalane and Havredal; and the (2) Ramfoss and (3) Spro pegmatites, from the Kongsberg Sector and Idefjorden 'Terrane', respectively. The Lindvikskollen pegmatite area was the focus of field work and sampling of rocks and tourmalines. Additional tourmaline samples were provided by the Natural History Museum of the University of Oslo. The methodologies used included whole-rock analysis, scanning electron microscopy (SEM), electron probe microanalysis (EPMA), laser ablation inductively coupled plasma mass spectrometry (LA-ICP-MS) and secondary ion mass spectrometry (SIMS).

The Kragerø pegmatites (which occur a few km apart from each other) have different B isotope signatures, which hints to separate melt sources. Because a common melt source of the Kragerø pegmatites can be excluded, it is suggested that they formed by local partial melting. This conclusion is supported by the fact that no granite pluton with similar ages to the pegmatites is exposed in the area. In the case of the Lindvikskollen pegmatite, which intruded a metagabbro body and its albitized parts, tourmaline and bulk rock chemistry indicates that the pegmatite was probably formed by mixed partial melting of its metagabbro and albitite host rocks. In addition, the nearby Tangen pegmatite intrudes the same metagabbro, and its overlapping $\delta^{11}B$ data with the Lindvikskollen tourmaline indicates that they share a common source. The Dalane and Havredal tourmalines, are most likely the result of partial melting of their metasedimentary host rocks, amphibolites and gneisses. The Ramfoss tourmalines show affinity to carbonates, which can be found in calcite veins that infiltrated the area's rocks. The Spro tourmaline chemical and isotopic compositions point to their host rock tourmaline-bearing gneiss to be the pegmatite melt source.

This thesis concludes that the source of B of the investigated pegmatites originated by low degree partial melting of their respective host rocks, which contain B-bearing minerals (borosilicates and micas) in addition to the fractional crystallization of the melt under conditions that increased the tourmaline stability range.

Acknowledgements

I wish to show my gratitude to my main supervisor Axel Müller for his continuous guidance, encouragement, and valuable discussions. I also want to thank my co-supervisor Tom Andersen for his advice, help with geochemical data, and insightful feedback.

To everyone at the National History Museum, I want to show my appreciation for their support and for making me feel welcomed. Especially Nélia Castro for her help and instruction in performing SEM/EDS analyses.

I would like to acknowledge the support of the Department of Geoscience of the University of Oslo. Thanks to Muriel Erambert for her assistance with the EPMA and subsequent data analysis. I would like to show my appreciation to Gunborg Bye Fjeld, for her help and guidance with the preparation of the bulk rock samples. Thanks to Salahalldin Akhavan for the preparation of the thick sections as well as the polishing of the epoxy casts. Lastly, I want to express my gratitude to Magnus Kristoffersen for his assistance and instruction with the LA-ICP-MS analyses and data handling.

I wish to extend my thanks to Robert Trumbull at the GFZ (German Research Centre for Geosciences) in Potsdam, Germany, for the SIMS Boron isotope analysis, his comments, and suggestions.

In addition, I want to thank the Activation Labs in Canada, for performing the whole-rock ICP-MS analyses.

In a more personal note, I want to thank my dear friends, Diana da Silva and João Fernandes for many discussions, help and emotional support. Finally, I want to thank my family for their constant optimism, encouragement, and for being my main source of motivation.

Contents

List of Figures

List of Tables

Preface

This thesis is submitted to the Department of Geosciences, University of Oslo (UiO), for the degree of Master of Science in Geosciences, within the Mineralogy, Petrology and Geochemistry programme.

This thesis was supervised by Axel Müller and Tom Andersen and developed in collaboration with Natural History Museum of the University of Oslo from January 2020 to June 2021.

List of Abbreviations

Alb. – Albitite

ASI – Alumina Saturation Index

apfu – atoms per formula unit

A.M. – Analysis Method

BBe – Boron – Beryllium

BSE – Backscattered Electrons

EMPA – Electron Microprobe Analysis

EPMA – Electron Probe Microanalysis

fO_2 – Oxygen fugacity

FUS-ISE – Fusion/Ion Selective Electrode

FUS-MS-Na_2O_2 – Sodium Peroxide Fusion/Inductive Coupled Plasma Mass Spectrometry

FUS-Na_2O_2 – Sodium Peroxide Fusion/Inductive Coupled Plasma

FUS-XRF – Fusion/X-ray Fluorescence

Gn. – Gneiss

Gr – Granite

HP – High-Pressure

HREE – Heavy Rare Earth Elements

HT –High-Temperature

ICP – Inductive Coupled Plasma

ICP-MS – Inductive Coupled Plasma Mass Spectrometry

ICP-OES – Inductive Coupled Plasma Optical Emission Spectrometry

IMA-CNMNC – International Mineralogy Association's Commission on New Minerals, Nomenclature and Classification

IMF – Initial Mass Function

Inter. – Intermediate

L. – Lindvikskollen

LA-ICP-MS – Laser Ablation Inductively Coupled Plasma Mass Spectrometry

LCT – Lithium-Cesium-tantalum

Lind. – Lindvikskollen

LOI – Loss in Ignition

LOD –Limits of Detection

LREE – Light Rare Earth Elements

LT – Low-Temperature

MG – Metagabbro

MORB – Mid-Ocean Ridge Basalts

MP – Moderate-Pressure

n – number of analyses

NIST SRM – National Institute of Standards and Technology, Standard Reference Material

NYF – Niobium-Yttrium-Fluorine

P – Pressure

P-T –Pressure-Temperature

REE – Rare Earth Elements

SD – Standard deviation

SE – Secondary Electrons

SEM – Scanning Electron Microscopy / Microscope

SIMS – Secondary Ion Mass Spectrometry

SMB – Sirdal Magmatic Belt

SRM – Standard Reference Material

T – Temperature

TAS – Total Alkali vs SiO_2

TIB – Transcandinavian Igneous Belt

Tour – Tourmaline-bearing

Tur – Tourmaline

UCC – Upper Continental Crust

UHP – Ultra-High-Pressure

UHT – Ultra-High-Temperature

XAl – Aluminium apfu allocated to the X-site

XRF – X-ray fluorescence

Xvac – X-site vacancy

Z. – Zone

1. Introduction

Tourmaline is a boron-silicate with a complex chemical composition of major and trace elements. Its flexible chemistry changes depending on the host environment giving it an outstanding stability range with regards to pressure, temperature, fluid, and host rock composition. This makes tourmaline a great indicator of its forming environment, and even as a mean to determine the origin of its source rocks.

Tourmaline is a major reservoir of B in the Earth's crust and a crucial component in the boron cycle (*e.g.,* van Hinsberg *et al.,* 2011b). Boron is scarce in the Earth, the continental crust being the richest domain in B with 17 ppm on average (Rudnick & Gao, 2003). That explains why tourmaline mostly occurs as an accessory mineral in all rock types despite its great stability range and flexible chemical structure. Nevertheless, tourmaline can occur in significant amounts in some igneous rocks due to the strongly incompatible behaviour of B in igneous systems, thus highly evolved melts are rich in B (*e.g.*, Dutrow & Henry, 2011; London, 2016). Consequently, an abundance of tourmaline in igneous rock is indicative of substantial chemical melt fractionation, as is the case with granitic pegmatites.

The vast array of major and trace elements in tourmaline are excellent tools in isotope geochemistry. Tourmaline isotopic data offers another source of information about its origin, melt source, formation conditions, rock-fluid interactions, fluid sources and evolution, etc. Among different isotope systems that are commonly applied in tourmaline studies, the B stable isotopes are the focus of this thesis. The stable B isotopes are ^{10}B and ^{11}B, and their ratio is expressed as permil (‰) $\delta^{11}B$ values, calculated relative to the standard SRM 951 (Catanzaro, 1970; Leeman & Tonarini, 2001). Tourmaline has a range of $\delta^{11}B$ values of ~ 60‰ in natural rocks: tourmalines produced in subduction zone environments have a heavier B composition (high $\delta^{11}B$ values) than tourmalines formed in and around granites (low $\delta^{11}B$ values). This difference in B isotope ratios means that geological settings and reservoirs have unique B isotopic signatures (Barth, 1993; Marschall & Jiang, 2011) which can be used to learn more about the origin and evolution of tourmaline-bearing rocks.

Tourmaline is a common and locally abundant mineral in granitic pegmatites. Pegmatites are rare, small (< 0.5 km^3) silica-rich rock bodies crystallized from melt. They have a great range

of crystal sizes (> 2 cm), although they are more recognized by their gigantic-sized textures and strong enrichment in rare elements, such as Li, Ta, Be, and REE. Worldwide, pegmatites are also recognized as a major source of gemstones, including tourmalines, for example the Borborema pegmatite province in Brazil (*e.g.*, Beurlen *et al.*, 2011) and the Oxford County pegmatite field in Maine, USA (*e.g.*, Simmons *et al.*, 2005a).

It is important to note that the term "granitic pegmatite" is a definition of its composition rather than being related to its formation. The conventional model of pegmatite genesis implies that the bulk of pegmatite bodies encountered worldwide represent residual melts derived by fractionation of a large felsic pluton. Since this is the traditional model, historically, most studies and pegmatite classifications have been based on this type of pegmatites. However, recent studies revealed that many pegmatite provinces worldwide are directly formed by partial melting and are not derived from granites (*e.g.*, Konzett *et al.*, 2018; Müller *et al.*, 2017; Webber *et al.*, 2019).

Pegmatites can be classified into two families (Černý, 1991a; Černý & Ercit, 2005): (1) Lithium-Cesium-tantalum (LCT) pegmatites, these are more abundant and are related to S-type granites (Chappell & White, 2001), although not exclusively. (2) Niobium-Yttrium-Fluorine (NYF) pegmatites, these are associated to mainly A-type granites (Collins *et al.*, 1982). Tourmaline occurs quite frequently in LCT pegmatites, whereas it is rare in NYF pegmatites (London, 2008).

In the Kragerø area in south Norway, tourmaline is, however, commonly found in NYF pegmatites. These pegmatites belong to the Sveconorwegian Pegmatite Province, which was emplaced during the Sveconorwegian orogenesis (1140-920 Ma). The province hosts over 5000 pegmatite bodies, making it one of the largest pegmatite clusters in the world. In general, they are classified as abyssal or barren pegmatites and rare-metal pegmatites with NYF-affinity (Müller *et al.*, 2017). The pegmatites of the Kragerø area are located in the tectonometamorphic domain of the Bamble Sector, which has the highest density of pegmatites occurrences within the orogen beside the Evje-Iveland in the Rogaland-Hardanger-Telemark Sector and Østfold area in the Idefjorden 'Terrane'. The local enrichment of tourmaline in the Kragerø pegmatites and the origin of B in the pegmatite melt are still under debate because the Sveconorwegian metamorphic basement is poor in B elsewhere (Bast *et al.*, 2014; Engvik *et al.*, 2011).

1.1. Major and specific aims of the study

The major aim of this thesis is to use the chemistry of tourmalines of the Kragerø pegmatites: Lindvikskollen, Tangen, Dalane and Havredal pegmatites; and of two other localities of the Sveconorwegian orogen: the Ramfoss and Spro pegmatites, from the Kongsberg Sector and Idefjorden 'Terrane', respectively, to better understand the origin and formation of pegmatite melts. The specific aims of this thesis are:

(1) To investigate the mineral paragenesis and the zoning of the Lindvikskollen pegmatite.

(2) To map the Lindvikskollen area near Kragerø in detail to determine the extension of the Lindvikskollen pegmatite and its relation to the different host rock types.

(3) To determine the bulk rock chemistry of the Lindvikskollen pegmatite, its host rocks and associated lithologies.

(4) To determine the major and trace element chemistry and B isotope signature of tourmalines of the Kragerø pegmatites.

(5) To determine the major and trace element chemistry and B isotope signature of tourmalines of other Sveconorwegian pegmatites, namely from the Ramfoss and Spro pegmatites.

(6) To determine the variation in tourmaline chemistry with relation to the zoning and chemical evolution of the Lindvikskollen pegmatite.

(7) To utilize the results of tourmaline chemistry and isotopic investigations to better understand the origin of B and the genesis of the Kragerø pegmatites.

(8) To interpret the geochemical results of the investigated tourmalines in order to reveal the possible melt source of their pegmatite.

To achieve these aims an array of methods was used including optical microscopy, inductive coupled plasma (ICP) whole-rock analysis, scanning electron microscopy (SEM), electron probe microanalysis (EPMA), laser ablation inductively coupled plasma mass spectrometry (LA-ICP-MS) and secondary ion mass spectrometry (SIMS). The field work was concentrated in the Lindvikskollen pegmatite area, where bulk rock samples of the pegmatite, host

rocks, and tourmalines were collected. Additional tourmaline samples were provided by the Natural History Museum (NHM) of the University of Oslo.

1.2. Structure of the thesis

This thesis is divided in ten main chapters:

Chapter 1: General introduction of the subjects of the study, aims and structure of the thesis.

Chapter 2: Pegmatite theory, explaining concepts regarding pegmatite composition, origin, and classification.

Chapter 3: Tourmaline theory, describing its chemistry, mineralogy, crystallography, classification, and formation conditions.

Chapter 4: Boron theory, explaining the occurrence of B in the Earth's crust, B enrichment processes, and its isotope chemistry.

Chapter 5: General description of the Sveconorwegian orogeny, with special attention to the Bamble Sector.

Chapter 6: Description of the Sveconorwegian pegmatite province, with emphasis on the investigated pegmatites.

Chapter 7: Methodology section, listing the samples investigated, and describing the process of sample preparation and analytical methods performed.

Chapter 8: Fieldwork descriptions, map, and cross-section, as well as the results of the analytical methods.

Chapter 9: Discussion of the results in the context of the origin of tourmaline, and B, in the investigated pegmatites and host rocks.

Chapter 10: Main conclusions of the thesis, and suggestions for further studies.

2. Pegmatites

Pegmatites are very coarse-grained igneous rocks that can occur as zoned or homogenous bodies, they usually have a granitic composition and host significant amounts of rare elements. These rocks possess a great range of grain sizes but are more recognized by their gigantic crystals. Thus, pegmatites are defined more by their textural attributes than by their composition.

Most commonly the term pegmatite refers to granitic pegmatites and is synonymous with a rock of overall granitic composition. Both terms are used interchangeably, except when used with a modifier (*e.g.*, gabbroic pegmatite). Granitic pegmatites are the most common (Jahns & Tuttle, 1963; Norton, 1966), even so pegmatites that reflect the compositions of ultramafic, mafic, syenitic and carbonatitic igneous rocks exist but are less abundant.

These rocks host a remarkable range of economic commodities for which they are explored: feldspar for the glass industry and ceramic industry; quartz, for the glass and electronic industry; as well as more exotic elements that are mined for applications in electronics, aerospace, and many other specialized industries. A great interest on pegmatites also arises from the occurrence of gem-quality mineral specimens.

2.1. Composition, textures, and internal zonation of pegmatites

Generally, pegmatites consist of three major minerals: quartz, sodic plagioclase, and K-feldspar. In certain cases, mica can also be a major mineral. Some elements can become enriched in the pegmatite melt due to fractionation, and form mineral assemblages rich in Li, Be, Rb, Cs, Nb, Ta, Sn, B, P, F, and REE.

As previously stated, giant grain-size is a diagnostic textural feature for pegmatites. Although, other textural attributes are also characteristic of pegmatites, such as: (1) a systematically increase of grain size from margins to the centre of the pegmatites; (2) spatial zonation of mineral assemblages; (3) an abundance of skeletal crystal habits and/or graphic intergrowths; (4) and a highly anisotropic fabric, represented as non-equidimensional crystals aligned perpendicularly to the margins of the body, as well as layered and radial fabrics (London, 2008).

Some of these textural features, especially the spatial zonation of mineral assemblages, led to the idea that pegmatites crystallize from the margins towards the core of the body (*e.g.*, Cameron *et al.*, 1949). The internal zonation is manifested by variations in the distribution of grain size, mineral assemblage, and crystal habit. Nevertheless, unzoned pegmatites also exist, and tend to occur associated with host rocks of high metamorphic grade; they are granulometric and mineralogically homogeneous but can possess porphyritic texture and oriented fabrics. An unzoned pegmatite is not necessarily primitive in composition.

The current nomenclature of the internal zoning of pegmatites was built on Cameron's *et al.* (1949) work, who based their zone descriptions on steep deep lenticular or sheet-like pegmatite bodies related to granitic plutons. Figure 2-1 shows a simplified schematic representation of pegmatite zoning. From margin to centre, pegmatite zones are defined as follows:

- **Border zone**: Is a thin layer that surrounds the pegmatite body in contact with the host rock. It is usually composed of quartz, plagioclase, muscovite, biotite, hornblende, or elongated alkali feldspar crystals. They occur as fine- to medium-grained crystals of hypidiomorphic granular texture, similar to regular granitic rocks (London, 2008).

- **Wall zone**: If present, this zone is a thicker (~1 m), coarser-grained variant of the border zone, it can surround the pegmatite completely or partially. This zone is marked by the anisotropic orientation of inwardly elongated and flaring crystals of tourmaline, beryl, micas, and feldspars, a fabric that may be carried through the interior zones of the pegmatite (London, 2008).

- **Intermediate zones**: These include all zones between the wall and core zones. Here, minerals show a significant increase in crystal size (Jahns, 1953). The intermediate zones contain the same minerals that occur in the previous zones, as well as the separation of graphic quartz-feldspar intergrowths into individual monophase crystals (London, 2014). These zones tend to be dominated by one or two minerals, usually perthitic microcline, plagioclase, muscovite, beryl, spodumene, petalite, or montebrasite, all in association with massive quartz. The intermediate zones can be symmetrical or asymmetrical, and continuous or discontinuous throughout the pegmatite body. These zones are better developed in the thickest parts of a pegmatite and decrease their size until they disappear as the pegmatite thins out (London, 2008).

- **Core**: Is the innermost unit of a pegmatite body, it can occur as a single mass or as multiple repetitions of the same mineralogy (London, 2008). The ratio of core material to the outer zones is extremely variable. Cores of monomineralic quartz are the most common, but cores may also consist of quartz combined with various proportions of perthite, albite, lithium aluminosilicates, and phosphates (London, 2008).

  The following units may also occur in some pegmatites with no specific zone placement in the pegmatite body.

- **Fracture fillings**: These units are not abundant but are present in some pegmatites. They are mainly composed of quartz or also consist of material from other zones that has migrated outward along fractures (London, 2008).

- **Replacement bodies**: Their occurrence is proof of a process that converted a pegmatite mass into something else (London, 2014). A clear indication of replacement bodies is the presence of pseudomorph minerals or mineral assemblages.

- **Miarolitic cavities**: These cavities are crystal-lined or clay-packed, crystal-filled voids in pegmatites, that can have crystals of gem quality suspended in clay, or just an empty space. These clay-packed cavities represent the last remnants of the dense hydrous silicate melt that formed the pegmatite and that is the place where most of the gem-quality minerals are developed (London, 2014).

Other zoning patterns have also been published (*e.g.*, Jahns, 1955; Norton, 1983; Uebel, 1977). Yet, Cameron's *et al.* (1949) zoning descriptions, based on a specific type of pegmatites, are the most widely used nomenclature of internal zonation of pegmatites. In this thesis, the description of the pegmatite internal zonation is adjusted to the zoning developed in the investigated pegmatites.

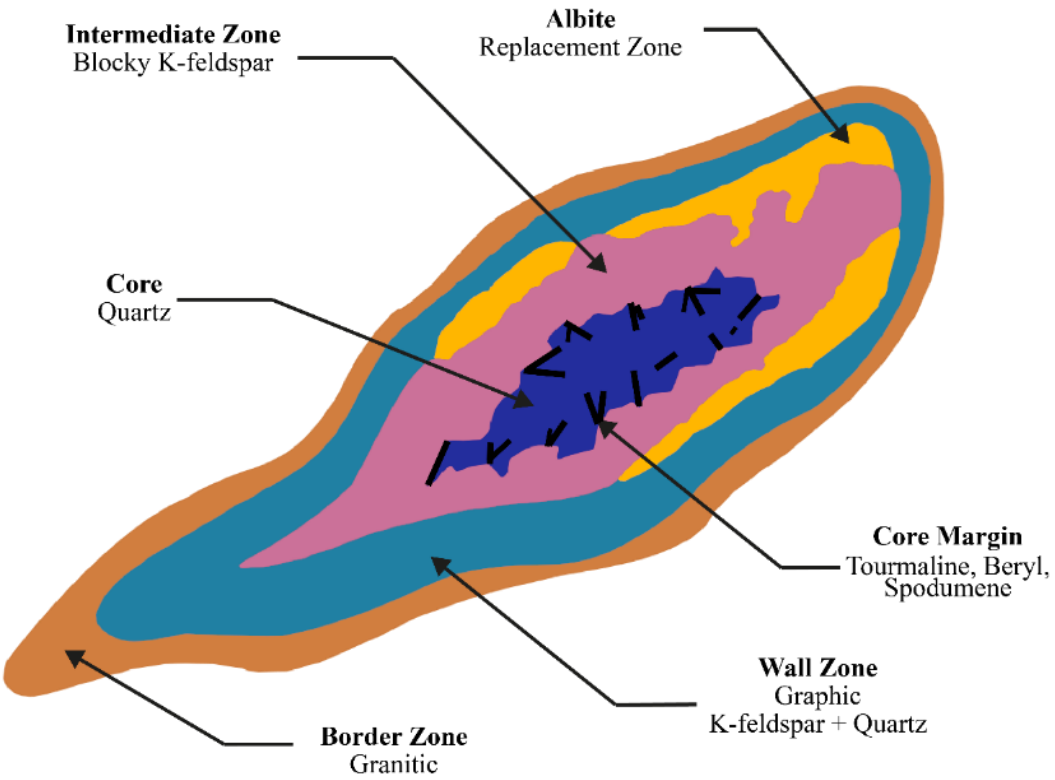

Figure 2-1 - Simplified representation of the internal zoning of a Pegmatite. Modified from Černý (1991a)

2.2. Pegmatite groups

Černý (1991a) classified pegmatite groups as the basic elements of large pegmatite populations, these pegmatites are related to individual periods of geological evolution and share structural, igneous, and geochemical links. From smaller to larger scale, pegmatites can be grouped in fields, districts, belts, and provinces.

Pegmatite fields are pegmatite groups that occur within the same geological and structural environment. These pegmatites formed during a single magmatic stage of regional evolution, share the same source type, and have equal or similar ages (Černý, 1991a). A **pegmatite district** consists of several pegmatite groups in a mining district (London, 2008). A **pegmatite belt** refers to pegmatite fields that are related to geological events of large-scale linear structure, for example a deep fault lineament or a cratonic margin (Černý, 1991a), these pegmatite fields usually belong to the same pegmatite class. A **pegmatite province** is the assemblage of pegmatite fields and belts within a large-scale geological unit, such as a metallogenic province. Essentially, they have in

common their geological evolution and mineralization style (Černý, 1991a). Yet, these pegmatite fields, districts and belts can usually belong to various classes and most likely formed at different stages of crustal evolution (Černý, 1991a).

2.3. Pegmatite formation

Many models have been proposed on how pegmatites form, but no universally accepted model of pegmatite formation has been able to satisfactorily explain all the distinct features of granitic pegmatites.

The most widely accepted model for pegmatite genesis proposes that pegmatites are formed by the fractional crystallization of large granitic plutons. Thus, pegmatites are considered as intrusive residual melts of these plutons (*e.g.*, Jahns, 1955; Jahns & Burnham, 1969). Further studies have used this model as a steppingstone to try to better understand the origin of pegmatites (*e.g.*, Fenn, 1986; London, 1989; London, 2008), adding that the pegmatite melts become enriched in incompatible components, rare elements, fluxes, and volatiles. The development of large crystals and pegmatitic textures are interpreted as the result of fluxes and volatiles presence in the pegmatite-forming melt; as these components lower the crystallization temperature, decrease nucleation rates, melt polymerization and viscosity, and increase diffusion rates and solubility (Simmons & Webber, 2008). According to this model, pegmatites from the same pegmatite field become chemically distinct with increasing distance away from the parental granite (Figure 2-2). This chemical distinction is represented by an increase in fractionation, enrichment in volatiles, increase in pegmatite zoning complexity, and the occurrence of more replacement zones (Černý, 1991a).

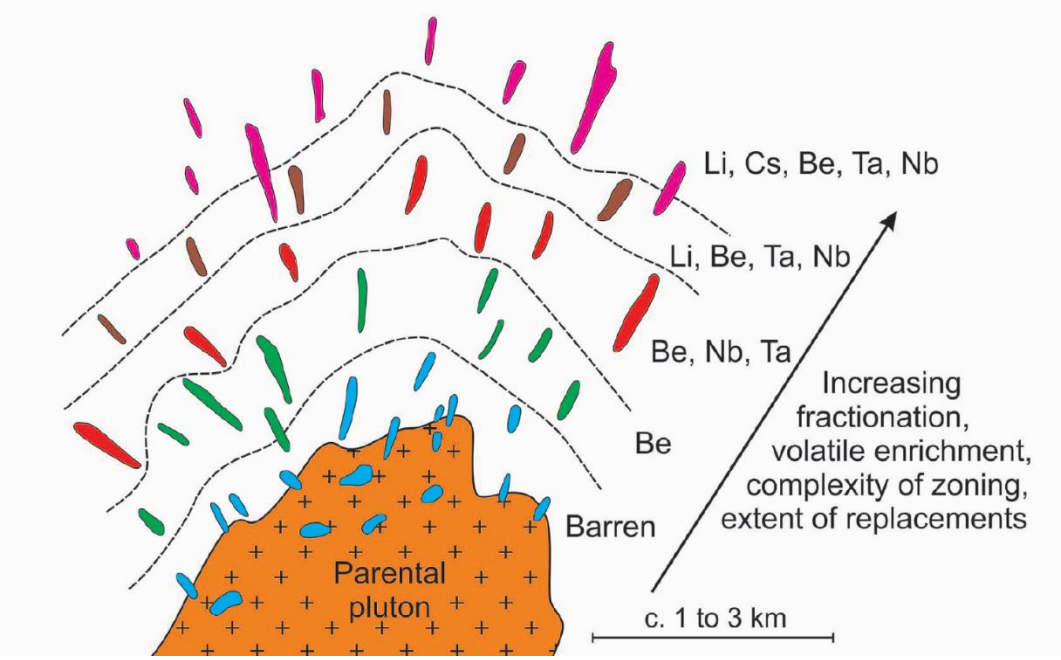

Figure 2-2 - Schematic representation of an idealized pegmatite field, showing that the pegmatites degree of evolution is related to their distance from the parental pluton. Pegmatites in and around the granite are barren and less fractionated than the farthest pegmatites which are more fractionated and richer in Li, Cs, Be, Ta and Nb. Redrawn by Müller *et al.* (2017), originally from Černý (1991b).

Researchers have also proposed that anatexis can be a mechanism capable of forming pegmatite melt (*e.g.*, Nabelek *et al.*, 1992a; 1992b; Roda Robles *et al.*, 1999). In general, this mechanism is characterized by low-degree partial melting, either around plutons or related to collisional tectonic environments (Simmons & Webber, 2008). In tectonic environments, the partial melting of sedimentary and volcanic sequences that contain incompatible elements and fluxing components, such as H_2O, B, P and F, can result in pegmatite melts (Figure 2-3). The fluxing components and incompatible elements will preferentially enter a low-degree partial melt, and subsequential fractional crystallization will create a pegmatitic melt (Simmons & Webber, 2008). The anatectic model has been recognized in some cases, for example, where no spatially related parental granite is exposed; when the exposed granitic plutons have significantly different ages; or when pegmatites occur very far from the potential parental granite (*e.g.*, Goodenough *et al.*, 2014; Müller *et al.*, 2017; Rosing-Schow *et al.*, 2021; Webber *et al.*, 2019). Anatexis has also been proposed as a pegmatite formation mechanism in localities where the pegmatite fields lack

the conventional chemical zonation (*e.g.*, Müller *et al.*, 2017; Roda Robles *et al.*, 1999; Webber *et al.*, 2019), such as the one shown in Figure 2-3.

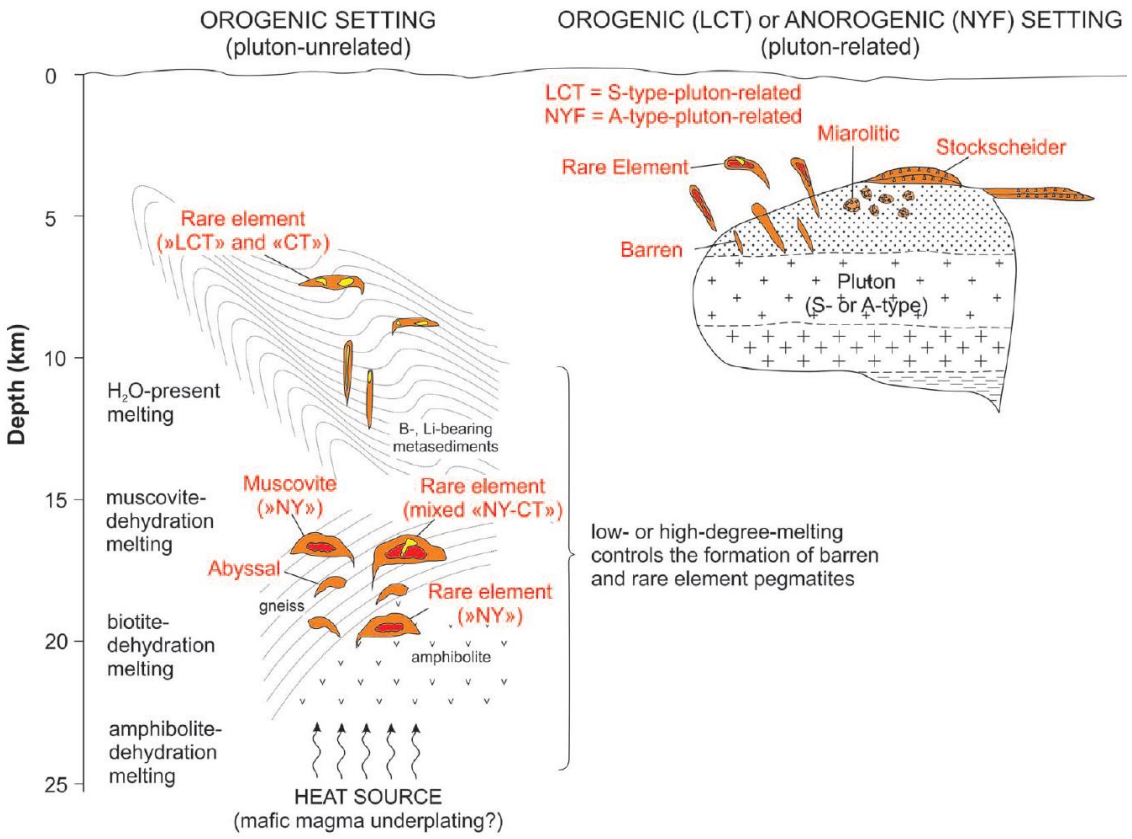

Figure 2-3 - Schematic representation of a crustal profile demonstrating two types of pegmatite formation by anatexis, pluton-unrelated or pluton-related (Müller *et al.*, 2017). Rare element and muscovite pegmatites, LCT and NYF, that originated in pluton-unrelated settings might not host Li or F, thus the classification was adapted to CT and NY, respectively. The degree of partial melting dictates the type of pegmatite that will form.

2.4. Pegmatite classification

Currently the most used pegmatite classification is the one created by Černý (1991a) and later adapted by Černý & Ercit (2005), based on the early classification works of Ginsburg *et al.* (1979). The authors use two approaches to classify pegmatites:

(1) Based on the P-T conditions of their host rock suites, the authors divided granitic-pegmatites into five classes depending on the depth of pegmatite intrusion, from deepest to shallowest: abyssal, muscovite, muscovite-rare-element, rare-element, and miarolitic; these classes were

further divided into subclasses and subtypes with fundamentally different geochemical and geological characteristics.

(2) Considering the petrogenesis and trace element signature of rare-element pegmatites derived by igneous differentiation from plutonic parents, Černý & Ercit (2005) created three families: Lithium-Cesium-Tantalum (LCT), Niobium-Yttrium-Fluorine (NYF) and mixed NYF+LCT pegmatites.

The family classification aimed to categorize large-scale pegmatite population, taking into consideration the parental granite and the derived pegmatites (Černý & Ercit, 2005). LCT pegmatites host and become progressively enriched in Li, Rb, Cs, Be, Sn, Ta, Nb (Ta > Nb) as well as B, P and F with increasing fractionation of the melt (Černý & Ercit, 2005). These pegmatites, in general, have a chemical affinity with peraluminous S-type granites (Chappell & White, 2001), derived by melting of mica-rich metapelite protoliths (Černý *et al.,* 2012). LCT pegmatites are more abundant, therefore they have been the focus of more pegmatite research (London, 2008). NYF pegmatites typically contain Nb, Ta (Nb > Ta), Ti, Y, Sc, REE, Zr, U, Th and F, and the degree of fractionation is moderate in comparison to the LCT pegmatites (Černý & Ercit, 2005). These pegmatites are depleted in P, and tourmaline is uncommon (Černý *et al.,* 2012; London, 2008). Generally, NYF pegmatites have a compositional affinity with A-type granites (Černý & Ercit, 2005; Eby, 1990), derived by anarogenic mechanisms from deep-crustal gneissic granulites and mantle basalts (Černý *et al.,* 2012). The mixed NYF+LCT family includes granites and pegmatites with mixed geochemical characteristics of the previous two families (Černý & Ercit, 2005). A small number of NYF and LCT pegmatites can also form by the fractional crystallization of I-type granites. These granites are usually linked to subduction-related magmatism and are formed from mafic to intermediate metaigneous rocks or metasedimentary rocks of volcanic origin (Černý & Ercit, 2005; Černý *et al.,* 2012).

Table 2-1 - Pegmatite classification by Černý & Ercit (2005), table adapted from Černý *et al.* (2012). HREE: Heavy rare earth elements. LREE: Light rare earth elements. BBe: Boron - Beryllium. REE: Rare earth elements. NYF: Niobium-Yttrium-Fluorine. LCT: Lithium-Cesium-Tantalum.

Class	Subclass	Type	Subtype	Family
Abyssal	HREE			NYF
	LREE			
	U			NYF
	BBe			LCT
Muscovite				
Muscovite-rare element	REE			NYF
	Li			LCT
Rare element	REE	Allanite-monazite		NYF
		Euxenite		
		Gadolinite		
	Li	Beryl	Beryl-columbite	LCT
			Beryl-columbite-phosphate	
		Complex	Spodumene	
			Petalite	
			Lepidolite	
			Elbaite	
			Amblygonite	
		Albite-spodumene		
		Albite		
Miarolitic	REE	Topaz-beryl		NYF
		Gadolinite-fergusonite		
	Li	Beryl-topaz		LCT
		Spodumene		
		Petalite		
		Lepidolite		

3. Tourmaline

3.1. Tourmaline mineralogy and chemistry

Tourmaline is a trigonal borosilicate mineral of the cyclosilicate superclass. Due to its complex chemical composition, it is classified as a supergroup in terms of nomenclature procedures. The generalized formula of tourmaline is:

$$XY_3Z_6(T_6O_{18})(BO_3)_3V_3W$$

This generalized formula represents the sites within the asymmetric unit of the structure without making assumptions about site occupancy, except for those occupied by O^2 (Hawthorne & Henry, 1999). Table 3-1 from Henry *et al.* (2011) shows the relative abundance of the generalized cations, represented by R^{1+}, R^{2+}, R^{3+} and R^{4+}, and anions, represented by $S^{1-}$and S^{2-}, in each site. Furthermore, it lists the most common cation and anion substituents for each of the valence states of the ions.

Table 3-1 - Relative site abundance of cations and anions in tourmaline-supergroup minerals. Modified from Henry *et al.* (2011). Bolded cations and anions represent the most common ions at these sites.

Site	Relative abundance of ions with different valence states	Common cations and anions at each site in order of relative abundance
X	$R^{1+} > R^{2+} >$ □ (vacancy)	R^{1+}: **Na^{+1}** >> K^{1+} R^{2+}: **Ca^{2+}**
Y	$R^{2+} > R^{3+} > R^{1+} > R^{4+}$	R^{2+}: **Fe^{2+}** ~ **Mg^{2+}** > **Mn^{2+}** >>> Zn^{2+}, Ni^{2+}, Co^{2+}, Cu^{2+} R^{3+}: **Al^{3+}** >> **Fe^{3+}** > Cr^{3+} >> V^{3+} R^{1+}: **Li^{1+}** R^{4+}: **Ti^{4+}**
Z	$R^{3+} >> R^{2+}$	R^{3+}: **Al^{3+}** >> **Fe^{3+}** > Cr^{3+} > V^{3+} R^{2+}: **Mg^{2+}** > Fe^{2+}
T	$R^{4+} >> R^{3+}$	R^{4+}: **Si^{4+}** R^{3+}: **Al^{3+}** > B^{3+}
B	R^{3+}	R^{3+}: **B^{3+}**
V	$S^{1-} >> S^{2-}$	S^{1-}: **OH^{1-}** S^{2-}: **O^{2-}**
W	S^{1-} ~ S^{2-}	S^{1-}: **OH^{1-} ~ F^{1-}** S^{2-}: **O^{2-}**

3.1.1. Crystal structure

Tourmaline-supergroup minerals are mainly rhombohedral, isostructural in the space group R3m. Although, some studies report tourmalines, or sectors within the crystals that possess an orthorhombic, monoclinic, or triclinic symmetry (*e.g.*, Akizuki *et al.*, 2001; Hughes *et al.*, 2011; Shtukenberg *et al.*, 2007; Williams *et al.*, 2010).

The structure of tourmaline-group minerals consists of six-membered rings of TO_4 tetrahedra. The acentric nature of their crystal structure derives from the apical oxygen atoms of the tetrahedral rings pointing toward the (-) c-pole. Above and below the tetrahedral rings, triangular BO_3 groups are located, sub-parallel to the (001) plane. The ninefold-coordinated X site is positioned on the threefold axis of symmetry, out of plane of the tetrahedra rings. The octahedrally coordinated Y and Z sites are both inside and outside in relation to the ring contour. The V site, O(3) in crystallographic data, is shared by one YO_6 and two ZO_6 octahedra. The W site, O(3) in crystallographic data, is linked to three YO_6 octahedra and located on the threefold axis central to the tetrahedral rings (Figure 3-1).

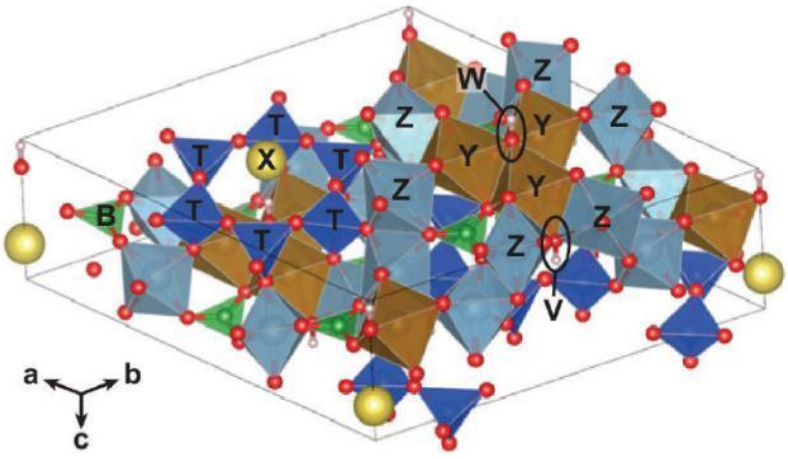

Figure 3-1 - Crystal structure of tourmaline, with rhombohedral symmetry (R3m). Yellow: X-site cations; Brown: Y-site octahedra; Light blue: Z-site octahedra; Dark blue: TO_4 tetrahedra; Green: BO_3 groups; Red: Oxygen atoms; Pink: Hydrogen. Black ellipses: V and W sites, occupied here by OH groups. Figure prepared on the VESTA software package (Momma & Izumi, 2011), using the structural data from Ertl *et al.* (2006), taken from Watenphul *et al.* (2016).

The letters in the general formula (X, Y, Z, T and B – not italicized) represent groups of cations at the [9]*X*, [6]*Y*, [6]*Z*, [4]*T*, and [3]*B* crystallographic sites (letters italicized). V and W represent groups of anions at the [3]O3 and [3]O1 sites, respectively, and the H atoms occupy the H3 and H1 sites, which are related to O3 and O1, respectively.

At least 26 relevant elements concerning concentration or occurrence have been identified in tourmaline. These constituents have diverse charges and sizes and are accommodated into the 7 crystallographic sites: *X*, *Y*, *Z*, *T*, *B*, O1, and O3; the other sites: O2, O4, O5, O6, O7, and O8, are exclusively occupied by oxygen. The number of constituent-coordination environments ([3], [4], [6], and [9] coordination) is relatively large in contrast with other minerals. Tourmaline is one of the exceptions to Pauling's parsimony rule (Pauling, 1929), which states that "The number of essentially different kinds of constituents in a crystal tends to be small". In principle, this large number of different coordination polyhedra or sites in a given mineral tends to decrease its stability, however, that's not the case with tourmaline, which occurs in a vast array of environments, from the surface of the crust to the upper mantle (*e.g.,* Lussier *et al.*, 2016; Marschall *et al.*, 2009) in the presence of H_2O, B-, and F-bearing fluids.

3.1.2. Tourmaline physical and thermochemical properties

Tourmaline is an elongated mineral, usually with a prismatic shape and well-defined crystal faces, although it can also occur as more equidimensional grains and masses (*e.g.*, Henry *et al.*, 1999; Slack, 1996). An overview of the physical properties of tourmaline are presented in Figure 3-2. Tourmaline displays a great array of colours, but the most common is black. Double terminated crystals are common and display hemimorphic character. A mineral with a hemimorphic character has different morphological forms at each end of the c crystallographic axis, this is one of the most characteristic properties of tourmaline. This anisotropy results in distinctly different properties for the opposite poles of the crystal, which gives the tourmaline its strong piezo- and pyroelectric properties (Dietrich, 1985; Lang, 2005; Lang, 1974; Sperlich *et al.*, 1996).

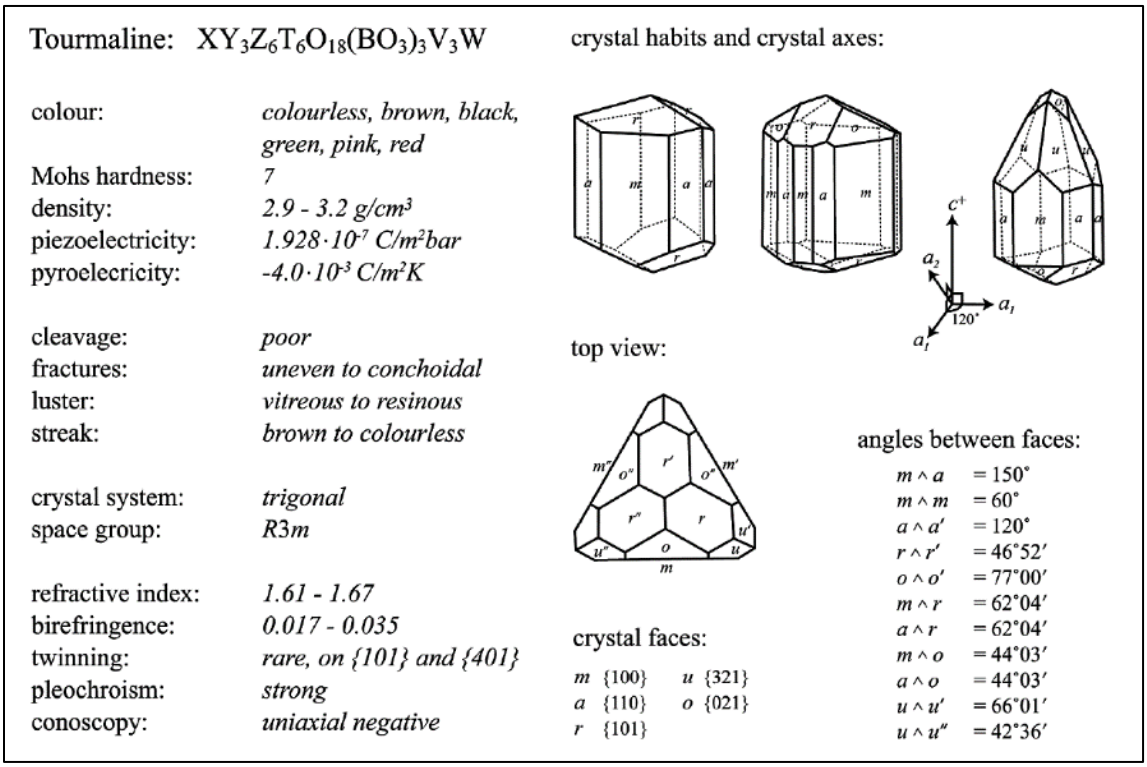

Figure 3-2 - Overview of the physical properties of tourmaline. Taken from van Hinsberg *et al.* (2011a). Data and figures from Anthony *et al.* (1995); Cady (1930); Ford & Dana (1932); Lang (2005); Tröger *et al.* (1971).

3.2. Tourmaline species and classification

A total of 38 tourmaline species are recognized by the International Mineralogy Association's Commission on New Minerals, Nomenclature and Classification (IMA-CNMNC) up until May 2021. The classification is based on the dominant compositional variability that occurs at the X, Y, Z and W sites, and to a lesser extent, V sites. The T site is usually occupied by Si, but can also be occupied by Al or B. The B site contains exclusively B. Hence, the cationic occupancies at the T and B sites are not used as primary parameters for classification, with the exception of some unusual tourmaline species (Henry *et al.*, 2011). The cationic and anionic occupancy of the X and W sites are petrologically meaningful ways to define the primary tourmaline groups and a subset of general series of tourmaline species, respectively. Based on the dominant occupancy of the X-site, tourmalines can be classified into three primary groups: alkali-, calcic- and X-vacant-tourmaline groups (Henry *et al.*, 2011). The secondary division takes into

account the dominant occupancies of the Y site, as well as considering major variations in the Z and T-site occupancy.

Further divisions correspond to the dominant W-site occupancy, three distinct anions (OH^{-1}, F^{-1}, and O^{2-}) can occupy this site, resulting in a general series of tourmaline species: hydroxy-, fluor- and oxy-species (Henry *et al.*, 2011). The primary X-site groups are defined as shown in Table 3-2, and Figure 3-3 shows these groups in a ternary system.

In this thesis, the tourmalines encountered in the investigated pegmatites and host rocks are alkali group tourmalines, namely schorls - Na (Fe^{2+}_3) $Al_6(Si_6O_{18})$ $(BO_3)_3(OH)_3(OH)$ – and dravites – Na (Mg_3) $Al_6(Si_6O_{18})$ $(BO_3)_3(OH)_3(OH)$.

Table 3-2 - Primary Tourmaline groups division according to the dominant occupancy of the X-site.

Primary Tourmaline groups	
Alkali	$(Na^{1+}+K^{1+}) \geq Ca^{2+}$ and $(Na^{1+}+K^{1+}) \geq {}^{X}\square$
Calcic	$Ca^{2+} > (Na^{1+}+K^{1+})$ and $Ca^{2+} > {}^{X}\square$
X-Vacant	${}^{X}\square > (Na^{1+}+K^{1+})$ and ${}^{X}\square > Ca^{2+}$

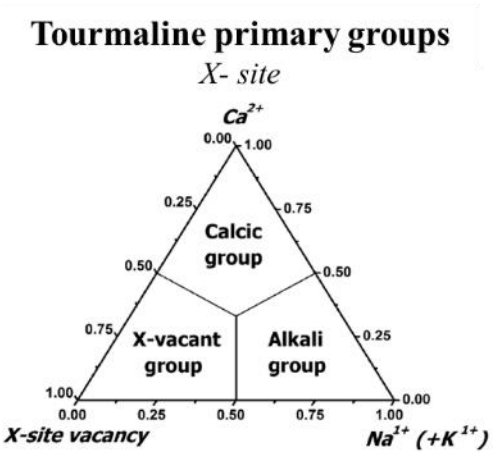

Figure 3-3 - Ternary system for the primary tourmaline groups based on the dominant occupancy of the X-site.(Henry *et al.*, 2011).

3.3. Tourmaline's Stability Range

The occurrence of tourmaline in a wide array of geological settings is caused by its extreme pressure and temperature stability range, one of the largest of crustal minerals (*e.g.*, van Hinsberg *et al.*, 2011a). Tourmaline can crystallize in hydrothermal, metamorphic, metasomatic, and magmatic settings, and occur as detrital grains in clastic sediments (*e.g.*, Henry & Dutrow, 1996; Henry *et al.*, 1999; Marschall *et al.*, 2009). Tourmaline can occur in a diversity of rock compositions, from silica-rich intrusive bodies and sediments to silica-poor mafic rocks, pelites, impure limestones and evaporates, and their metamorphic equivalents. The flexibility in the crystal

structure of the tourmaline is partially the reason that allows the mineral to acquire various compositions in response to different chemical environments and P-T conditions (Dutrow & Henry, 2011).

Tourmaline is found in many low P–T environments (*i.e.*, ~ 10 kbar, < 150 °C), it can also be found at the other extreme, at high temperature (> 850ºC) and at ultra-high pressure (UHP) conditions (> 40 kbar) (Figure 3-4). Experiments show that tourmaline undergoes melting between 725ºC and at least 950 ºC, depending on pressure and composition (*e.g.,* Henry *et al.*, 1999; London, 2011; Marschall *et al.*, 2009; Morgan & London, 1989; Ota *et al.*, 2008).

The tourmaline stability range can be affected by the composition of the coexisting fluid phase. In aqueous solutions, tourmaline is stable in acidic to neutral solution (low pH), where B is triangularly coordinated with three oxygens in a $B(OH)_3$ complex that is consistent with the B coordination of tourmaline. In neutral to basic aqueous solutions (high pH), tourmaline is unstable, in these conditions boron complexes are generally tetrahedrally coordinated to oxygen in a $B(OH)_4$ anionic complex. Tourmaline can also be unstable in solutions where the activities of the cations (including B) and anions are unfavourable (*e.g.*, Dutrow *et al.*, 1999; Dutrow & Henry, 2011; 2016; Henry & Dutrow, 1996) . The amount of boron required to stabilize tourmaline increases with increasing pH (Dutrow & Henry, 2011). Thus, tourmaline is a stable mineral at nearly all crustal P-T conditions, but its disruption within these conditions is controlled by the destabilizing compositions of the coexisting fluid phase. Since tourmaline responds to changing fluid compositions in a predictable and systematic way, transient fluid compositions can be recovered from the mineral's chemistry (*e.g.*, Dutrow & Henry, 2016; 2018; Henry & Dutrow, 2012; van Hinsberg *et al.*, 2017). Thus, tourmaline may be the only source of a chemical record of B-bearing fluids that pass through rocks (Henry & Dutrow, 2018).

Within a tourmaline the differences in chemical signature are best shown by the fine colour banding in some pegmatitic tourmalines, although common "black" tourmaline can be as finely and complexly zoned as the colourful specimens. Tourmaline's chemical and colour zonation, or its absence, are key pieces of petrogenetic information (London, 2016). Undeformed tourmaline seems to have extremely slow/negligible volume diffusion rates of major and trace elements, thus once formed tourmaline retains the evolving chemical signatures of where it crystallized (*e.g.*, Henry & Dutrow, 1996; van Hinsberg *et al.*, 2011b; van Hinsberg & Schumacher, 2011) making

them an almost ideal petrogenetic indicator of their host environment (*e.g.*, Henry & Dutrow, 1996; Keller *et al.*, 1999; London, 2011; Selway *et al.*, 2000a; Selway *et al.*, 1999; Trumbull *et al.*, 2011; van Hinsberg *et al.*, 2011a; Williamson *et al.*, 2000). Tourmalines that formed in a steady-state environment like those that crystallized within large igneous bodies, such as granites, are optically and chemically homogeneous. Hydrothermal tourmalines, that crystallized in an open system, with ever-changing temperature and composition, display the most complex zonation of all tourmalines (London, 2016). Thus, the more zoned the tourmaline is, the more variable was the host environment where it formed. Furthermore, tourmalines can be used as geothermobarometers since they are able to record the pressure and temperature of the host environment in its systematic chemical variations (Henry & Dutrow, 1996; Kawakami & Ikeda, 2003; van Hinsberg & Schumacher, 2007).

Tourmalines that are deformed at relatively high temperatures, probably through a dislocation-creep mechanism, may present diffusional compositional adjustments (Büttner, 2005; Büttner & Kasemann, 2007). Therefore, when a chemical signature is recorded in the tourmaline, it is preserved until the tourmaline is deformed or replaced by other minerals or other tourmaline generations in response to reactive fluids (*e.g.*, Dutrow & Henry, 2000; Henry *et al.*, 2004).

Tourmaline's chemical complexity hosts a large number of major and trace elements that are important tools in isotope geochemistry. B, O, H, Si, Mg, Li, Sr, Nd, Pb, K(Ar), and Cu isotope systems have been applied to tourmaline, providing a reliable record of the physicochemical conditions associated with rock-fluid interaction, fluid origin and evolution, source and genesis of ore deposits, and the geochronology of magmatic, metamorphic and hydrothermal events that formed tourmaline (Marschall & Jiang, 2011).

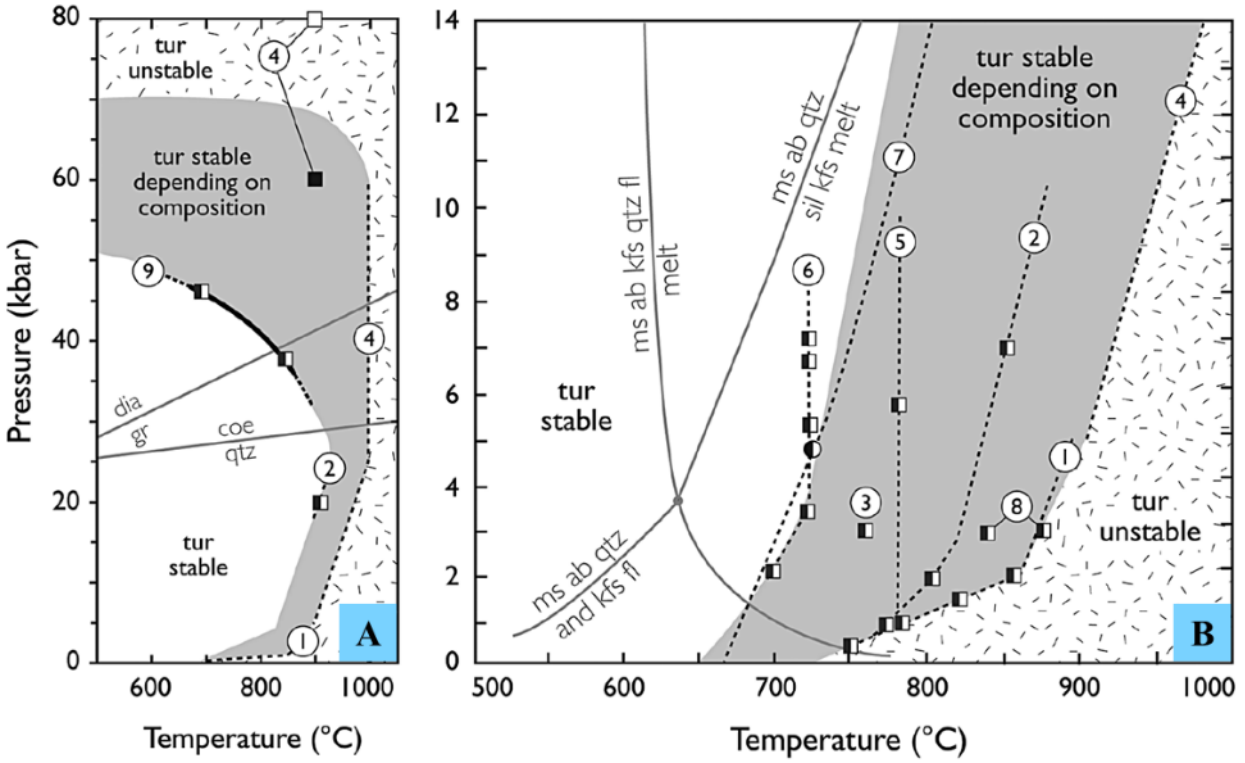

Figure 3-4 - Compilation of P-T stability estimates for tourmaline of various compositions based on constraints from natural samples. **A:** high-P stability. **B:** low-P stability. Numbered circles: constraints from natural samples. Squares: constraints from experimental data. Dashed lines: extrapolations presented by the original authors. The curve for H_2O-saturated melting reactions, the quartz-coesite and graphite-diamond phase transitions are shown for reference. Data are for: 1) dravite: (Robbins & Yoder, 1962). 2) Magnesio-foitite: (Werding & Schreyer, 1984). 3) Schorl: (Holtz & Johannes, 1991). 4) Dravite: (Krosse, 1995). 5) Na-free Mg system: (von Goerne *et al.*, 1999). 6) Na-bearing Mg system (von Goerne *et al.*, 1999). 7) natural tourmalines: (Kawakami, 2004). 8) natural tourmaline: (Spicer *et al.*, 2004). 9) dravite: (Ota *et al.*, 2008). Plots from van Hinsberg *et al.* (2011a).

4. Boron

4.1. Boron in the Continental crust

Boron (B) is a moderately volatile, lithophile metalloid. B is a trace element in most igneous rocks, it has a low atomic mass (10.811u) and two stable isotopes (^{10}B and ^{11}B).

The continental crust is the main reservoir of B on Earth. Boron is incompatible in igneous systems; thus, it partitions preferentially into fractionated silicic/granitic melts (*e.g.*, London *et al.*, 1996). These melts will form intermediate-composition to felsic igneous rocks which are the main constituents of the continental crust (Trumbull & Slack, 2018). Granites and felsic volcanic rocks show concentrations between 2 and 11 ppm (Trumbull & Slack, 2018). In highly evolved granitic magmas boron can be enriched up to weight percent (wt.%) leading to the crystallization of B-rich minerals, mostly tourmaline (*e.g.*, Morgan & London, 1989).

Another reason the continental crust is enriched in boron is its volatile behaviour. Boron is readily transported by hydrous fluids, which are widespread in and on the continents. Consequently, important concentrations of boron and boron minerals are related to many types of hydrothermal ore deposits. Ocean water is also a significant sink for B (Lemarchand *et al.*, 2000). Hydrothermal alteration of the oceanic crust and incorporation of ocean water into pelagic sediments removes B from the water and preserves it in the oceanic crust rocks. And the subduction of oceanic crust causes the release of B-bearing fluids into the overlying crust (Marschall & Jiang, 2011).

The continental crust average values for boron concentration are the following: Upper crust: 17 ± 8 ppm; lower crust: 2 ppm; and, bulk crust: c. 11 ppm (Gao *et al.*, 1998; Rudnick & Gao, 2003). By contrast the mantle is depleted of B: < 0.1 ppm (Leeman & Sisson, 1996) (Table 4-1).

Tourmaline is composed of 3 wt.% of B, making it a major host of B in the Earth's crust and a key mineral in the cycling of B (e.g. van Hinsberg *et al.*, 2011b). When tourmaline or other borosilicates are absent in felsic igneous rocks, boron is mainly hosted in micas, mostly muscovite.

Since the object of study for this dissertation are pegmatites, this chapter will focus mainly on the behaviour of B isotopes in the continental crust. The average concentration of boron in crustal rocks is given in Table 4-2.

Table 4-1 - Abundance of boron in various reservoirs. Modified from Dutrow & Henry (2011), based on the sources of B data from Henry & Dutrow (1996), Leeman & Sisson (1996) and Rudnick & Gao (2003).

Reservoirs	**Boron (ppm)**
Fluids	
Ocean water	4.4
Fresh and sedimentary water	< ~ 0.2
River water	~ 10.2 ppb
Brines	< 2160
Salt and borax lakes	< 9000
Crust	
Upper Continental	17
Middle Continental	17
Pelagic Clay	< 230
Volcanic arc basalts	2-35
Fresh mid-ocean ridge basalt	< 1.5
Within-plate basalts	< 3.0
Silicic igneous rocks	~ 5 – 1900
Pelitic and metapelitic rocks	< ~250
Lower continental crust	2
Mantle	
Primitive mantle	0.26
Upper Mantle (average)	< 0.1

Table 4-2 - Boron concentration in crustal rocks. Modified from Trumbull & Slack (2018), based on Gao *et al.* (1998).

Crustal rocks	**Boron ppm, average bulk-rock values**	
Amphibolite	9	
Carbonate	8, 22	Archean: 8, post-Archean: 22 ppm
Pelitic Rocks	38, 101	Archean: 38, post-Archean: 101 ppm
Tonalite-trondhemite-granodiorite	5	
Intermediate felsic granulites	2	
Granites (undifferentiated)	7, 3	Archean: 7, post-Archean: 3 ppm
Diorite	7	
Felsic volcanics	11	
Felsic metavolcanics	5	

4.1.1. Crustal processes of B enrichment and the Formation of Tourmaline

Igneous rocks and associated mineralization can become enriched in B and form tourmaline due to:

(1) **Partial melting of B-bearing protoliths:** tourmaline usually occurs in silicic and peraluminous volcanic rocks and plutonic rocks – rhyolites, granites, pegmatites – formed from the melting of deeply buried metasediments, which are commonly enriched in B, relative to the average crust.

(2) **Fractional crystallization of melts:** B is strongly incompatible in igneous systems; consequently, it concentrates in the melt phase. In granites having an Alumina saturation index (ASI; also known as A/CNK) between 1.2 and 1.4, the formation of tourmaline as an early liquidus phase would require ~ 2 wt.% B_2O_3 (~6200 ppm B; London, 1997; Wolf & London, 1997) or ~1 wt.% B_2O_3 (~3100 ppm B) in the most highly peraluminous melts (ASI > 1.4). It should be noted that saturation with respect to tourmaline can be reached at B concentrations as low as 0.5 wt.% B (~1550 ppm, depending on H_2O activity, fO_2 and temperature). However, this requires undersaturation with respect to H_2O (Dingwell *et al.*, 1996), which is rarely the case in fractionated granites.

(3) **Generation of hydrothermal fluids in association with B-bearing melts:** late-stage hydrothermal fluids can be B-bearing at the P-T conditions near the granitic solidus because of the partitioning of B into the hydrous fluid (Dutrow & Henry, 2011). Tourmaline can metasomatically form in the margins of igneous bodies and surrounding host rocks due to the concentration and mobility of boron in magmatic-hydrothermal fluids. These fluids are associated with many types of ore deposits (Slack & Trumbull, 2011) and can be highly oxidized, which will result in the crystallization of Fe^{3+} - rich tourmaline (*e.g.*, povondraite).

Beside granite-derived fluid metasomatism, metasomatic tourmaline can also be produced by B-bearing fluids which resulted from dehydrating metasediments in subducting slabs or orogenic belts. Tourmaline may be consumed during prograde metamorphism in water-saturated conditions because boron's solubility in aqueous fluids increases with temperature and, thus, boron is commonly removed from high-grade metamorphic environments.

4.2. Boron Stable Isotopes

^{10}B and ^{11}B are the only two stable occurring B isotopes in nature; their ratio is expressed as permil $\delta^{11}B$ values, relative to the NIST SRM-951 (National Institute of Standards and Technology, Standard Reference Material – 951; Catanzaro, 1970; Leeman & Tonarini, 2001):

$$\delta^{11}B = \left(\frac{{}^{11}B/{}^{10}B_{sample}}{{}^{11}B/{}^{10}B_{SRM951}} - 1 \right) \times 1000$$

Experimental and modelling studies have shown that, for many solid-solid or solid-fluid systems, isotopic fractionation between two phases follows the rule: the lighter isotope is preferentially incorporated in the phase where it is at higher coordination. This is combined with longer cation-anion bond lengths and weaker bond strength (e.g. Schauble, 2004). Boron occurs in trigonal coordination (III-B) or tetrahedral coordination (IV-B) with oxygen. ^{11}B is more abundant (ca. 80%) and prefers trigonal coordination, while ^{10}B (ca. 20%) prefers the tetrahedral coordination (Palmer & Swihart, 1996).

The boron isotope system has great potential for modelling geochemical cycles and as geochemical tracer of geological processes, and tracer of boron sources due to the range of $\delta^{11}B$ values. In nature, the $\delta^{11}B$ values have a range of approximately 60‰ (e.g. Marschall & Jiang, 2011). Different geological settings and reservoirs have unique B isotopic signatures (Barth, 1993; Marschall & Jiang, 2011) (Figure 4-1).

Major element chemistry commonly reflects the local hydrothermal fluid, precursor minerals or wall rocks. In contrast, isotopic data, and to a lesser degree trace element content, provide information on the source of the melt and fluids. B isotope data can discriminate among many B reservoirs: crustal, granitic, sedimentary, volcanic, seawater, basinal brine, marine evaporitic and non-marine evaporitic (Marschall & Jiang, 2011). For example: continental rocks such as granites, felsic gneisses and schists have light isotopic compositions. In contrast, metabasite, mid-ocean ridge basalt (MORB), altered oceanic crust and marine sediments display higher $\delta^{11}B$ values (Marschall & Jiang, 2011) (Figure 4-1).

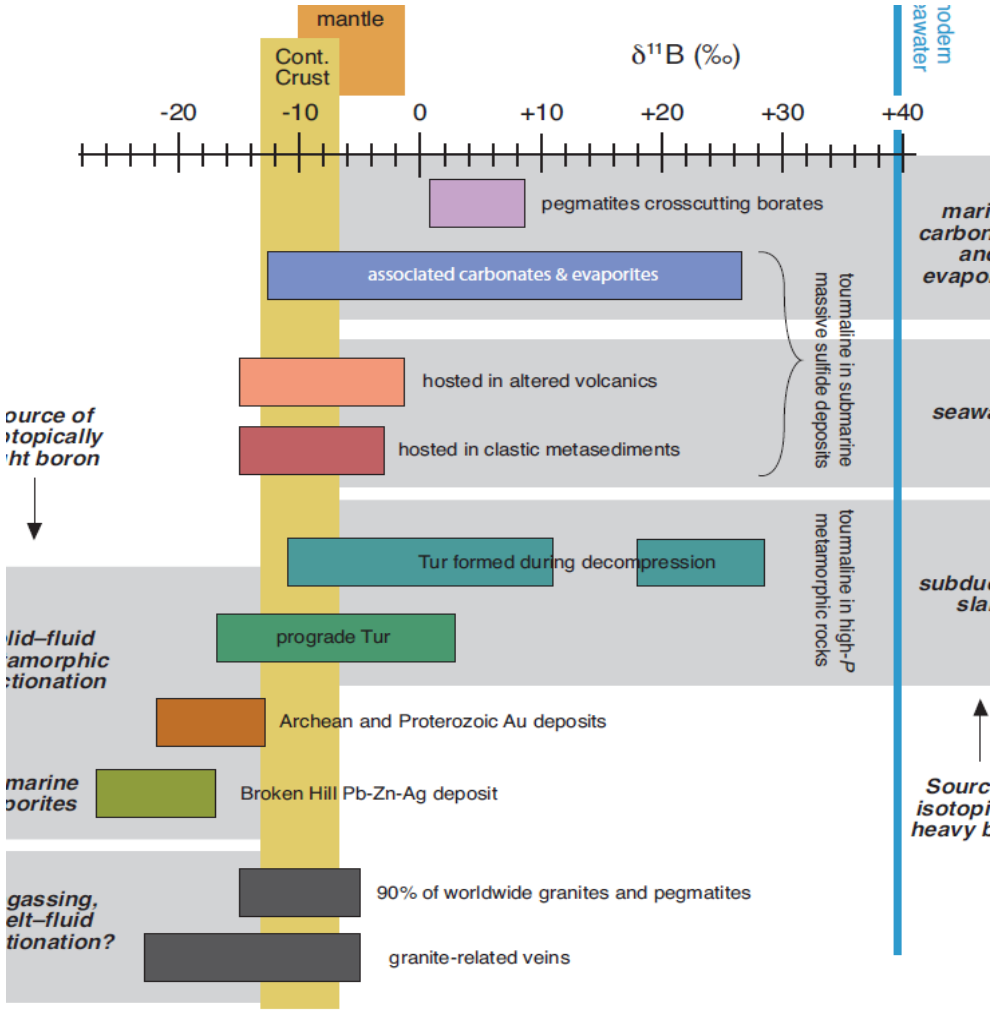

Figure 4-1 - B isotopic composition as a function of host rock type (represented by coloured boxes) and inferred B sources (represented by grey boxes). Tur= tourmaline. Taken from Marschall & Jiang (2011).

The most important carriers of B among common metamorphic rocks within the continental crust are amphibolite, metacarbonate, metagreywacke, and metapelite, especially the latter (*e.g.*, Leeman & Sisson, 1996; Rudnick & Gao, 2003). The isotopic composition of B in metamorphic and igneous rocks of the continental crust ranges between -20 to +10‰ for the protoliths. Although, fractionation during phase transition at low temperatures (< 500ºC) also influences these values.

Overall, during metamorphic devolatilization reactions, boron is susceptible to loss. Yet, if minerals like tourmaline crystallize in adequate amount, prograde metamorphism and anatexis have little effect on B isotopes (*e.g.*, Kasemann *et al.*, 2000). Since B isotopic fractionation is

marginally affected by melting or partial melting, B isotope data of rocks, magmatic minerals, glass, or melt inclusions are then used to constrain the rock or mineral's melt source.

5. The Sveconorwegian orogeny with emphasis on the Bamble Sector

5.1. The Sveconorwegian Orogeny

The Sveconorwegian orogenic belt is situated at the southwest margin of Fennoscandia and to the southeast front of the Caledonian belt (Gorbatschev & Bogdanova, 1993). It extends over 500 km and covers southwestern Sweden and south Norway (Bingen *et al.*, 2008a) (Figure 5-1). The belt is reconstructed to the east of the Grenville orogenic belt of Laurentia, facing Amazonia, at the end of the Mesoproterozoic and during the Neoproterozoic (Bogdanova *et al.*, 2008; Cawood & Pisarevsky, 2006; Hoffman, 1991; Karlstrom *et al.*, 2001; Torsvik *et al.*, 1996). Bingen *et al.* (2008c) proposes a four-phase geological model for the Sveconorwegian orogeny based on recorded tectono-metamorphic events (subductions and collisions) where the Sveconorwegian belt is a result of the collision between a common Laurentia-Baltica margin and the Amazonia indenter. In contrast, Slagstad *et al.* (2017 & 2020) proposes that the Sveconorwegian belt evolved by diachronous accretion of previously fragmented crustal blocks along an active continental margin, based on new interpretations of magmatic and metamorphic evidence from the western part of the Sveconorwegian Province (Blereau *et al.*, 2016; Bybee *et al.*, 2014; Coint *et al.*, 2015; Slagstad *et al.*, 2012). The authors also concluded that although the Sveconorwegian and the Grenville orogeny are geodynamically linked they represent tectonically distinct events along an extensive convergent margin.

The Baltica-Laurentia margin is typically interpreted to have been active prior to the Sveconorwegian-Grenvillian orogenesis (Culshaw *et al.*, 2013; McNutt & Dickin, 2012; Rivers & Corrigan, 2000; Roberts & Slagstad, 2015). The Sveconorwegian orogen is comprised of the reworked rocks that formed the pre-orogenic margin of Baltica, with ages of at least 1.9 to 1.5 Ga (Andersen, 1997; Andersen *et al.*, 2001; Andersen *et al.*, 2004; de Haas *et al.*, 1993; Knudsen *et al.*, 1997; Möller *et al.*, 2015; Roberts *et al.*, 2013). The pre-Sveconorwegian (> 1140Ma) SW Baltica margin has been poorly reconstructed since later geological processes have rewritten it (Slagstad *et al.*, 2017). However, the widespread emplacement of mafic dikes, bimodal volcanism, and sedimentation (between c. 1.2 and 1.1 Ga) are evidences of an active margin with widespread, long-lived continental extension that took place in a continental back-arc setting (*e.g.*, Brewer *et*

al., 2002; Roberts & Slagstad, 2015; Roberts *et al.*, 2011; Söderlund *et al.*, 2006). Slagstad *et al.* (2017) considers these evidences and proposes that this part of Baltica was comprised by variably thinned continental ribbons and intervening basins.

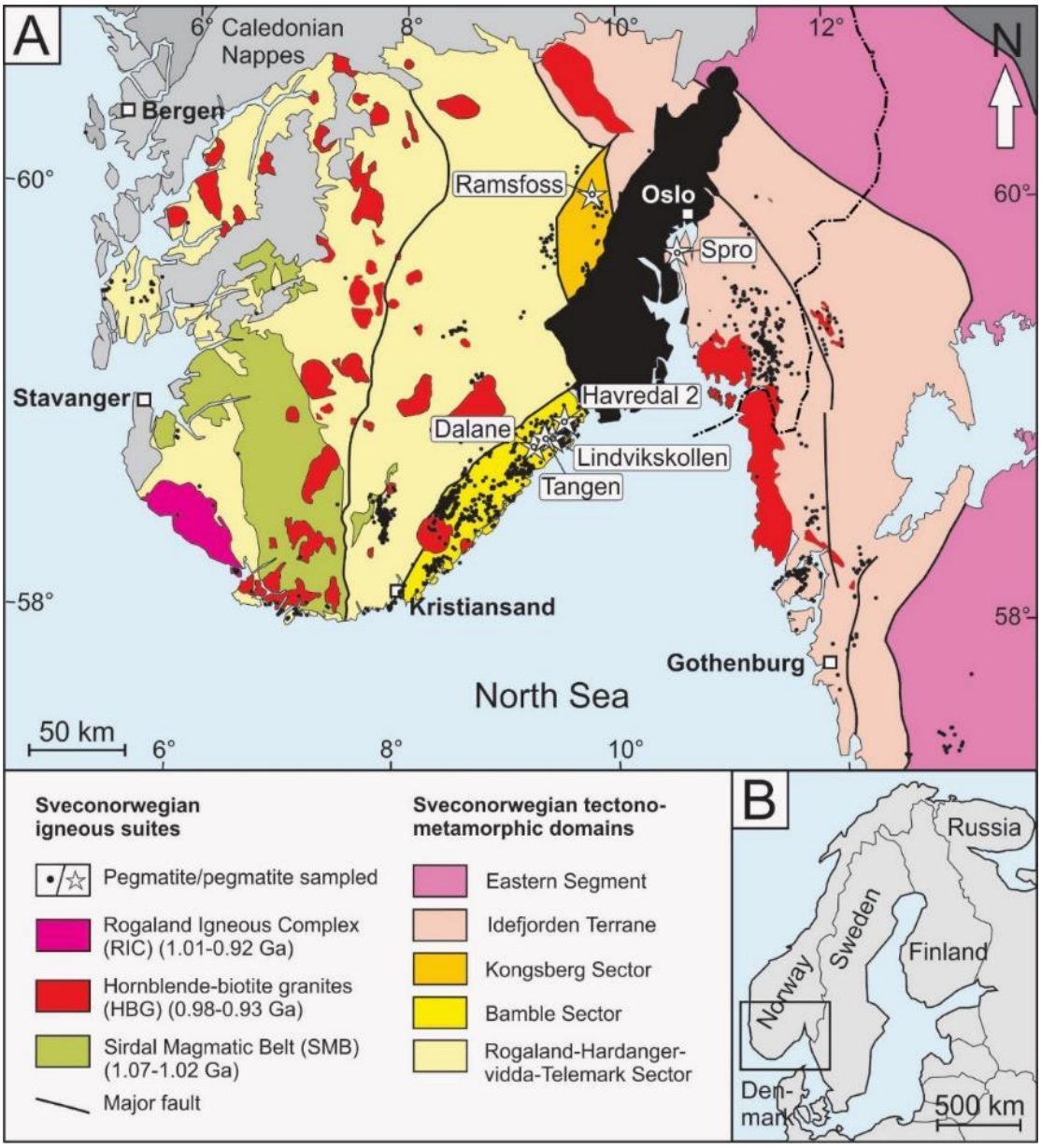

Figure 5-1 - Simplified map of the Sveconorwegian orogen. **A:** Simplified map of southern Norway and southwestern Sweden showing the domains and segments of the Sveconorwegian orogen (coloured areas), major faults and thrust zones, and orogenic magmatism. From Müller *et al.* (2017) according to Bingen *et al.* (2008c). **B:** Inset showing the location of map A at the southern tip of Scandinavia.

The Sveconorwegian orogeny comprised a series of geographically and tectonically discreet events between 1140 and 920 Ma. The Sveconorwegian orogen has been divided into 5 tectonic units, separated by crustal scale shear zones (Figure 5-1). Many authors have differing ideas about the divisions and nomenclature of the units. Bingen *et al.* (2008c) defines these units as terranes, Slagstad *et al.* (2017) considers them as sectors and terranes, and Andersen (2005) proposes the use of a non-genetic regional nomenclature, such as blocks. A summary of their respective divisions is presented on Table 5-1.

Table 5-1 - Comparison between different regional nomenclature systems, namely Andersen (2005); Bingen *et al.* (2008c) and Slagstad *et al.* (2017).

Andersen, 2005	**Bingen et al., 2008**	**Slagstad et al., 2017**
Vänern-Halmstad Block	Eastern Segment	Eastern Segment
Trysil-Vättern Block		
Randsfjord-Lygnern Block	Idefjord Terrane	Idefjorden Terrane
Kongsberg-Marstrand Block		
	Kongsberg Terrane	Kongsberg Sector
Bamble- Lillesand Block	Bamble Terrane	Bamble Sector
Tromøy Block		
Hardangervidda-Rogaland Block	Telemarkia Terrane	The Rogaland - Hardanger - Telemark Sector
Telemark Block		

The five tectonic units were affected by several major tectonometamorphic events during the Sveconorwegian orogeny. Bingen *et al.* (2008c) suggested a four-phase model for the Sveconorwegian orogeny. The four phases are as follow: Arendal phase (1140 – 1080 Ma), Agder phase (1050 – 980 Ma), Falkenberg phase (980 – 970 Ma) and Dalane phase (970 – 900 Ma) (Table 5-2). In this thesis, the most recent nomenclature of Slagstad *et al.* (2017) is applied, with the exception of the name for the Idefjorden 'Terrane'. A tectonostratigraphic terrane is a fault-bounded crustal block with a geological history that is different from the neighbouring units (Condie, 1997). Some authors contest the terrane status of the Idefjorden unit (*e.g.*, Andersen *et al.*, 2004). Therefore, apostrophes will be used in this thesis to reference this unit, following the example of Slagstad *et al.* (2012). The five tectonic units of the Sveconorwegian orogeny are:

- The **Easter Segment** is mainly comprised of gneissic granitoids, compositionally similar to the rocks of the Transcandinavian Igneous Belt (TIB), with ages ranging between 1800 and 1640 Ma (Högdahl *et al.*, 2004; Möller *et al.*, 2007; Söderlund *et al.*, 1999; Söderlund *et al.*, 2002).

- The **Idefjorden 'Terrane'** is composed of mainly calc-alkaline and tholeiitic plutonic and volcanic rocks, associated with greywacke-bearing metasedimentary sequences, with ages between 1660 to 1520 Ma (Åhäll & Connelly, 2008; Åhäll & Larson, 2000; Andersen *et al.*, 2004; Bingen *et al.*, 2001; Brewer *et al.*, 1998).

- The **Kongsberg Sector** in general consists of a heterogeneous suite of amphibolite- to granulite-facies gneisses and amphibolites with gabbroic and granitic intrusions (Jacobsen, 1975; Morton *et al.*, 1970; Starmer, 1972). This sector has been divided into 3 main complexes. In the Kongsberg Complex, granodioritic to tonalitic gneisses, associated with metasupracrustal, rocks have ages between c. 1530 and 1500 Ma (Andersen *et al.*, 2004; 2008b; Bingen *et al.*, 2005). Gabbros of the Modum Complex intruded at c. 1200 Ma (Munz *et al.*, 1994), and meta-igneous bodies of the Veme Complex have ages between c. 1555 Ma and 1495 Ma (Bingen *et al.*, 2008b; Bingen *et al.*, 2005).

- The **Bamble Sector** underwent amphibolite- to granulite-facies metamorphism (Nijland & Maijer, 1993; Touret, 1971). The dominant lithologies of this sector include migmatitic granitic orthogneisses, with protolith ages between 1600 to 1520 Ma (Andersen *et al.*, 2004), which intruded the quartz-rich and metapelitic metasedimentary rocks (*e.g.,* de Haas *et al.*, 1999; Starmer, 1985). The rocks of this sector were intruded by several pulses of felsic and basic magmas, between 1235 and 1135 Ma (Heaman & Smalley, 1994). The Bamble sector hosts the rocks studied in this thesis and as such it will be further explained below.

- The **Rogaland-Hardangervidda Sector** is divided into four sub-sectors according to their metamorphic grade, from low-grade to granulite-facies (Bingen *et al.*, 2005) and is characterized as the location of voluminous plutonism from 1520 up to 850 Ma. During the Agder phase, the Sirdal Magmatic Belt (SMB) was formed, this is a large (200 x 50 km), mostly undeformed and unmetamorphosed granitoid batholith, that was emplaced between c. 1060 and 1020 Ma in the Rogaland-Vest Agder area (Coint *et al.*, 2015; Slagstad *et al.*, 2012).

The earliest Sveconorwegian tectonic event corresponds to the Arendal phase (Bingen *et al.*, 2008c), and is interpreted as the result of accretionary events related to long-lived convergence, accretion, and amalgamation along the SW Baltica margin (Söderlund *et al.*, 2008) between the Rogaland- Hardangervidda Sector and Idefjorden 'Terrane'. This process resulted in the formation of the Bamble and Kongsberg Sectors, interpreted as tectonic wedges (Andersson *et al.*, 1996; Ebbing *et al.*, 2005). This event produced crustal thickening with metamorphism peaking at intermediate-pressure granulite-facies conditions. At 1110 Ma, the convergence continued, and it resulted in the propagation of high-grade metamorphism in the Bamble and Kongsberg Sectors and locally into the Idefjorden 'Terrane', as well as the thrusting of the Bamble Sector onto the Rogaland-Hardangervidda Sector ramp, materialized by the Kristiansand-Porsgrunn Shear Zone (Bingen *et al.*, 2008c). At 1080 Ma, thrusting ended with regional cooling. After the unroofing of the Bamble and Kongsberg Sectors, there was a period of apparent tectonic quiescence in the Sveconorwegian belt between 1080 and 1050 Ma (Bingen *et al.*, 2008c).

Geochemical and isotope data of the igneous rocks of southern Norway demonstrate that the Rogaland-Hardangervidda, Bamble and Kongsberg Sectors have an identical geochemical signature, which implies that these sectors were part of the same Fennoscandian continental margin before 1.6 Ga (Andersen *et al.*, 2001; Andersen *et al.*, 2009; Andersen *et al.*, 2004; Andersen *et al.*, 2002).

Between 1050 and 980 Ma the Agder phase took place (Bingen *et al.*, 2008c), this period is characterized by an oblique continent-continent collision between Fennoscandia and a large continent, possibly Amazonia, according to Bingen *et al.* (2008c). It resulted in tectonic imbrication and crustal thickening in the central part of the orogen. According to Slagstad *et al.* (2017), this metamorphic event represents foreland-directed thrusting of high-pressure metamorphism close to the orogenic foreland (Möller *et al.*, 2015) – Idefjorden 'Terrane' – and an extended medium-pressure metamorphism towards the hinterland – Rogaland-Hardangervidda Sector (Bingen *et al.*, 2008c). As late as 1010 Ma the Rogaland- Hardangervidda Sector was thrusted over the Idefjorden 'Terrane' (Bingen *et al.*, 2008b), although the timing of the convergence of other units is still unknown.

The Eastern Segment records eclogite-facies metamorphism at c. 980 Ma (Möller, 1998; Möller *et al.*, 2015) and the Mylonite Zone and Göta-Älv Shear Zone shows amphibolite-facies

metamorphism, migmatization and related deformation at 980 – 970 Ma (Ahlin *et al.*, 2006; Andersson *et al.*, 2002) possibly linked to thrusting of the Idefjorden 'Terrane' onto the Eastern Segment (Park *et al.*, 1991; Stephens *et al.*, 1996) or strike-slip displacement (Andersen, 2005; Bingen *et al.*, 2001; de Haas *et al.*, 1999) . These events correspond to Bingen *et al.* (2008c) Falkenberg phase, which represents the final propagation of the foreland, and is evidence for the last convergence event of the orogeny.

Shortly after, large-scale extension occurred. Evidences of this were documented along the Mylonite Zone (Viola *et al.*, 2011) as well as prograde mineral zoning in the Eastern Segment eclogites which indicates relative rapid burial and exhumation (Möller, 1998).

The Dalane Phase, 970 – 900 Ma, is characterized by the gravitational collapse of the orogen, associated with post-collisional magmatism and low pressure, high temperature metamorphism (Bingen *et al.*, 2008c). The southern part of the Eastern Segment and the Rogaland-Vest Agder unit in the Rogaland-Hardangervidda sector were exhumed to upper crustal level during this phase, resulting in large-scale gneiss dome or core complex-like structures (Bingen *et al.*, 2008c).

In various parts of the Sveconorwegian orogen and its foreland, intrusive magmatism started as A-type magmatism at c. 1168 Ma (Andersen *et al.*, 2007), and it seems it continued throughout the Sveconorwegian orogen until c. 915 Ma (Söderlund *et al.*, 2005; Vander Auwera *et al.*, 2011). The magmatism included voluminous ferroan granites, minor gabbros, mafic dykes and anorthosite (*e.g.*, Høy, 2016; Jensen & Corfu, 2016; Slagstad *et al.*, 2012; Vander Auwera *et al.*, 2011). The ferroan compositions of these rocks have been interpreted to be related to extensional events (Vander Auwera *et al.*, 2011), and match with the long-lived extensional reactivation of the Mylonite Zone at least until 920 Ma (Viola *et al.*, 2011). The extension is usually attributed to orogenic collapse and delamination of thickened lithosphere, however Slagstad *et al.* (2017) favours the idea that the prolonged extension took place in a continental back-arc setting, based on previous studies by Coint *et al.* (2015) and Slagstad *et al.* (2012).

No metamorphism is recorded in the Bamble and Kongsberg Sectors after 1080 Ma, and in the Idefjorden 'Terrane' after 1025 Ma (Bingen *et al.*, 2008b). However, high-grade regional metamorphism is documented in the western part of the Rogaland-Hardangervidda Sector,

between 1035 and 970 Ma including ultra-high temperature metamorphism at 1000 Ma (Drüppel *et al.*, 2012).

Table 5-2 - Summary of the Sveconorwegian orogeny phases (Bingen *et al.*, 2008c).

Ages (Ma)	Phases	Sectors Involved	Metamorphism	Related Magmatism	
1140	Arendal	Rogaland-Hardangervidda Sector and Idefjorden 'Terrane'	Granulite-facies	Intrusive Magmatism	Post-Collisional
		Kongsberg and Bamble Sectors	High grade metamorphism: amphibolite- to granulite-facies		
1080					
1050	Agder	Idefjorden 'Terrane'	HP metamorphism		
		Rogaland-Hardangervidda Sector	MP metamorphism, High-grade regional metamorphism and UHT metamorphism		
980	Falkenberg	Eastern Segment	Eclogite facies		
970	Dalane	Eastern Segment and Rogaland-Hardangervidda Sector	LP – HT metamorphism		
900					

The Sveconorwegian orogen lacks any ultramafic rocks that could represent ophiolite suites related to the closure of an oceanic basin during the orogeny, as well as Sveconorwegian subduction related igneous rocks east of the Oslo rift. So it is unknown if the orogenic belt hosts a suture zone between the three main units, although if it exists it would probably be located between the Rogaland-Hardangervidda Sector and Idefjorden 'Terrane', implying that the

Rogaland-Hardangervidda Sector has an exotic origin and was accreted by closure of an ocean basin, during the orogeny (Bingen *et al.*, 2008c).

5.2. The Bamble Sector

The Kragerø pegmatites studied in this thesis occur in the Bamble Sector, an approximately 30 km wide, 135 km long Precambrian NE-SW tectonic unit. The Permian Oslo Rift cuts off the Bamble Sector to the northeast. To the west, the Bamble Sector is thrusted over the Rogaland-Hardangervidda Sector (Telemark Block; Andersen, 2005). This contact is marked by the Porsgrunn-Kristiansand shear zone, and it shows a thrust phase, associated with amphibolite-facies conditions (1.07 Ga) that was followed by an extension phase, associated with green-schist conditions (890 Ma; Mulch, 2004).

The Bamble Sector is a high-grade gneissic sector with multiple isoclinal folding (Bugge, 1943; Starmer, 1985; 1996). Traditionally the Bamble sector has been correlated with the Kongsberg Sector (Bingen *et al.*, 2005; Bugge, 1936; Bugge, 1943; Starmer, 1985; 1996) although this notion has been challenged by geochemical evidence (*e.g.*, Andersen, 2005).

The sector predominantly consists of: (1) Gothian migmatitic granitic para- and orthogneisses, with protolith ages between 1600 and 1520 Ma, the formation environment of these rocks has been interpreted as a magmatic arc setting (*e.g.*, Andersen *et al.*, 2004; Pedersen *et al.*, 2009); (2) quartz-rich metasedimentary rocks, deposited in shallow-water and turbiditic environments; and (3) intrusive magmatic rocks: abundant felsic and mafic magmatism, from around 1235 to 1135 Ma (*e.g.*, Heaman & Smalley, 1994), and post-collisional granite plutons, c. 990 to 925 Ma (Andersen, 1997; Kullerud & Machado, 1991).

During the early stage of the Sveconorwegian orogeny (1.25 – 0.9 Ga), granitic-charnockitic magmas intruded the central part of the sector, as well as along and across the contact between the Bamble Sector and the Rogaland-Hardangervidda Sector, between 1.12 and 1.19 Ga (Andersen *et al.*, 1994; Heaman & Smalley, 1994; Kullerud & Machado, 1991). Some authors propose that the Bamble and the Rogaland-Hardangervidda Sectors have a common history dating back to the early Mesoproterozoic. This is evidenced by the intrusive ages of granitic-charnockitic augen gneisses (1190-1120 Ga; Andersen *et al.*, 1994; Field *et al.*, 1985; Heaman & Smalley,

1994) and their syn-kinematic and syn-metamorphic relationship with the Porsgrunn-Kristiansand shear zone (Starmer, 1987), as well as age correlations between rocks of both sectors (Roberts *et al.*, 2013).

Regarding its geotectonic evolution, the rocks of the Bamble sector were reworked during the Sveconorwegian orogeny and resulted in two amphibolite- to granulite-facies metamorphic peaks: at 1140 to 1125 Ma and at 1110 to 1080 Ma (Bingen *et al.*, 2008c). The granulite-facies rocks occurred on Tromøy, Hisøy and other islands along the coast up to several kilometres inland. The rest of the complex consists of upper amphibolite-facies rocks, with the exception of several "granulite-facies islands".

The cause of a granulite-facies metamorphism is still debatable (Nijland *et al.*, 2014). It is widely accepted based on geochronological data that a Sveconorwegian granulite-facies event was superimposed on an already high grade migmatitic gneiss terrane (geochronological data gathered by Nijland *et al.* (2014) from: Bingen *et al.* (2008b); Cosca *et al.* (1998); De Haas *et al.* (2002); Graham *et al.* (2005); Knudsen & Andersen (1999); Kullerud & Machado (1991)). The presence of carbonic and saline fluids controlled the development of H_2O-poor, high-grade mineral assemblages in the granulite-facies zone as well in the granulite-facies islands in the amphibolite-facies zone (*e.g.*, Touret & Nijland, 2012). A possible origin for the granulite-facies metamorphism involves a heat source associated with thermal doming due to the elevation of the asthenosphere magmas under an overriding plate, or thinned lithosphere as a result of an attempted rifting (Nijland, 1993).

During the late Arendal stage, the lithologies of the Bamble Sector were affected by widespread metasomatism. The metasomatism was part of the Sveconorwegian regional amphibolite-facies metamorphism phase that affected the Bamble Sector. Engvik *et al.* (2011) constrained this phase with U-Pb rutile and Rb-Sr phlogopite ages between 1090 and 1040 Ma, which formed during scapolitization and albitization. The scapolitization temperature conditions were 600 to 700ºC (Engvik *et al.*, 2011), whereas the albitization temperature conditions are considered to be broader, up to 700ºC (Engvik *et al.*, 2011; Nijland & Touret, 2001).

Scapolitization is locally widespread, especially affecting metagabbroic bodies (Nijland *et al.*, 2014). Cl-scapolite rocks are associated with Cl-apatite + enstatite + phlogopite veins (Engvik *et al.*, 2009; Lieftink *et al.*, 1994), most probably of metasomatic origin, derived from an ilmenite-

bearing precursor (Austrheim *et al.*, 2008). The veins subsequently underwent hydrous alteration, which resulted in the replacement of Cl-apatite by F-OH-apatite and the formation of monazite and xenotime (Engvik *et al.*, 2009; Harlov *et al.*, 2002; Lieftink *et al.*, 1994). The hydrous alteration is quite widespread, and it also occurred in (non-metasomatized) granite pegmatites *e.g.*, Gloserheia (Åmli, 1975; 1977; Harlov, 2011). These metasomatic rocks have been studied in other localities close to Kragerø, namely at Ødegården Verk, Ringsjø, Åtangen, Valberg, and Langøy (Engvik *et al.*, 2014; Engvik *et al.*, 2011; Lieftink *et al.*, 1994).

Both metagabbros and the sediments were altered by albitization, which occurs in the central part of the Bamble Sector and in the Kragerø area (Bugge, 1965; Elliott, 1966; Engvik *et al.*, 2008; Nijland & Touret, 2001). In the Kragerø area, albitization is generally associated with scapolite-bearing rocks, and postdates the scapolitization (Engvik *et al.*, 2018). In the Kongsberg Sector similar lithologies also occur (Jøsang, 1966; Munz *et al.*, 1994; Munz *et al.*, 1995).

The distribution of albitites in the Bamble sector suggests the presence of a regional scale 'irrigation network' associated to late fracture system and along gabbro-country rock contacts, where these rocks occur along a complex system of elongated zones and patches, that originated during the last stage of the Sveconorwegian orogen (Nijland & Touret, 2001). Engvik *et al.* (2014), based on the mineralogical and geochemical evidence, suggests that the albitite-forming fluids were likely rich in Na, K, Cl, Mg, B and P. The age of this network is unclear, Munz *et al.* (1994) dated similar albitized rocks of the Kongsberg Sector and obtained a U-Pb titanite age of 1080 ± 3 Ma.

Albitites are usually enriched in Ti-minerals: titanite and rutile. Kragerøite is the local name used for albitite rocks enriched in rutile. They can be apatite rich, often associated with apatite-actinolite rocks. Where the alteration has been more pervasive, mafic phases are non-existent, here the albitite is made up of nearly monomineralic albite (Ab_{98-99}), with some minor rutile (Engvik *et al.*, 2008; Engvik *et al.*, 2011). Locally, the albitite can be Ti-rich therefore this rock has been mined as Ti ore, for example, at Lindvikskollen.

The end of the Arendal phase (1140 - 1080 Ma) is marked by the Bamble sector-wide emplacement of granitic rare-element pegmatites which formed several pegmatite clusters, including the Kragerø field (Müller *et al.*, 2015; Müller *et al.*, 2017; Rosing-Schow *et al.*, 2021)

Following the peak Sveconorwegian metamorphism, the coastal zone and the adjacent part of the amphibolite-facies area experienced isobaric cooling, which is recorded by mineral assemblages (Nijland *et al.*, 1993; Visser & Senior, 1990) and fluid inclusions isochores (Touret & Olsen, 1985). The Nelaug area, next to the Porsgrunn-Kristiansand shear zone, however, underwent an increase in P-T after the initial cooling (Nijland, 1993).

The intrusion of the post-tectonic Herefoss (926 ± 8 Ma; Andersen, 1997) and Grimstad (989 ± 9 Ma; Kullerud & Machado, 1991) granites in the Bamble Sector marks the end of the Sveconorwegian orogeny.

6. The Sveconorwegian pegmatites with emphasis on the Kragerø pegmatite field

The South Norwegian Pegmatite Province hosts more than 5000 large pegmatite bodies, which makes it one of the largest pegmatite clusters in the world. This province covers most of the Sveconorwegian orogen in southern Norway and some parts of southwestern Sweden (Müller *et al.*, 2015)(Figure 6-1). It is comprised of seven pegmatite districts: Mandal, Setesdal, Bamble, Nissedal, Hardanger, Buskerud and Østfold-Halland. The districts are not confined to any tectonic domain, yet their pegmatite fields usually occur restricted to certain sectors and segments. Overall, the Sveconorwegian pegmatites are classified as abyssal and rare-metal pegmatites with NYF-affinity (Müller *et al.*, 2017).

This thesis focuses mainly on the Lindvikskollen pegmatite from the Kragerø pegmatite field of the Bamble pegmatite district. However, in order to compare results, other Sveconorwegian pegmatites were studied as well. The pegmatites investigated include (1) three additional pegmatites from the Kragerø pegmatite field: Tangen, Dalane and Havredal pegmatites; (2) one from the Kongsberg Sector: Ramfoss pegmatite; and finally, (3) one from the Idefjorden 'Terrane': the Spro pegmatite. Table 6-1 presents a list of these pegmatites, to which pegmatite district/field they belong and their host rocks.

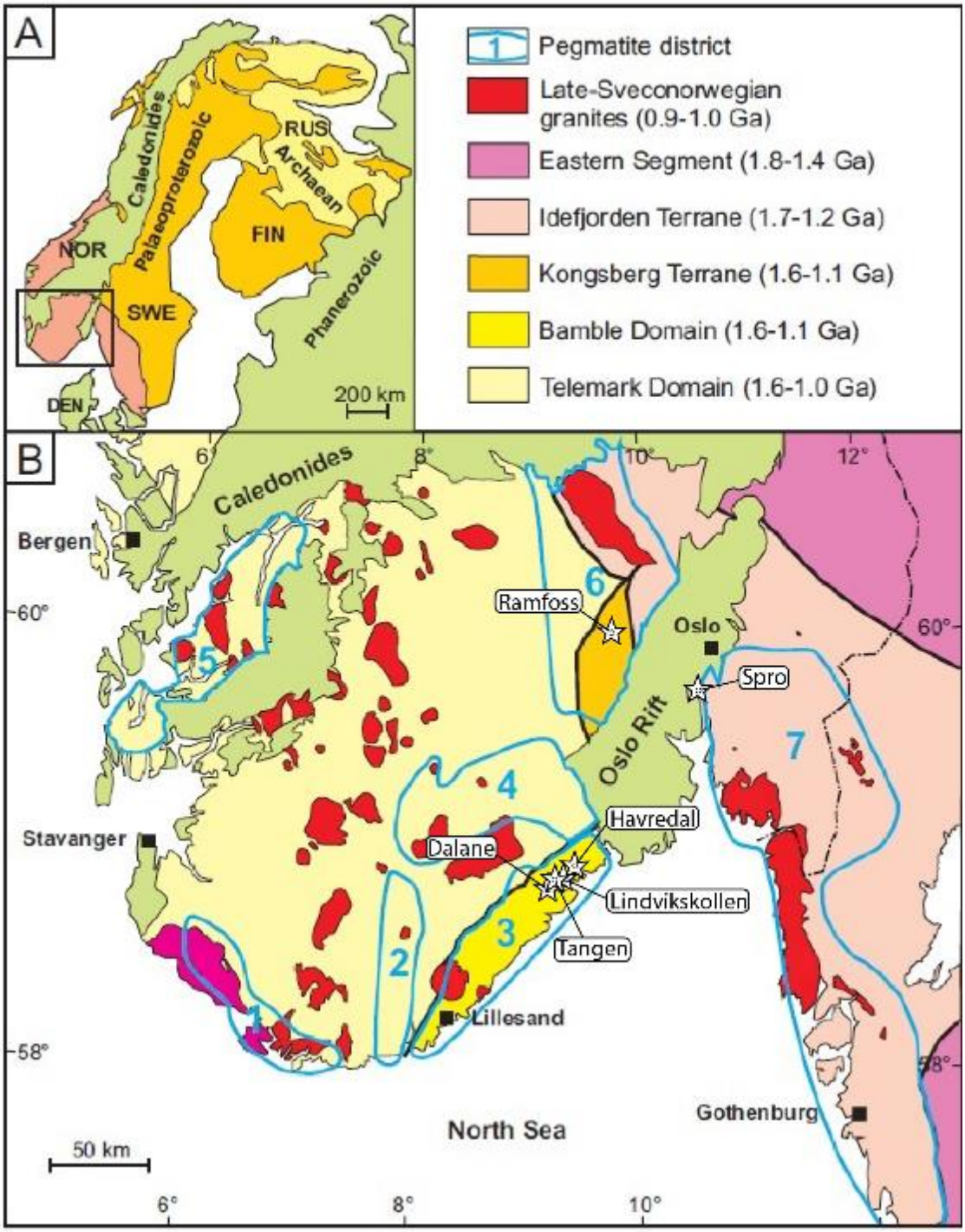

Figure 6-1 - The Sveconorwegian pegmatite province and location of the studied pegmatites (stars). **A:** Simplified map of Fennoscandia, showing the location of map B. Sveconorwegian orogeny is represented by the pinkish areas. **B:** Simplified geological map of southern Norway and parts of southwestern Sweden. The pegmatite districts of the Sveconorwegian pegmatite province are framed by blue lines: 1- Mandal; 2- Setesdal; 3- Bamble; 4- Nissedal; 5- Hardanger; 6- Buskerud; 7- Østfold-Halland. Map modified from Müller *et al.* (2015).

Table 6-1 - Investigated pegmatites, the pegmatite district/field and tectonic unit to which they belong, their host rocks and the age of emplacement of the pegmatite. [1] Müller *et al.* (2017) [2] Rosing-Schow *et al.* (2019)

Pegmatite	District/Field	Unit	Host rocks	Age of emplacement
Lindvikskollen	Kragerø pegmatite field	Bamble Sector	Metagabbro Albitite	1090-1030 Ma[1]
Tangen	Kragerø pegmatite field	Bamble Sector	Metagabbro	1082 ± 4.5 Ma[2]
Havredal	Kragerø pegmatite field	Bamble Sector	Gneiss-migmatite Amphibolite Metagabbro	-
Dalane	Kragerø pegmatite field	Bamble Sector	Migmatized gneiss Amphibolite gneiss	-
Ramfoss	Kongsberg-Modum pegmatite district	Kongsberg Sector	Quartzite	-
Spro	Østfold-Halland pegmatite district	Idefjorden 'Terrane'	Amphibole gneiss Spro granite	1036 ± 2 Ma[2]

6.1. Investigated pegmatites from the Kragerø pegmatite field - Bamble pegmatite district

The Bamble pegmatite district encompasses almost entirely the Bamble Sector. This district has one of the highest densities of pegmatite occurrences within the orogen, which are mainly grouped in the pegmatite fields: Glamsland-Lillesand, Froland, Arendal, Søndeled, and Kragerø. The Bamble pegmatites are classified as simple abyssal, primitive rare-element REE, and muscovite rare-element REE pegmatites with NYF affinity (Müller *et al.*, 2017). Some pegmatites exhibit albite replacement zones, which is why they are considered as chemically evolved NYF pegmatites, such as the Tangen and Sjåen pegmatites near Kragerø.

The Kragerø pegmatite field is composed of about 100 pegmatites (Figure 6-2). The highest density of pegmatite bodies occurs in the islands between the towns of Kragerø and Valle. The pegmatites from the Kragerø field are slightly deformed, which implies a syn- to post-kinematic formation in respect to the Sveconorwegian orogeny. They belong to the first (I) pegmatite

formation period described by Müller *et al.* (2017), in which their emplacement age is restricted from 1094 to 1060 Ma. The pegmatite melt emplacement slightly postdates the amphibolite-facies peak metamorphism (1140 – 1080 Ma) in the area.

6.1.1. Lindvikskollen pegmatite

The Lindvikskollen pegmatite lies on the Storkollen-Lindvikskollen hill, c. 2.5 km W of the town of Kragerø (Figure 6-2). The body is about 500 m long and up to 200 m wide, striking E-W and dipping ~30º to N (Bjørlykke, 1937). Major minerals include K-feldspar, plagioclase, quartz and biotite, these crystals may reach a couple meters in the intermediate zone. Accessory minerals comprise schorl, muscovite, allanite, euxenite-(Y), apatite, calcite, magnetite, yttrotitanite, ilmenite, hellandite-(Y), gadolinite and thorite. The Lindvikskollen pegmatite is the type locality of hellandite-(Y), which was first described by Brøgger (1903). The pegmatite formed between c. 1090 and 1030 Ma (U-Pb columbite group minerals), and intruded a metagabbro body (Müller *et al.*, 2017). This metagabbro may belong to the same suite of intrusions as the Ødegården metagabbro (close to the Havredal pegmatite; Figure 6-2) which yield an U-Pb zircon age of 1149 ± 7 Ma (Engvik *et al.*, 2011). In Lindvikskollen, the metagabbro is partially metasomatized to albitite. The pegmatite cross-cuts the albitites, which shows that the metasomatism of the metagabbro predates the pegmatite formation.

The albitites immediately W of the Lindvikskollen pegmatite were mined from 1901 to 1950 for rutile used as Ti ore. About 3000 tons rutile concentrate was produced (Bugge, 1978). The deposit was reinvestigated by A/S Sydvaranger in the mid 1970's. Five drill holes with a total length of 838 m were drilled. According to Bugge (1978) the deposit contains about 3 million tons of albitite (kragerøite) with an average grade 2 wt.% rutile. Today the deposit is too small to be of economic interest.

6.1.2. Tangen pegmatite

The Tangen pegmatite lies 4 km W of the town of Kragerø (Figure 6-2). The zoned but irregular body is about 40 m long and up to 15 m wide. The major minerals consist of quartz, oligoclase, and K-feldspar (Bjørlykke, 1937). Biotite and muscovite have not been found. Accessory minerals include allanite-(Ce), magnetite, fluorapatite, zircon, phenakite, columbite-(Fe) – columbite-(Mn) series, schorl, and topaz. The pegmatite is characterized by several cleavelandite replacement zones that are particularly well-developed in the western part of the body. Columbite group minerals form well-developed crystals embedded in cleavelandite. The Tangen pegmatite was dated, giving an age of emplacement of 1082 ± 4.5 Ma (U-Pb columbite; Müller *et al.*, 2017). The Tangen pegmatite intruded the same metagabbro body as the Lindvikskollen pegmatite.

6.1.3. Dalane pegmatite

The Dalane pegmatite is found 3 km SW of the town of Sannidal (Figure 6-2), it forms a c. 50 m long and up to 6 m wide pegmatite lens which strikes E-W. The pegmatite shows a distinct zoning with a granitic border zone, wall zone and quartz core. Major minerals are K-feldspar, plagioclase, quartz, biotite, and muscovite. Black tourmaline is a minor mineral with crystal length of up to 50 cm. Accessory minerals include garnet, beryl, fergusonite, zircon, monazite, xenotime and allanite (orthite; Bjorlykke, 1935). According to the geological map of the Bamble Sector (Marker *et al.*, 2020), the Dalane pegmatite intrudes strongly migmatized gneiss with layers of amphibolite and migmatitic amphibolite.

6.1.4. Havredal pegmatite

The Havredal pegmatite forms a E-W striking dyke-like body and it is c. 100 m long and up to 15 m wide. The pegmatite is exposed in a small mine (10 x 15 m) where muscovite was produced in 1943/44, 3 km N from the town of Valle (Figure 6-2). The zoning is only weakly developed, and the major minerals comprise K-feldspar, plagioclase, and quartz. Tourmaline is a very common minor mineral, while biotite is rare. This pegmatite is characterized by the occurrence of hematite masses up to 20 cm, which were mined in the 17th century. The host rocks are gneiss-migmatites, amphibolites, and metagabbros (Marker *et al.*, 2020). The metagabbros of

the Havredal (Ødegården) area have a magmatic protolith U-Pb zircon age of 1149 ± 7 Ma (Engvik *et al.*, 2011). Similarly to the Lindvikskollen, this metagabbro underwent partial albitization. The albitization event was dated by the same authors, which yielded U-Pb ages for metasomatic rutile between 1090 and 1084 Ma.

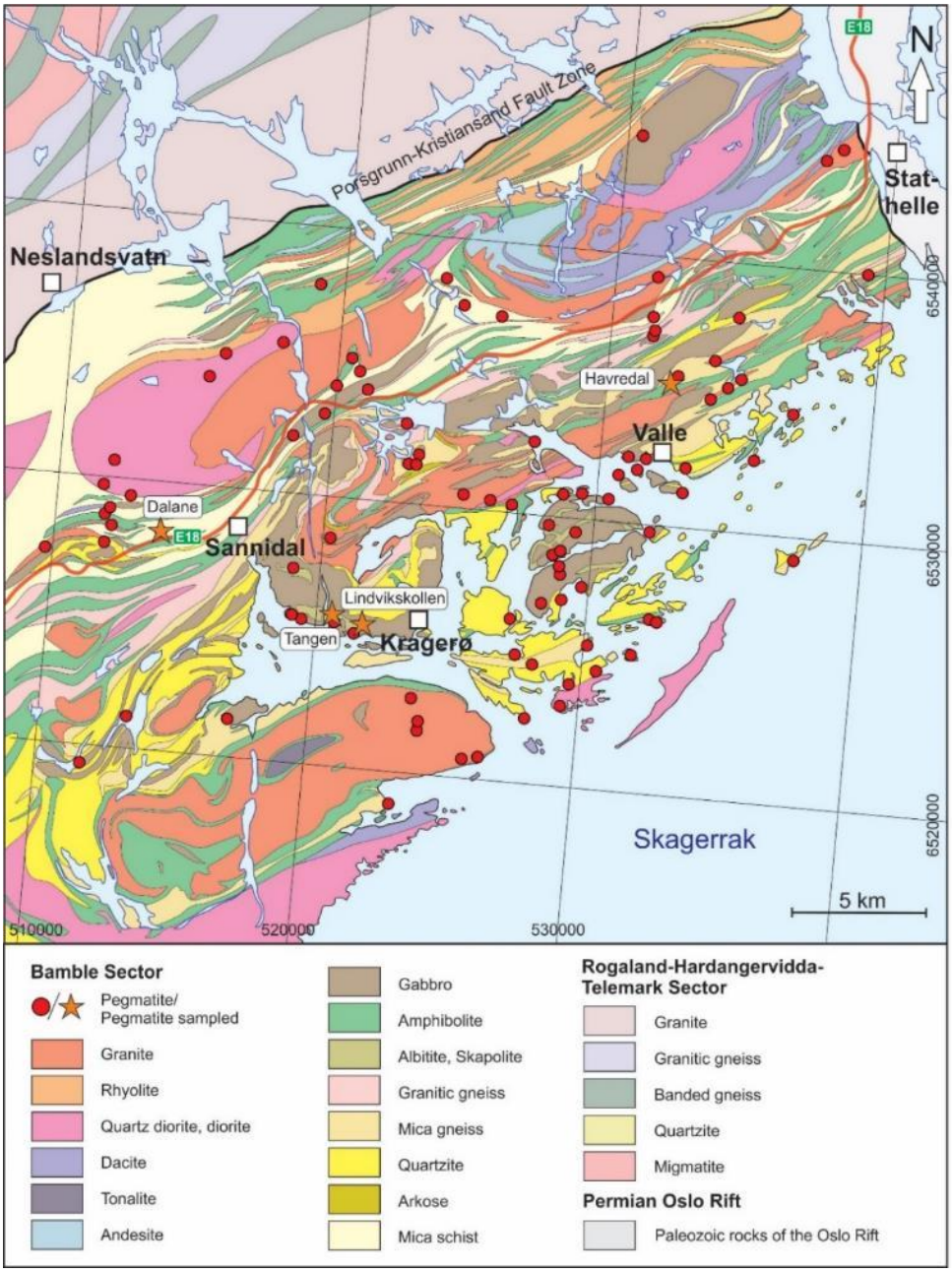

Figure 6-2 - Geological map of the Northern part of the Bamble Sector, showing the pegmatite occurrences in the area. The investigated pegmatites are represented by an orange star and their respective names. From Müller *et al.* (2021).

6.2. Other investigated pegmatites from the South Norwegian pegmatite province

6.2.1. Ramfoss pegmatite of the Kongsberg-Modum pegmatite district

The Ramfoss pegmatite is part of the Kongsberg-Modum pegmatite district, of the Kongsberg Sector, 9 km NW of Vikersund (Figure 6-1). This pegmatite forms a relatively small (15 x 6 m), isolated body. Major minerals are K-feldspar, plagioclase, albite, quartz, and muscovite. Other minerals occurring in the pegmatite are allanite-(Y), black tourmaline and titanite. Pb-Pb mineral isochron dating of the Ramfoss pegmatite yielded an age of 1045 ± 12 Ma (Andersen & Grorud, 1998). The Ramfoss pegmatite host rocks are pure quartzite to feldspar-bearing quartzite (Viola *et al.*, 2016). The quartzites of the Modum Complex were deposited after 1467 ± 33 Ma (Bingen *et al.*, 2001; Bingen & Viola, 2018). Later, during the Sveconorwegian orogeny they were subjected to upper amphibolite-facies metamorphism. Nevertheless, other lithologies also occur near this pegmatite (1.2 to 2 km away) such as amphibolites, metagabbro, granitic gneisses and metagranodiorites (Viola *et al.*, 2016).

6.2.2. Spro pegmatite of the Østfold-Halland pegmatite district.

The Spro pegmatite is part of the Østfold-Halland pegmatite district, of the Idefjorden 'Terrane' (Figure 6-1). Spro is a large, isolated body c. 230 m long, it occurs as a vertical dyke with variable thickness, from 1 up to 25 m. Major minerals include quartz, muscovite, K-feldspar and albitic plagioclase. Overall, the pegmatite is homogenous. However, there is an increase in crystal sizes, from the wall zone towards the core. The pegmatite has 3 crystallization stages (Faria, 2019), from oldest to youngest: (1) Coarse-grained to megacrystals of microcline, muscovite, quartz, oligoclase-albite, monazite-(Ce), thorite, smarskite-(Y), columbite-(Fe), euxenite-(Y) and possibly beryl (Faria, 2019; Raade, 1965). (2) Irregular cross-cutting veins of fine-grained sugary albite, in association with tourmaline, muscovite, fluorite, topaz, beryl, microlite group minerals, apatite, and calcite. (3) The third stage involved the alteration of the previous minerals (Faria, 2019). The core has an abundancy of muscovite in comparison with the other zones. At the wall zone the accessory minerals are scarcer, and plagioclase is more abundant than the other minerals.

In its replacement zones, the major minerals are cross-cut and partially replaced by albite. The age of emplacement of the Spro pegmatite is 1036 ± 2 Ma (Rosing-Schow *et al.*, 2019),

The Spro pegmatite host rocks consist of amphibole gneisses and the deformed Spro granite. The protolith ages of the amphibolitic rocks are between 1600-1900 Ma (Jacobsen & Heier, 1978; Pedersen, 1978; Skiöld, 1976; Versteeve, 1974). The Spro granite has a crystallization age of between 1542-1493 Ma (Pozer, 2008). During the Sveconorwegian orogeny these were deformed under amphibolite-facies metamorphism which peaked at 1050 Ma, in addition to some migmatization (Graversen, 1984; Magnusson, 1960; Swensson, 1990).

7. Samples and Methods

7.1. Sampling

During fieldwork, 7 whole rock samples and 12 tourmaline samples were collected for this thesis. From the NHM collection, 5 pegmatite tourmaline samples and 1 host rock tourmaline sample were analysed. In addition, 3 tourmaline samples of the Spro pegmatite, previously studied through EPMA and SIMS by Faria (2019), were analysed by LA-ICP-MS. Table 7-1 presents a simplified list of the analysed samples. An extended sample list, with the addition of mineral descriptions, sampling coordinates and type of sample preparation is presented in Appendix A Table 1.

Table 7-1 - Sample List. Lind: Lindvikskollen; WR: Whole Rock. * Samples previously analysed by Faria (2019).

Sample number	Locality	Rock/ Mineral type	Location within pegmatite	Analyses	Sample source
20252	Lindvikskollen	Tourmaline	Core	EPMA, LA-IP-MS, SIMS (B-isotope)	NHM collection
20241	Tangen	Tourmaline	Core	EPMA, LA-IP-MS, SIMS (B-isotope)	NHM collection
20216	Havredal	Tourmaline	Intermediate zone	EPMA, LA-IP-MS, SIMS (B-isotope)	NHM collection
13051920	Dalane	Tourmaline	Intermediate zone	EPMA, LA-IP-MS, SIMS (B-isotope)	NHM collection
20091	Ramfoss	Tourmaline	-	EPMA, LA-IP-MS, SIMS (B-isotope)	NHM collection
05061804	Spro	Tourmaline	Host rock Gneiss	EPMA, LA-IP-MS, SIMS (B-isotope)	NHM collection
12062004	Lind. W mine	Tourmaline	Core	EPMA, LA-ICP-MS	Field
12062007	Lind. W mine	Tourmaline	Intermediate zone	EPMA, LA-ICP-MS	Field
12062008	Lind. W mine	Tourmaline	Intermediate zone	EPMA, LA-ICP-MS	Field
12062009	Lind. W mine	Tourmaline	Wall zone 0.5 m from contact	EPMA, LA-ICP-MS	Field
12062014	Lind. W mine	Bulk wall zone	Wall zone	WR analysis	Field
12062015	Lind. W mine	Metagabbro	Host rock	EPMA, LA-ICP-MS WR analysis	Field

Sample number	Locality	Rock/ Mineral type	Location within pegmatite	Analyses	Sample source
12062016	Lind. W mine	Tourmaline in Albitite	Host rock	EPMA, LA-ICP-MS WR analysis	Field
12062018	Lind. W mine	Tourmaline	Core (Not *in situ*)	EPMA, LA-ICP-MS	Field
12062020	Lind. W mine	Tourmaline in Metagabbro	Host rock	EPMA, LA-ICP-MS	Field
12062021	Lind. E mine	Tourmaline	Intermediate zone	EPMA, LA-ICP-MS	Field
12062022	Lind. E mine	Tourmaline	Core	EPMA, LA-ICP-MS	Field
12062023	Lind. E mine	Tourmaline	Core	EPMA, LA-ICP-MS	Field
12062024	Lind. E mine	Tourmaline	Intermediate zone	EPMA, LA-ICP-MS	Field
12062025	Lind. E mine	Tourmaline	Intermediate zone	EPMA, LA-ICP-MS	Field
12062026	Lind. rutile mine tailings	Albitite (Rutile-rich)	Host rock	EPMA, LA-ICP-MS WR analysis	Field
12062027	Lind. rutile mine tailings	Albitite (Rutile-poor)	Host rock	WR analysis	Field
12062029	Lind. road cut	Monzonitic gneiss	-	WR analysis	Field
12062030	Lind. road cut	Tourmaline in granitic dyke	-	EPMA, LA-ICP-MS	Field
12062031	Lind. road cut	Granitic dyke	-	WR analysis	Field
690a*	Spro	Tourmaline	Pegmatite	EPMA, LA-ICP-MS	NHM collection
690b*	Spro	Tourmaline	Pegmatite	EPMA, LA-ICP-MS	NHM collection
690c*	Spro	Tourmaline	Pegmatite	EPMA, LA-ICP-MS	NHM collection
20160*	Spro	Tourmaline	Pegmatite	EPMA	NHM collection
18081715*	Spro	Tourmaline	Pegmatite	EPMA	NHM collection

7.2. Sample preparation

7.2.1. Rock Crushing

Rock samples were crushed and split to obtain representative samples of the host rocks and pegmatites for whole rock analysis. The crushing of rock samples was performed at the department of Geosciences of the University of Oslo, with the guidance and assistance of Chief Engineer Gunborg Bye Fjeld. To obtain a representative crushed rock of the samples without sample contamination, the following steps were methodically performed in all samples:

(1) Cutting of the samples with the diamond microsaw: The rocks were cut into pieces up to 10 cm^3, as to avoid damage and obstruction in the jaw crusher (Figure 7-1A).

(2) Sample washing: The samples were washed under running water and then further cleaned in an ultrasonic water bath, this way removing any material that could have contaminated the sample during sampling, transport, storage and cutting.

(3) Drying: The rocks were dried in the oven for more than 12 hours, to eliminate any water content in the rock.

(4) Preparation of the equipment: a plastic bag was placed between the machine and the crushing plates to lessen the amount of sample that would come into contact with the machine. Also, a bucket with two plastic bags was placed under the machine to gather the crushed sample.

(5) Crushing: The multiple pieces of each rock sample were dropped into the jaw crusher one by one, attentively watching if the crushed sample was falling properly in the plastic bags (Figure 7-1B).

(6) Splitting: The resulting crushed rock was then separated into halves using a sample splitter (Figure 7-1C). Using this method, 30g representative of the rock were saved for whole rock analysis and 300g were kept for reference (Figure 7-1D).

To prevent sample contamination a meticulous cleaning procedure was performed before the crushing of each rock sample began. This included dismantling the jaw crusher between each sample, and vacuuming, blowing compressed air, polishing, wiping with alcohol, and drying with compressed air all the surfaces and pieces of the jaw crusher that might or have come into contact

with the rock. The desk surface had to be vacuumed and cleaned with alcohol, since the method created a large amount of dust. The sample splitter needed to be cleaned with running water, submerged in the ultrasonic bath, cleaned with alcohol, and finally dried with compressed air.

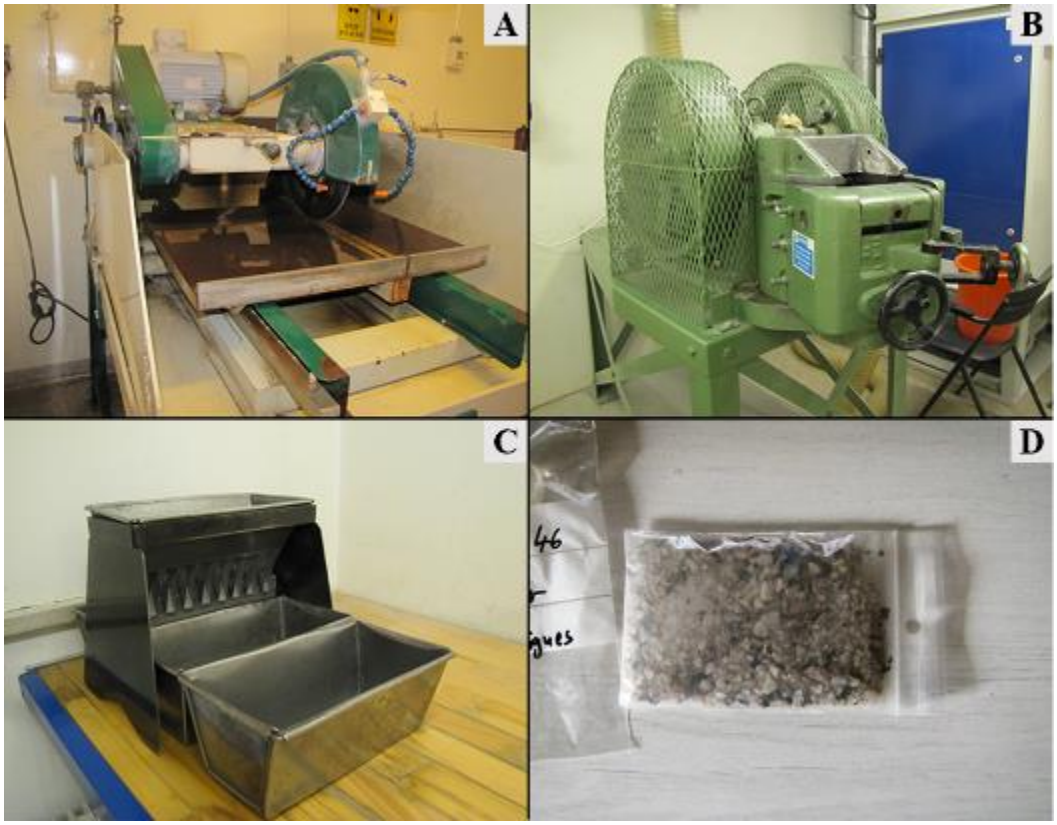

Figure 7-1 - Rock Crushing at the UiO-Department of Geosciences. **A:** Diamond microsaw. **B:** Jaw crusher**. C:** Splitter. **D:** Resulting crushed rock.

7.2.2. Thick section preparation

11 rock samples were used to make thick sections. The samples were cut on a diamond rotary saw at the NHM – Mineralogy Lab (Økern). The cuts were made considering important aspects of the rock, such as the orientation of the minerals, presence of minerals of interest, non-altered parts of the rocks, etc. Afterwards, the samples were sent to the UiO - Department of Geosciences where polished 300 µm thin sections were made by Senior Engineer Salahalldin Akhavan. These samples were then analysed in the SEM, EPMA and LA-ICP-MS.

7.2.3. Preparation of tourmaline crystals as epoxy mounts

Mineral samples for micro analytical investigations were assembled and prepared in 1-inch (24 mm) epoxy mounts. The samples were prepared in the NHM – Mineralogy Lab (Økern). The preparation of an epoxy mount comprises the following steps:

(1) Small mineral pieces (3-5 mm) were grinded with silicon carbide 80 grit powder on a glass slab on one side to get a flat surface.

(2) A doubled sided tape was placed on top of a glass slab that served as a hard and homogeneous flat surface.

(3) The outline of the plastic support cup was drawn on the tape with a North mark orientation (N in Figure 7-2A).

(4) The samples were placed with the flat face on the tape inside the outlined surface (Figure 7-2A).

(5) The position of the samples was recorded with sketches and photographs (Figure 7-2A).

(6) The support cup was placed once again on the tape, plasticine was then put around the bottom as to prevent any leakage (Figure 7-2B).

(7) For precaution in the case of leakages, before the next steps were carried out the cast was placed on a disposable box.

(8) To make the epoxy glue that is going to hold the sample, epofix resin and epofix hardener (in a ratio 25:3) were mixed in a disposable container.

(9) The glue was mixed for around 1 minute, slowly as to make the least amount of bubbles.

(10) The epoxy glue was carefully poured in the support cup to prevent the samples from falling or moving.

(11) It was then left to solidify for at least 24 hours.

(12) After the epoxy glue was set, the support cast was removed and sent for surface polishing to the Department of Geoscience at UiO.

The result is a group of tourmaline samples in an epoxy mount as shown in Figure 7-3 (Epoxy cast 41). In total 6 epoxy mounts were prepared.

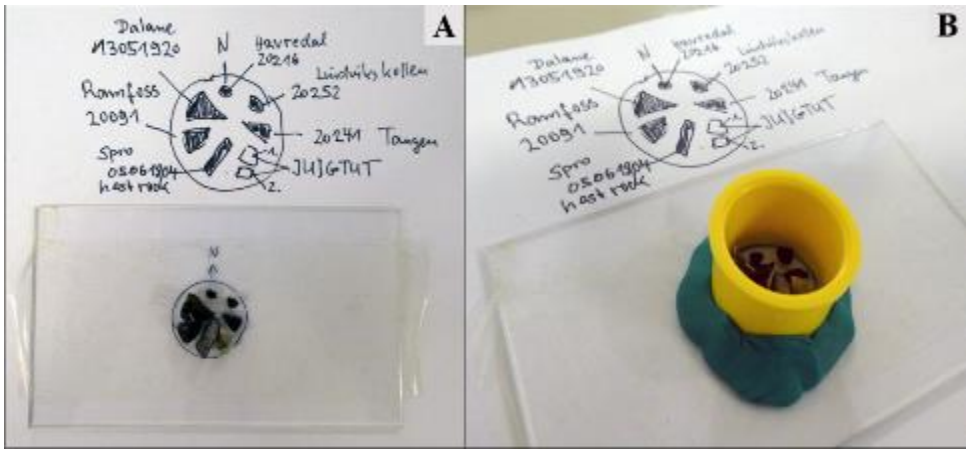

Figure 7-2 - **A:** Preparation of epoxy cast 41. Tourmaline samples glued to transparent tape, and sketch map of each sample location. **B:** Preparation of epoxy cast 41. Placing of support cup and plasticine around it to prevent leakages after the glue is poured in.

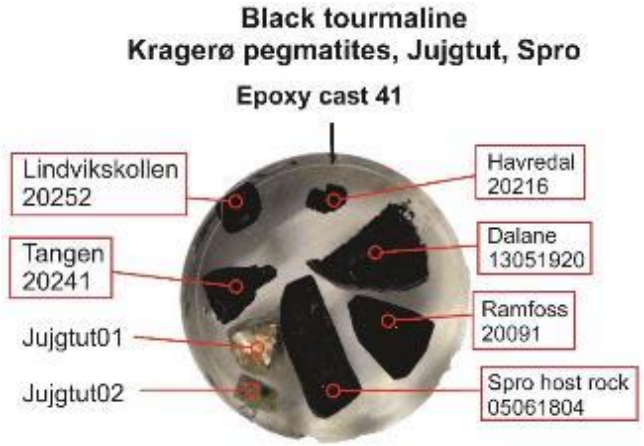

Figure 7-3 - Epoxy cast 41 showing analysed tourmaline samples (red rectangles). This samples were analysed by EPMA, LA-ICP-MS and SIMS.

7.2.4. Carbon coating of the epoxy mounts

With the purpose of performing SEM and EPMA, thin sections and epoxy mounts needed to be coated with carbon. The coating was performed at the NHM – Mineralogy Lab (Økern) under the instruction and aid of the laboratory manager Ph.D. Nélia Castro.

The carbon coating is done through evaporation of a thin layer (5-50 nm) of conductive carbon on the surface of the sample. This carbon layer is thin enough that it covers the surface

without masking the morphology of the sample. It produces conductivity on the sample surface dissipating the charging, prevents overcharge and thermal damage to the sample, and improves the imaging of samples (Echlin, 2009).

The equipment used was a 'AGAR auto carbon coater'. The coating of the sample involved the following steps:

(1) Sharpening of the carbon rod source, if needed.

(2) Placement of the sample on the sample holder inside the evaporation chamber, followed by adjusting the height of the sample as to not touch the carbon rod source.

(3) Closing the top-plate and turning on the equipment and the chamber pump.

(4) The evaporation chamber was pumped until it reached a pressure below 0.05 mb.

(5) The setting chosen were AUTO mode, 5.0 V and a 10 second timer.

(6) The coating process was then started and repeated until the coating was acceptable.

7.3. Methods

7.3.1. Whole Rock Analysis

Whole rock analyses were performed on selected samples of the Lindvikskollen area rocks, presented in Table 7-1. The analyses were conducted by the commercial laboratory Activation Labs in Canada. To do so, 30 g of each crushed rock were sent to the laboratory. Table 7-2 shows the analytical method and limit of detection (LOD) of every analysed oxide and element. The applied analytical methods were the following:

(1) The Fusion / X-ray fluorescence (**FUS-XRF**) analytical method was performed to analyse major oxides. Before the sample is fused, it is first roasted at 1000ºC for 2 hours. The loss on ignition (LOI) fraction of the sample is determined by the difference in weight before and after the sampled is roasted (Actlabs, 2021). The fusion of the samples involves the creation of a fusion disc: 0.75 g of the samples were mixed with a blend of 9.75 g of lithium metaborate and lithium tetraborate with lithium bromide. The samples were then fused in platinum crucibles and analysed on a Panalytical Axios Advanced Wavelength dispersive XRF (Actlabs, 2021). XRF analysis

involves the bombardment of a sample with high-energy X-rays or gamma rays, that cause the excited sample to emit secondary or fluorescent X-rays, which are characteristic of a specific element.

(2) The Fusion/Ion Selective Electrode (**FUS-ISE**) method was used to analyse fluoride. This method uses 0.2 g of rock sample that were fused with a mixture of lithium metaborate and lithium tetraborate in an induction furnace in order to release fluoride ions (Actlabs, 2021). Subsequently, the sample was dissolved in diluted nitric acid, the resulting solution was complexed and the ionic strength adjusted. The fluoride-ion activity was measured by the immersion of a fluoride ion electrode in the solution, and further analysed by an automated fluoride analyser from Mandel Scientific (Actlabs, 2021).

(3) The sodium peroxide fusion/Inductive coupled plasma and inductive coupled plasma Mass Spectrometry (**FUS-Na_2O_2** and **FUS-MS-Na_2O_2**, respectively) methods were performed to analyse most of the elements. Crushed samples were fused with sodium peroxide in a zirconium crucible, and then acidified with concentrated nitric and hydrochloric acid. Next, the resulting solutions were diluted and measured by ICP and ICP-MS (Actlabs, 2021). ICP refers to the ICP-optical emission spectrometry (ICP-OES) analytical method, ICP is used in a sample which causes the samples' excited atoms and ions to emit electromagnetic radiation, the wavelengths produced are characteristics of each element.

Table 7-2 – Limits of detection of the whole rock analyses. A.M.: Analysis Method. LOD: Limit of detection.

Element		A.M.	LOD	Element		A.M.	LOD
SiO_2	%	FUS-XRF	0.01	**In**	ppm	FUS-MS-Na_2O_2	0.2
Al_2O_3	%	FUS-XRF	0.01	**K**	%	FUS-Na_2O_2	0.1
Fe_2O_3 (T)	%	FUS-XRF	0.01	**La**	ppm	FUS-MS-Na_2O_2	0.4
MgO	%	FUS-XRF	0.01	**Li**	ppm	FUS-MS-Na_2O_2	3
CaO	%	FUS-XRF	0.01	**Mg**	%	FUS-Na_2O_2	0.01
Na_2O	%	FUS-XRF	0.01	**Mn**	ppm	FUS-MS-Na_2O_2	3
K_2O	%	FUS-XRF	0.01	**Mo**	ppm	FUS-MS-Na_2O_2	1
TiO_2	%	FUS-XRF	0.01	**Nb**	ppm	FUS-MS-Na_2O_2	2.4
P_2O_5	%	FUS-XRF	0.01	**Nd**	ppm	FUS-MS-Na_2O_2	0.4
MnO	%	FUS-XRF	0.001	**Ni**	ppm	FUS-MS-Na_2O_2	10
Total	%	FUS-XRF	0.01	**Pb**	ppm	FUS-MS-Na_2O_2	0.8
F	%	FUS-ISE	0.01	**Pr**	ppm	FUS-MS-Na_2O_2	0.1
Al	%	FUS-Na_2O_2	0.01	**Rb**	ppm	FUS-MS-Na_2O_2	0.4
As	ppm	FUS-MS-Na_2O_2	5	**S**	%	FUS-Na_2O_2	0.01
B	ppm	FUS-MS-Na_2O_2	10	**Sb**	ppm	FUS-MS-Na_2O_2	2
Ba	ppm	FUS-MS-Na_2O_2	3	**Se**	ppm	FUS-MS-Na_2O_2	8
Be	ppm	FUS-MS-Na_2O_2	3	**Si**	%	FUS-Na_2O_2	0.01
Bi	ppm	FUS-MS-Na_2O_2	2	**Sm**	ppm	FUS-MS-Na_2O_2	0.1
Ca	%	FUS-Na_2O_2	0.01	**Sn**	ppm	FUS-MS-Na_2O_2	0.5
Cd	ppm	FUS-MS-Na_2O_2	2	**Sr**	ppm	FUS-MS-Na_2O_2	3
Ce	ppm	FUS-MS-Na_2O_2	0.8	**Ta**	ppm	FUS-MS-Na_2O_2	0.2
Co	ppm	FUS-MS-Na_2O_2	0.2	**Tb**	ppm	FUS-MS-Na_2O_2	0.1
Cr	ppm	FUS-MS-Na_2O_2	30	**Te**	ppm	FUS-MS-Na_2O_2	6
Cs	ppm	FUS-MS-Na_2O_2	0.1	**Th**	ppm	FUS-MS-Na_2O_2	0.1
Cu	ppm	FUS-MS-Na_2O_2	2	**Ti**	%	FUS-Na_2O_2	0.01
Dy	ppm	FUS-MS-Na_2O_2	0.3	**Tl**	ppm	FUS-MS-Na_2O_2	0.1
Er	ppm	FUS-MS-Na_2O_2	0.1	**Tm**	ppm	FUS-MS-Na_2O_2	0.1
Eu	ppm	FUS-MS-Na_2O_2	0.1	**U**	ppm	FUS-MS-Na_2O_2	0.1
Fe	%	FUS-Na_2O_2	0.05	**V**	ppm	FUS-MS-Na_2O_2	5
Ga	ppm	FUS-MS-Na_2O_2	0.2	**W**	ppm	FUS-MS-Na_2O_2	0.7
Gd	ppm	FUS-MS-Na_2O_2	0.1	**Y**	ppm	FUS-MS-Na_2O_2	0.1
Ge	ppm	FUS-MS-Na_2O_2	0.7	**Yb**	ppm	FUS-MS-Na_2O_2	0.1
Ho	ppm	FUS-MS-Na_2O_2	0.2	**Zn**	ppm	FUS-MS-Na_2O_2	30
Hf	ppm	FUS-MS-Na_2O_2	10				

7.3.2. Scanning Electron Microscopy

The scanning electron microscopy (SEM) was performed to identify micro inclusions in tourmalines, the paragenesis and textural relationship with other minerals and to reveal possible intra-crystal zoning. In addition, high-resolution backscattered electron images (BSE) were taken, which were used as sample reference images for subsequent EPMA, LA-ICP-MS and SIMS analyses. The analyses were performed under the supervision and instruction of the laboratory manager Ph.D. Nélia Castro at the NHM – Mineralogy Lab (Økern).

The SEM is an instrument used to take magnified images which reveal microscopic-scale information of a sample, from their size, shape, composition, crystallography, among other physical and chemical properties. The operation of the SEM mainly involves the creation of a finely focused beam of energetic electrons emitted from an electron source. The electrons are emitted and accelerate to high energy (0.1 to 30 kV), after this the electron beam is modified to reduce its diameter and to scan the focused beam in a raster (x-y) pattern, in individual places in the sample. At each location in the scan pattern, the scanning beam interacts with the sample and produces two outgoing electron products, backscattered electrons (BSE) and secondary electrons (SE).

BSEs are beam electrons that, after going through scattering and deflection by the electric fields of the atoms in the sample, come out with a large fraction of their incident energy intact. SE are electrons that break free from the sample surface, at low kinetic energies, after beam electrons have ejected them from atoms in the sample. These outgoing electron signals are measured using one or more electron detectors, a SE detector and a dedicated BSE detector. The detectors measure the signal at each scan location on the sample. This signal is digitized into the computer and then used to determine the gray level at the location of scanning in the computer screen, creating a pixel.

In order to minimize the unwanted scattering that the beam electrons, the BSE and SE would go through when encountering atoms of atmospheric gasses, the electron-optical column and the specimen chamber must be isolated under high vacuum conditions.

The SEM instrument used is the Hitachi S-3600N. The images were taken with a BSE detector in high vacuum (< 1 Pa), with 15 kV accelerating voltage, at a working distance of 15 mm, and the beam diameter size was in the range of c. 150 – 250 nm. The software used by this

equipment is the Hitachi S-3600. The individual images were subsequently combined to create a map (or composite image) of each sample or of important points in the sample. Some of these images are presented in Appendix D.

7.3.3. Electron probe microanalysis

The electron probe microanalysis (EPMA), or electron microprobe analysis (EMPA) method was performed to determine the major and minor element concentrations of the tourmaline samples that were selected after SEM analysis. This method was conducted at the UiO - Department of Geosciences, under the supervision and aid of Senior Engineer Muriel Erambert.

The EPMA is an instrument used for chemical analysis of small areas of solid samples. In principle it is the same instrument as a SEM, with further capability of chemical analysis.

In an EPMA an electron beam is focused on a small area of the sample. This beam will release heat, energy, cathodoluminescence, BSE, SE, and X-rays from the sample. The X-rays will be emitted at a characteristic frequency and detected by an electron microprobe; this process is what makes the chemical analysis possible. The wavelength and energy of the X-rays determine the elements present in the sample, and by comparing the intensities of the characteristic X-rays from the sample with intensities of standard materials (pure elements or compounds of known composition) it is possible to determine the concentrations of the elements present.

The instrument used was an Electron microprobe Cameca SX100 with 5 WDS spectrometers. The software of the EPMA shares the name of the instrument. The conditions for the analyses were the following: accelerating voltage of 15kV, beam current of 15 nA and beam size from focused beam to 3 μm in diameter, the scanning time peak was 10 s. The calibration standards used were the compounds: Al_2O_3, MgO, Cr_2O_3 and metal Fe; and the minerals: Wollastonite (for Si, Ca), Pyrophanite (for Ti, Mn), Orthoclase (for K), Albite (for Na) and Fluorite (for F).

Table 7-3 - EPMA mean detection limits of each analysed element.

Mean detection limit (ppm)										
	Si	**Al**	**Ti**	**Fe**	**Mg**	**Mn**	**Na**	**Ca**	**K**	**F**
20252	349	325	298	688	335	604	359	453	238	2072
20241	344	323	306	741	318	639	428	461	249	2116
13051920	339	337	291	658	302	577	336	446	239	2109
20216	331	333	287	622	315	547	338	424	239	2198
20091	341	328	293	641	347	570	336	473	234	2191
5061804	340	334	288	623	315	578	335	439	239	2085
12062004	340	325	301	685	343	590	359	458	239	2471
12062007	339	330	297	698	334	596	357	460	243	2457
12062008	340	325	299	685	342	596	358	466	239	2620
12062009	337	331	303	705	333	596	369	455	242	2341
12062018	334	321	299	688	341	588	359	469	241	2664
12062021	342	324	301	679	333	589	363	461	244	2695
12062022	340	321	301	701	337	601	363	454	240	2349
12062023	336	325	301	685	329	595	368	446	244	2342
12062024	343	330	303	708	345	593	363	454	246	2501
12062025	342	330	303	708	336	593	367	456	240	2427
12062030	339	336	298	701	321	607	373	454	246	2633

7.3.4. Laser ablation inductively coupled plasma mass spectrometry

The laser ablation inductively coupled plasma mass spectrometry (LA-ICP-MS) method was performed in selected tourmaline samples, at the UiO - Department of Geosciences, under the supervision and aid of Senior Engineer Magnus Kristoffersen.

LA-ICP-MS is a multi-element trace element technique that incorporates a quadrupole mass analyser. The fundamental principal of this method is elemental differentiation on the basis of atomic mass (Linge & Jarvis, 2009). The method starts when a focused laser beam strikes the surface of the tourmaline sample on selected points. This process, called laser ablation heats up, evaporates and ionises the sample, creating a plume of particles and ions that are then transported

to the inductive coupled plasma (Thomas, 2013). In the ICP the sample particles are ionised. Subsequently the excited ions are focused and transported to the mass spectrometer, which separates them based on their mass-to-charge ratio (Linge & Jarvis, 2009). A detector counts each individual ion by pulse counting, this means that each ion is translated into an electrical pulse. The number of pulses is related to the number of analysed ions in the sample. This process provides the absolute concentration of an element by comparing the signal produced by the sample with that registered from a calibration reference sample (Linge & Jarvis, 2009).

The equipment used was the Bruker Aurora Elite, from 2013, in combination with a Cetac LSX-213 G2 + laser microprobe, Cetac ASX-250 autosampler, a ESI one FAST sample introduction system, and its software Quantum. The software utilized to handle the data was Glitter (Griffin, 2008). The LA-ICP-MS procedure followed the analysis pattern presented on Figure 7-4. Every cycle consisted of 3 analysed points on a synthetic glass standard sample (NIST SRM 610), 16 points on the analysed tourmaline samples, 2 points on a basaltic glass standard sample (BCR-2G), and 2 points on a black tourmaline reference sample.

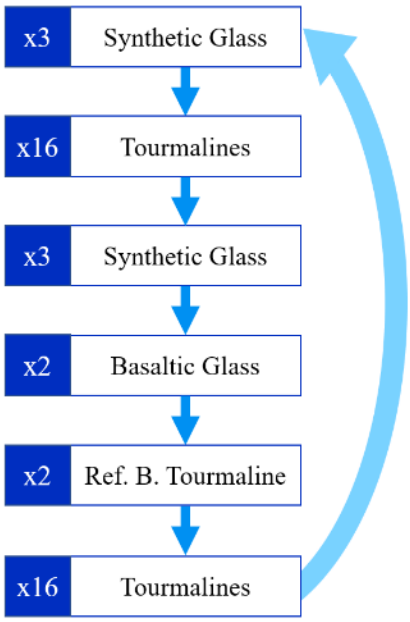

Figure 7-4 - LA-ICP-MS analysis sequence.

The analyses parameters needed to be adjusted for each tourmaline. The samples parameters are presented in Table 7-4 and the LOD are listed in Table 7-5. The composition of the reference and standard samples are presented in Appendix B Table 1.

7.3.5. Secondary ion mass spectrometry

The secondary ion mass spectrometry (SIMS) was used to analyse the B isotopes of the selected tourmaline samples. The SIMS method was performed at the GFZ German Research Centre for Geosciences in Potsdam, Germany, by Dr. Robert Trumbull. The equipment used was a CAMECA 1280-HR SIMS.

Table 7-4 - LA-ICP-MS analysis parameters used for each sample.

Sample	Spot size (µm)	Laser energy (%)	Laser Shot. Frequency (Hz)	Shutter delay (s)	Burst count
20252	100	10	10	10	400
20241	50	20	10	10	400
20216	100	10	10	10	400
13051920	100	10	20	10	800
20091	100	10	10	10	400
05061804	40	20	10	10	400
12062009	100	10	10	10	400
12062016	50	5	20	10	800
12062018	100	10	10	10	400
12062020	50	10	10	10	400
12062021	50	10	10	10	400
12062030	100	10	20	20	800
690a	100	10	20	10	800
690b	100	10	10	10	400
690c	100	10	20	10	800
Standard and reference samples					
NIST SRM 610	50	20	10	10	400
BCR-2G	50	20	10	10	400
Black Tour.	100	10	20	10	800

This method involves a focused ion beam that bombards the sample's surface, this causes the escape of secondary ions from defined spots of the sample which are then analysed by a mass analyser. SIMS uses an ion gun to create a precisely focused high energy primary ion beam that bombards the surface of the sample. Because of this bombardment, in the upper surface layers of the sample a collision cascade occurs and causes energy dissipation, which subsequently causes bonds to break and secondary particles to be emitted. These particles are mainly neutral, although a small percentage (~1%) is charged, either positively or negatively depending on the electric beam used. The secondary particles are then accelerated, focused, and analysed by a mass spectrometer, where they are separated according to their mass/charge ratio. The detection limit of the SIMS is in the part-per-billion range for many elements, due to its high sensitivity in comparison with other microbeam sampling techniques.

Table 7-5 - LA-ICP-MS limits of detection of each analyte, minimum, maximum and mean ppm values.

Element	Min	Max	Mean	Element	Min	Max	Mean
Li	0.08	1.55	0.47	**Y**	0	0.525	0.066
Be	0.02	0.40	0.13	**Zr**	0	2.860	0.934
Na	12.05	273.43	85.33	**Nb**	0.001	0.022	0.007
Mg	2.91	131.02	35.77	**Mo**	0.016	0.300	0.093
Al	59.65	2326.23	678.31	**Sn**	0.025	0.418	0.134
Si	251.78	4239.95	1368.93	**Sb**	0.008	0.169	0.045
P	0.91	14.77	4.73	**Cs**	0.006	0.106	0.034
K	3.70	60.78	20.10	**Ba**	0.019	0.307	0.100
Ca	14.23	246.13	84.78	**La**	0.001	0.020	0.007
Sc	0.04	0.76	0.25	**Ce**	0	0.352	0.026
Ti	0.75	32.65	9.22	**Pr**	0.0004	0.012	0.004
V	0.14	2.34	0.78	**Nd**	0.004	0.133	0.037
Cr	0.33	6.12	1.99	**Sm**	0.003	0.084	0.022
Mn	0.80	14.33	4.60	**Eu**	0.001	0.027	0.008
Co	0.01	0.29	0.09	**Lu**	0.0003	0.012	0.003
Ni	0.66	14.93	4.76	**Ta**	0	0.727	0.038
Cu	0.03	0.68	0.22	**W**	0.003	0.069	0.021
Zn	0.09	1.83	0.59	**Pb**	0.002	0.048	0.014
Ga	0.02	0.30	0.10	**Th**	0	0.016	0.004
Rb	0.01	0.19	0.06	**U**	0.0004	0.016	0.004
Sr	0.003	0.06	0.02				

The tourmaline samples were analysed in combination with standard reference samples, to calibrate the equipment and ensure more accurate and precise results. The B isotope results of these standard samples are presented in Appendix B Table 2.

The measured B ratios were corrected for Initial Mass Function (IMF) and converted to $\delta^{11}B$ values, using the international boron isotope standard, NIST SRM 951 (Catanzaro, 1970; Leeman & Tonarini, 2001). The formula for the calculation of $\delta^{11}B$ is presented in chapter 4.2. The IMF value was averaged from the standard samples presented in Appendix B Table 2, for schorl-dravite tourmalines IMF is 0.9762.

8. Results

8.1. Fieldwork mapping of the Lindvikskollen pegmatite

The objective of the fieldwork was to map the Lindvikskollen pegmatite about 2.5 km W of Kragerø and its host rocks in detail to create a geological high-resolution map (Figure 8-1) and cross-section of a part of the pegmatite (Figure 8-2).

8.1.1. The Lindvikskollen pegmatite

The Lindvikskollen pegmatite forms an irregular body which is about 500 m long in E-W direction and up to 200 m wide. The pegmatite intruded a massive metagabbro, which forms the Storkollen-Lindvikskollen hill. The metagabbro is albitized to albitite at the W/NW contact of the pegmatite.

The pegmatite's major minerals are K-feldspar, plagioclase (oligoclase), quartz, and biotite. Accessory minerals identified during fieldwork comprise muscovite, albite, calcite, magnetite, black tourmaline, allanite-(Ce) and fergusonite-(Y). In addition, about 20 other accessory minerals have been described from the Lindvikskollen pegmatite, listed in Table 8-1.

The internal zoning of the pegmatite is defined by three mineralogical zones – wall, intermediate and core: (1) The **wall zone** is the outermost part of the pegmatite, characterized by megacrystic, relative equigranular pegmatitic granite (Figure 8-3A, B). In this zone multiple core and intermediate zones occur. During fieldwork three cores were mapped (Figure 8-1). (2) The **intermediate zones** (blocky zones; Figure 8-3A) surround the core zones**,** they consist predominantly of euhedral to sub-euhedral K-feldspar megacrysts, 0.2 to 2 m in size, beside quartz and minor muscovite and tourmaline (Figure 8-3C). Occasionally up to 2 m large biotite plates are found in the intermediate zone or in the wall zone close to the intermediate zone (Figure 8-3A). Around the core zone in the eastern part of the mine, the intermediate zone hosts up to 30 cm large crystals of allanite-(Ce) and fergusonite (Figure 8-3E). Both minerals are mineralogical indicators for NYF-type pegmatites. (3) The **core zones** consist predominantly of massive quartz, where up to 20 cm large tourmalines occur sparsely in the quartz core (Figure 8-3D).

Table 8-1 Minerals identified in the Lindvikskollen pegmatite. Modified from Mindat (2021). TL – type locality. *Simplified formula

Mineral name	**Formula**
Aeschynite-(Y)	$(Y,Ln,Ca,Th)(Ti,Nb)_2(O,OH)_6$
Albite	$Na(AlSi_3O_8)$
Allanite-(Ce)	$CaCe(Al_2Fe^{2+})[Si_2O_7][SiO_4]O(OH)$
Anatase	TiO_2
'Apatite'	$Ca_5(PO_4)_3(Cl/F/OH)$
Bastnäsite-(Ce)	$Ce(CO_3)F$
'Biotite'	$K(Mg,Fe)_3AlSi_3O_{10}(OH)_2$*
Calcite	$Ca(CO_3)$
Caysichite-(Y)	$(Ca,Yb,Er)_4Y_4(Si_8O_{20})(CO_3)_6(OH) \cdot 7H_2O$
Chernovite-(Y)	$Y(AsO_4)$
Euxenite-(Y)	$(Y,Ca,Ce,U,Th)(Nb,Ta,Ti)_2O_6$
'Fergusonite'	$(Ce,Nd,Y)NbO_4$
Fluorapatite	$Ca_5(PO_4)_3F$
'Gadolinite'	$(Ce,La,Nd,Y)_2Fe^{2+}Be_2Si_2O_{10}$
Hellandite-(Y) (TL)	$(Ca,REE)_4Y_2Al□_2(B_4Si_4O_{22})\ (OH)_2$
Hingganite-(Y)	$(Y,REE,Ca)_2(□,Fe^{2+})Be_2[SiO_4]_2(OH)_2$
Ilmenite	$Fe^{2+}TiO_3$
Kainosite-(Y)	$Ca_2(Y,Ce)_2(Si_4O_{12})(CO_3) \cdot H_2O$
Magnetite	$Fe^{2+}Fe^{3+}{}_2O_4$
Microcline	$K(AlSi_3O_8)$
Monazite-(Ce)	$Ce(PO_4)$
Muscovite	$KAl_2(AlSi_3O_{10})(OH)_2$
Oligoclase	$(Na,Ca)[Al(Si,Al)Si_2O_8]$
Phenakite	Be_2SiO_4
Pyrite	FeS_2
Quartz	SiO_2
Rutile	TiO_2
Schorl	$Na(Fe^{2+}{}_3)Al_6(Si_6O_{18})(BO_3)_3(OH)_3(OH)$
Tengerite-(Y)?	$Y_2(CO_3)_3 \cdot 2\text{-}3H_2O$
Thorite	$Th(SiO_4)$
Titanite	$CaTi(SiO_4)O$
Xenotime-(Y)	$Y(PO_4)$
Zircon	$Zr(SiO_4)$

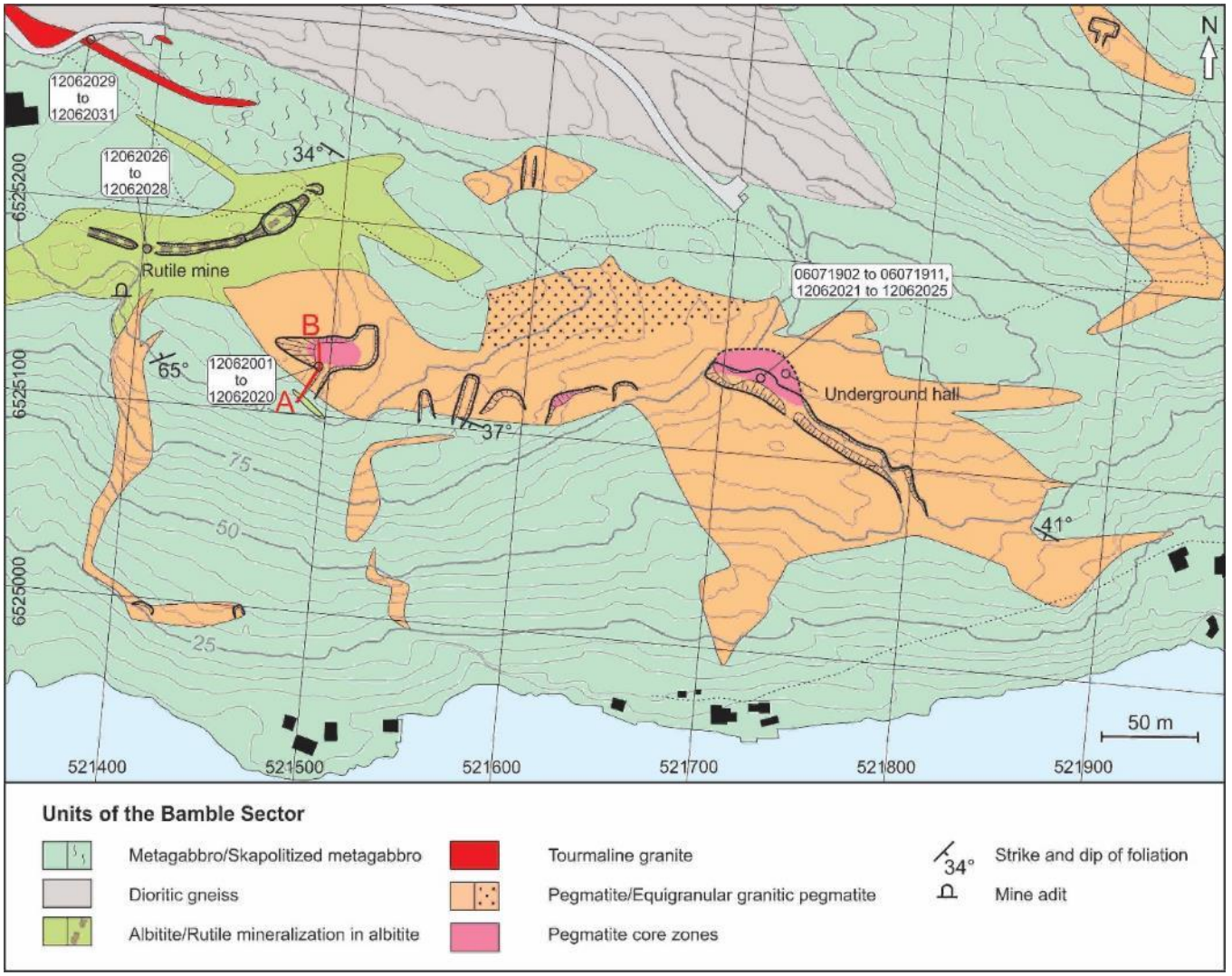

Figure 8-1 - Geological Map of Lindvikskollen pegmatite and surroundings with sample locations (white boxes with sample numbers). Location of the geological cross-section of Figure 8-2 is represented by the red lines and letters (A -B).

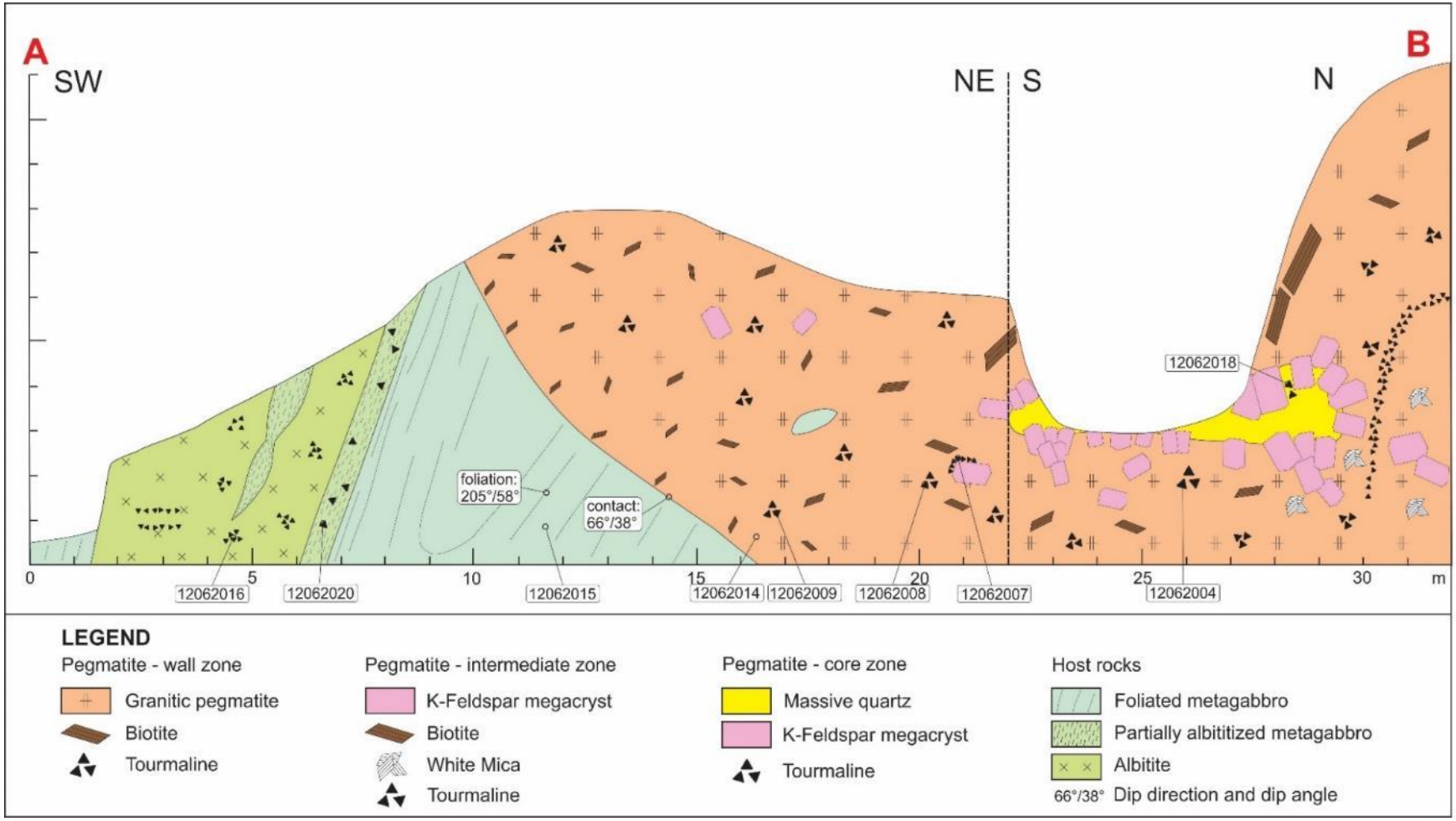

Figure 8-2 - Geological cross-sections through the SW part of the Lindvikskollen pegmatite with sample locations.

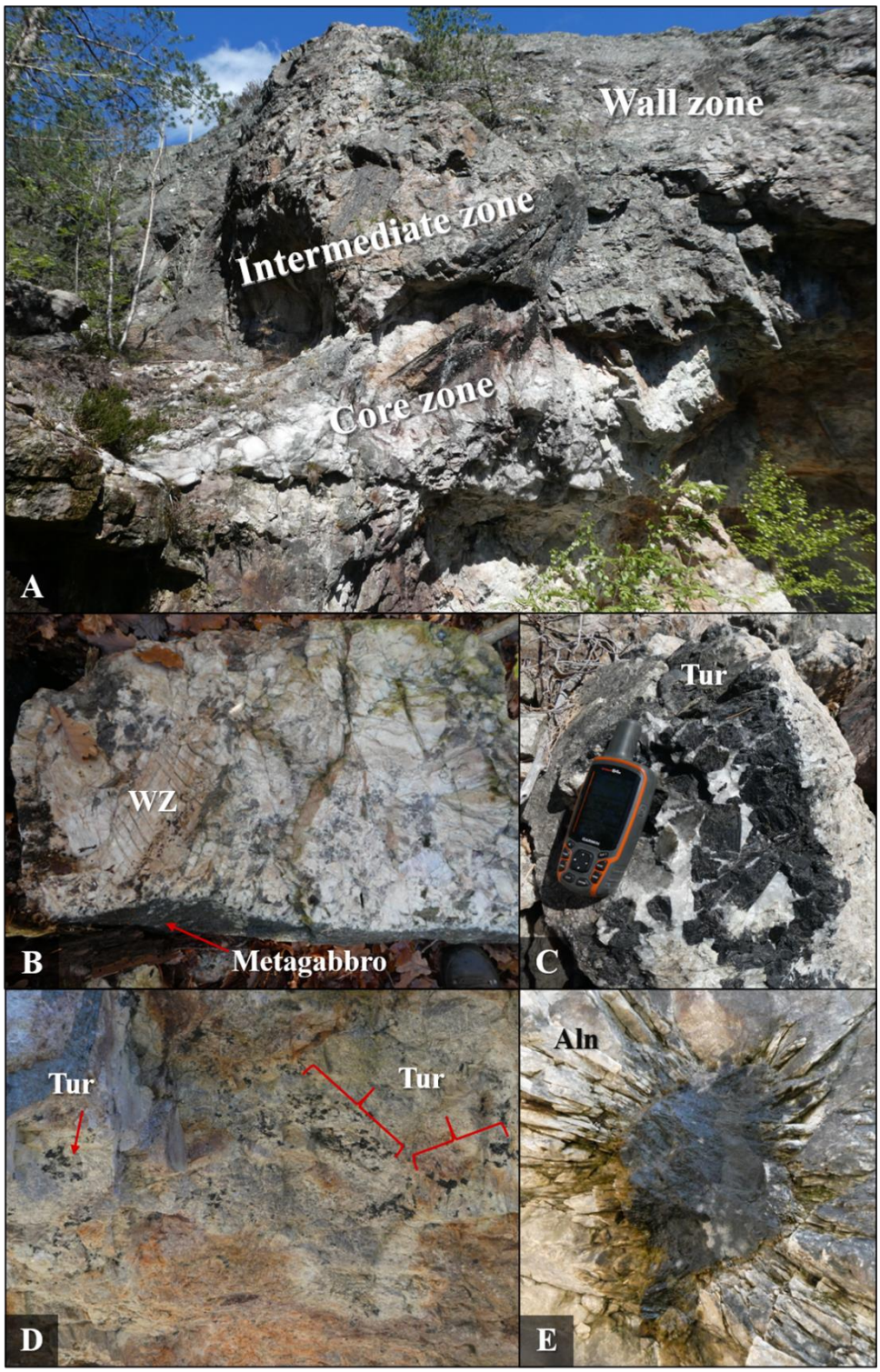

Figure 8-3 - Field photographs of the Lindvikskollen pegmatite. **A:** Wall zone, intermediate zone and core zone of the pegmatite exposed in the western open pit. Large biotite plates can be seen (ca. 2 m of length). **B:** Loose block showing metagabbro-pegmatite contact. No obvious border zone is developed, large feldspar crystals grew immediately from the contact plane forming the wall zone (WZ). **C:** Large tourmaline (Tur) crystals exposed near the eastern open pit. **D:** Tourmaline clusters in the intermediate zone close to the quartz core. **E:** Allanite-(Ce) megacryst (ca. 40 cm) of the intermediate zone exposed in the wall of the eastern mine.

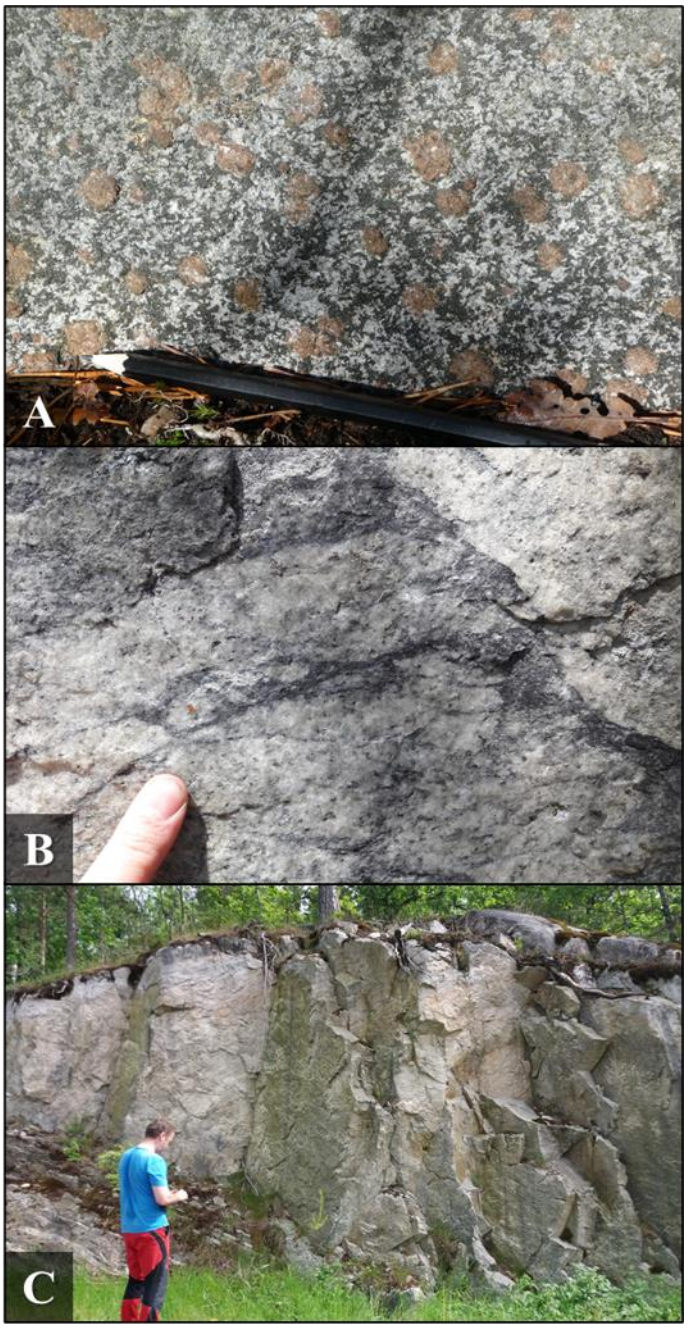

Figure 8-4 - Lithologies associated to the Lindvikskollen pegmatite. **A:** Host rock metagabbro with garnets. **B:** Host rock albitite with fine-grained tourmaline. **C:** Tourmaline granite dyke exposed at the road cut near Lindvikskollen Street nr. 26.

8.1.2. Metagabbro

The metagabbro is fine- to medium-grained with a gneissic to schistose structure (Figure 8-4A), and mainly composed of amphibole and andesine, in addition to biotite, garnet, epidote, chlorite, calcite and apatite. Accessory minerals include quartz, rutile, scapolite, prehnite, sphene, serpentine and zircon. Tourmaline occurs near the contact with the pegmatite (< 10 m).

8.1.3. Albitite

Metasomatic alteration of the metagabbro produced albitite, evident by the gradual contact between these rocks. The albitite is fine- to medium-grained, composed mainly of albite (Figure 8-4B). In less quantities, quartz and microcline can occur. The accessory minerals of the albitite consist of biotite, chlorite, epidote, rutile, titanite, hornblende, tourmaline, sphene and zircon. The tourmaline in the albitite occurs banded as schlieren and in patches, only near the contact with the pegmatite (< 10 m). This rock exhibits a metamorphic texture, locally displaying banding and strong foliation marked by its

mafic minerals. Pegmatite veins, consisting mostly of plagioclase with some rutile or amphibole, intrude the albitite. These veins are up to 20 cm wide.

8.1.4. Tourmaline-bearing granite dyke

A granite with tourmaline as minor mineral is exposed in a 4 m wide and south-dipping (176; 48S) dyke in a road cut c. 212 m NW of the Lindvikskollen pegmatite (Figure 8-4C). The dyke sits between the metagabbro and monzonitic gneiss. The latter has a strong foliation that has been affected by folding.

8.2. Bulk chemistry composition of the Lindvikskollen area rocks

The bulk chemistry composition of several Lindvikskollen area rocks were determined by whole-rock analyses. In the Lindvikskollen W mine three lithologies were sampled: wall zone of the pegmatite (12062014), metagabbro (12062015) and tourmaline-bearing albitite (12062016). In the rutile mine tailings two albitites were sampled: one rutile-rich albitite (12062026) and one rutile-poor albitite (12062027). In addition, further away from the sample location of the pegmatite (~ 212 m) the tourmaline-bearing granite (12062029) and the monzonitic gneiss (12062031) were sampled. Table 8-2 contains the geochemical data of the analysed rocks, and Figure 8-1 shows the sampling locations.

Samples of magmatic and meta-magmatic rocks were plotted in the total alkali vs SiO_2 diagram (TAS diagram; Figure 8-5). The wall zone of the Lindvikskollen pegmatite and the tourmaline-bearing granite plot in the granite field, with the granitic dyke having higher alkali composition than the pegmatite. The monzonitic gneiss plots in the monzonite field, close to the monzo-diorite border. The metagabbro plots in the foid-gabbro field, having the lowest SiO_2 and alkali content.

The A/CNK vs A/NK diagram (molar ratios $Al_2O_3/(CaO+Na_2O+K_2O)$ vs $Al_2O_3/(Na_2O+K_2O)$) shows that the pegmatite wall zone sample has an intermediate composition between the metaluminous and peraluminous fields. The tourmaline-bearing granite is classified as peraluminous, whereas the monzonitic gneiss is metaluminous (Figure 8-6).

Table 8-2 - Whole-rock compositions of the Lindvikskollen area selected rock samples. Major oxides (%) and major elements (%) were analysed by FUS-XRF and FUS-Na_2O_2 (see chapter 7.3.1). Limits of detection are presented in Table 7-2. Tour: Tourmaline. LOI: Loss on ignition.

Sample		**Pegmatite wall zone**	**Metagabbro**	**Tour-bearing albitite**	**Albitite (Rutile-rich)**	**Albitite (Rutile-poor)**	**Monzonitic gneiss**	**Tour-bearing granite**
Nr.		**12062014**	**12062015**	**12062016**	**12062026**	**12062027**	**12062029**	**12062031**
SiO_2	%	78.14	42.33	59.3	64.17	61.72	55.34	75.2
Al_2O_3	%	12.46	18.09	22.67	18.69	21.02	14.54	14.09
Fe_2O_3 (T)	%	1.51	8.84	1.58	0.56	1.11	5.05	1.31
MgO	%	0.4	7.89	2.29	0.16	0.8	10.11	0.12
CaO	%	1.66	7.77	2.28	0.7	1.66	4.87	0.56
Na_2O	%	5.35	3.66	8.55	10.13	9.76	6.02	4.61
K_2O	%	0.58	1.16	1.12	0.78	0.36	1.74	4.49
TiO_2	%	0.12	0.62	0.84	4.85	3.28	1.02	0.02
P_2O_5	%	0.01	0.06	0.04	0.01	0.24	0.25	0.02
MnO	%	0.029	0.061	0.013	0.005	0.009	0.013	0.03
LOI	%	0.23	10.05	1.52	0.18	0.48	1.85	0.25
Total	%	100.5	100.6	100.2	100.3	100.5	100.8	100.7
F	%	< 0.01	< 0.01	0.01	< 0.01	< 0.01	0.08	< 0.01
Al	%	6.74	10.7	12	9.82	11.2	7.89	7.63
As	ppm	6	< 5	< 5	< 5	< 5	18	< 5
B	ppm	20	230	2210	40	2380	90	750
Ba	ppm	30	66	82	23	49	18	10
Be	ppm	8	< 3	< 3	5	< 3	22	11
Bi	ppm	< 2	< 2	< 2	< 2	< 2	< 2	< 2
Ca	%	1.23	6.28	1.67	0.5	1.21	3.46	0.39
Cd	ppm	< 2	< 2	< 2	< 2	< 2	< 2	< 2
Ce	ppm	3.1	6.5	12.5	0.9	8.2	25	17.1

Co	ppm	4.8	44.6	4.9	1	3.4	10.8	0.6
Cr	ppm	90	130	120	150	90	110	70
Cs	ppm	2.3	3.6	1.5	0.6	0.4	4.5	2.3
Cu	ppm	12	12	6	67	8	3	10
Dy	ppm	1.6	1.9	1.4	< 0.3	1.8	4.6	4.2
Er	ppm	1	0.8	0.9	< 0.1	0.8	2.9	2.5
Eu	ppm	0.5	0.8	0.3	0.1	0.4	1.3	< 0.1
Fe	%	1.07	6.66	1.09	0.41	0.75	3.52	0.91
Ga	ppm	17.3	16.1	20.9	26.2	23.3	19.1	21.2
Gd	ppm	0.9	2	1.8	0.2	2.3	4.9	3.2
Ge	ppm	1.8	1.2	1.8	2.1	1.8	2.6	4.7
Ho	ppm	0.4	0.3	0.4	< 0.2	0.4	1	0.7
Hf	ppm	< 10	< 10	< 10	10	10	10	< 10
In	ppm	< 0.2	< 0.2	< 0.2	< 0.2	< 0.2	< 0.2	< 0.2
K	%	0.5	1.1	1	0.7	0.3	1.5	3.8
La	ppm	2.3	2.7	7.3	1	3.6	10.2	7.9
Li	ppm	16	32	22	7	6	29	7
Mg	%	0.19	5.3	1.26	0.02	0.39	6.08	0.04
Mn	ppm	251	436	104	51	69	111	221
Mo	ppm	< 1	< 1	< 1	< 1	< 1	< 1	< 1
Nb	ppm	7.5	3.6	4.4	10.4	6.8	35.6	23.5
Nd	ppm	1.7	4.8	7.7	0.5	5.4	21	8.9
Ni	ppm	20	160	90	50	50	90	20
Pb	ppm	8.2	4.4	14.1	5	3.2	2	8.1
Pr	ppm	0.4	1.1	1.6	0.2	1.5	3.4	2.4
Rb	ppm	39.7	39.5	48.2	5.5	6.2	70.7	228
S	%	< 0.01	0.04	0.02	< 0.01	0.02	< 0.01	< 0.01

Sb	ppm	< 2	< 2	< 2	< 2	< 2	3	< 2
Se	ppm	< 8	< 8	8	< 8	17	< 8	< 8
Si	%	> 30.0	22.3	28.3	> 30.0	29.2	26.1	> 30.0
Sm	ppm	0.7	1.5	1.6	0.1	1.6	5.7	3.3
Sn	ppm	3.2	1.8	2.7	7.4	3.6	6.4	2.9
Sr	ppm	92	216	132	43	95	35	23
Ta	ppm	0.9	0.4	0.5	0.6	0.7	2.3	4.8
Tb	ppm	0.2	0.4	0.3	< 0.1	0.3	0.8	0.7
Te	ppm	9	6	9	14	< 6	7	< 6
Th	ppm	19	0.2	0.5	0.5	0.7	6.4	4.8
Ti	%	0.07	0.41	0.5	2.84	1.98	0.59	< 0.01
Tl	ppm	0.2	0.1	0.1	< 0.1	< 0.1	0.1	0.8
Tm	ppm	0.2	0.1	0.1	< 0.1	0.1	0.4	0.6
U	ppm	4.4	0.6	0.9	6.2	1.5	0.9	5.6
V	ppm	15	71	123	176	316	97	7
W	ppm	1.1	1	3.8	19.4	7.4	2.5	1.3
Y	ppm	10	9.2	8.7	0.8	9.5	27.9	25.5
Yb	ppm	1.8	1.3	0.9	0.3	0.5	3	4.5
Zn	ppm	< 30	< 30	< 30	< 30	< 30	< 30	< 30

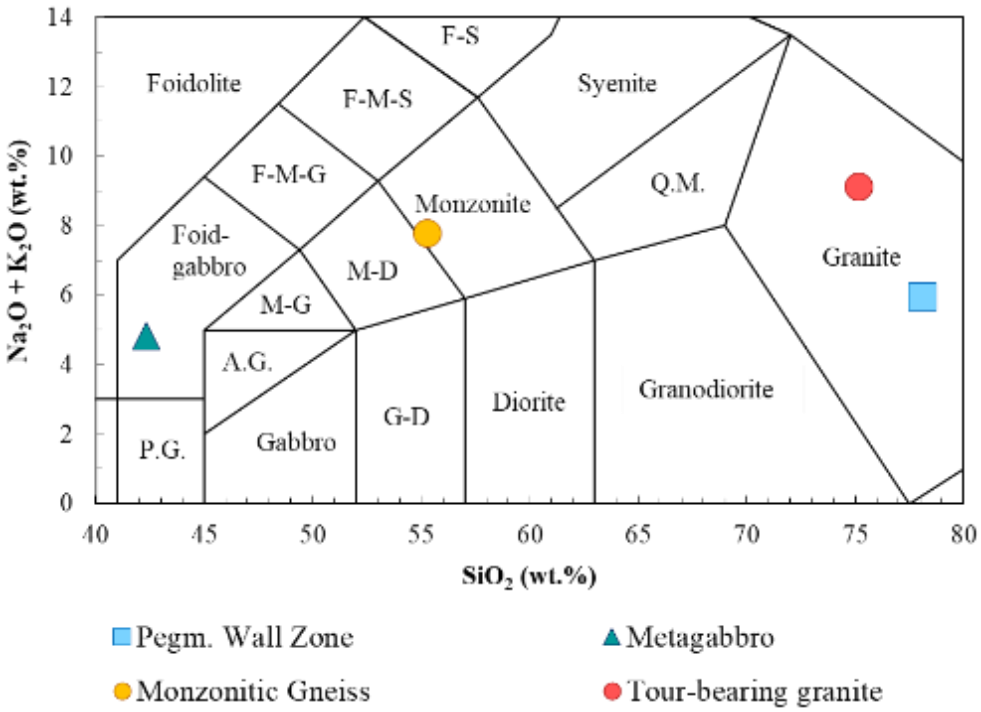

Figure 8-5 - SiO_2 vs Na_2O+K_2O (wt.%): TAS diagram (Le Maitre *et al.*, 2005), showing the classification of the Lindvikskollen area magmatic and meta-magmatic rocks based on their bulk rock composition. F-S: Foid-syenite; F-M-S: Foid-monzo-syenite; F-M-G: Foid-monzo-gabbro; Q.M.: Quartz monzonite; M-D: Monzo-diorite; M-G: Monzo-gabbro; G-D: Gabbroic-diorite; A.G.: Alkalic Gabbro; P.G.: Peridot Gabbro.

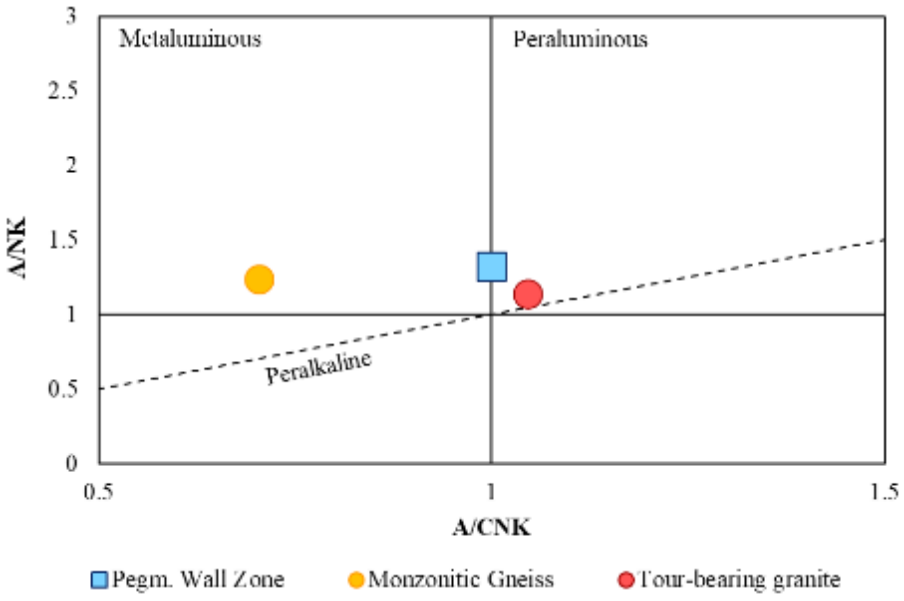

Figure 8-6 - A/CNK vs A/NK diagram (molar ratios of $Al_2O_3/(CaO+Na_2O+K_2O)$ vs $Al_2O_3/(Na_2O+K_2O)$). The Lindvikskollen pegmatite has an intermediate composition between metaluminous and peraluminous. The monzonitic gneiss plots in the metaluminous field. The tourmaline-bearing granite plots in the peraluminous field.

The bulk wall zone of the pegmatite and the tourmaline-bearing granite were plotted in the granite type classification diagrams adapted from Whalen *et al.* (1987) (Figure 8-7). The pegmatite sample plots in between the A-type granites and the I-, S-, M-type granites fields, while the tourmaline-bearing granite plots in the A-type granite field (Figure 8-7A). Both samples plot in the A2-type granite field in the Y/Nb vs Rb/Nb diagram (Figure 8-7B), which discerns A-type granites depending on their source. A1-type granites are formed by crystal fractionation or partial melting of sources similar to the ocean island basalts. A2-type granites are related to sources similar to the average continental crust (excluding metasediments) or arc-type sources, derived from partial melting.

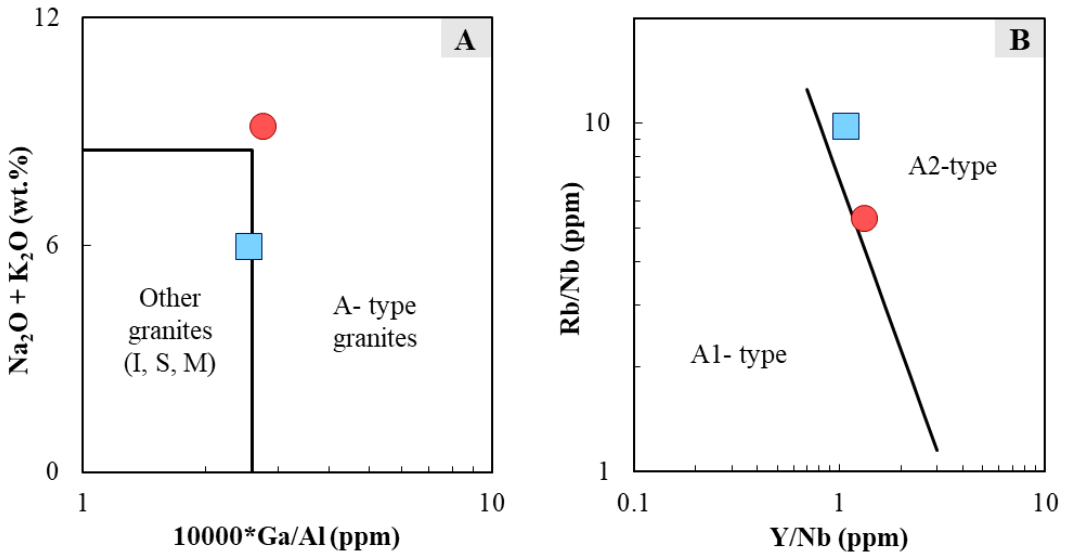

Figure 8-7 - **A:** 10000*Ga/Al (ppm) vs Na_2O+K_2O (wt.%) diagram (Whalen *et al.*, 1987), the tourmaline-bearing granite plots in the A-type field, while the pegmatite wall zone plots in the limit between both granitic fields. **B:** Y/Nb vs Rb/Nb (ppm) diagram (Eby, 1992). Both samples plot in the A-2 type field. A1-type granites are formed by crystal fractionation or partial melting of sources similar to the ocean island basalts. A2-type granites are related to sources similar to the average continental crust (excluding metasediments) or arc-type sources, derived from partial melting.

To determine the relationship between the pegmatite and its associated lithologies all bulk rock samples including the metasomatic albitites were normalized to the upper continental crust (UCC; Rudnick & Gao, 2003) and plotted in a spidergram (Figure 8-8) of selected incompatible elements. No sample is close to the average UCC composition. All samples of the Lindvikskollen area show in overall a relative similar distribution pattern characterized by depletion in Ba, K, La, Ce, Sr, and Nd relatively to the UCC composition. All analysed samples are rich in Ti, the albitites (rutile-rich and -poor) from the rutile mine have the highest ratio (> 516). The pegmatite wall zone is particularly enriched in Th in relation to the other samples.

Compared to the UCC composition the host rocks of the pegmatite, the metagabbro and albitites are depleted in most elements, except Ti, Li (in the metagabbro), Sn and W (both in the albitites). The rutile-poor albitite shows the lowest REE and Y content.

Relatively to the UCC, the monzonitic gneiss and the tourmaline-bearing granite have high concentrations of Ta, Nb, Y, Yb. The gneiss is also richer in Sm, Sn and W. Whereas, the tourmaline-bearing granite differentiates itself from the other rocks by having high Rb and the lowest concentration in Ti.

The tourmaline-bearing albitite and the rutile-poor albitite have the highest concentrations of B, with sample/UCC ratios between 130 and 140 (2210 and 2380 ppm, respectively). The other samples have ratios below 44 (750 ppm), the pegmatite wall zone having the lowest, 1.2 (20 ppm).

Sr is richer in the metagabbro, tourmaline-bearing albitite, rutile-rich albitite and pegmatite in comparison with the rutile-poor albitite, monzonitic gneiss and granite.

The REE concentrations of the samples were normalized to the chondrite composition (Anders & Grevesse, 1989) and plotted in a REE plot (Figure 8-9). The monzonitic gneiss is, in general, the richest sample in REE, while the albitite (rutile-rich) is the most depleted. Most of the REE of the rutile-rich albitite elements have concentrations below the limit of detection (LOD) (Table 7-2). The pegmatite wall zone is poorer in most REE (La up to Dy) than the metagabbro, but richer in some HREE (Ho up to Yb). Both rocks show a positive Eu anomaly. Whereas the tourmaline-bearing albitite and the rutile-poor albitite display a negative Eu anomaly. The metagabbro, the tourmaline-bearing albitite and the monzonitic gneiss have a higher concentration of LREE than HREE. The tourmaline-bearing granite has in overall a smooth REE pattern, except for a strong negative Eu anomaly. This rock Eu concentration is below the detection limit (< 0.1 ppm; Table 7-2).

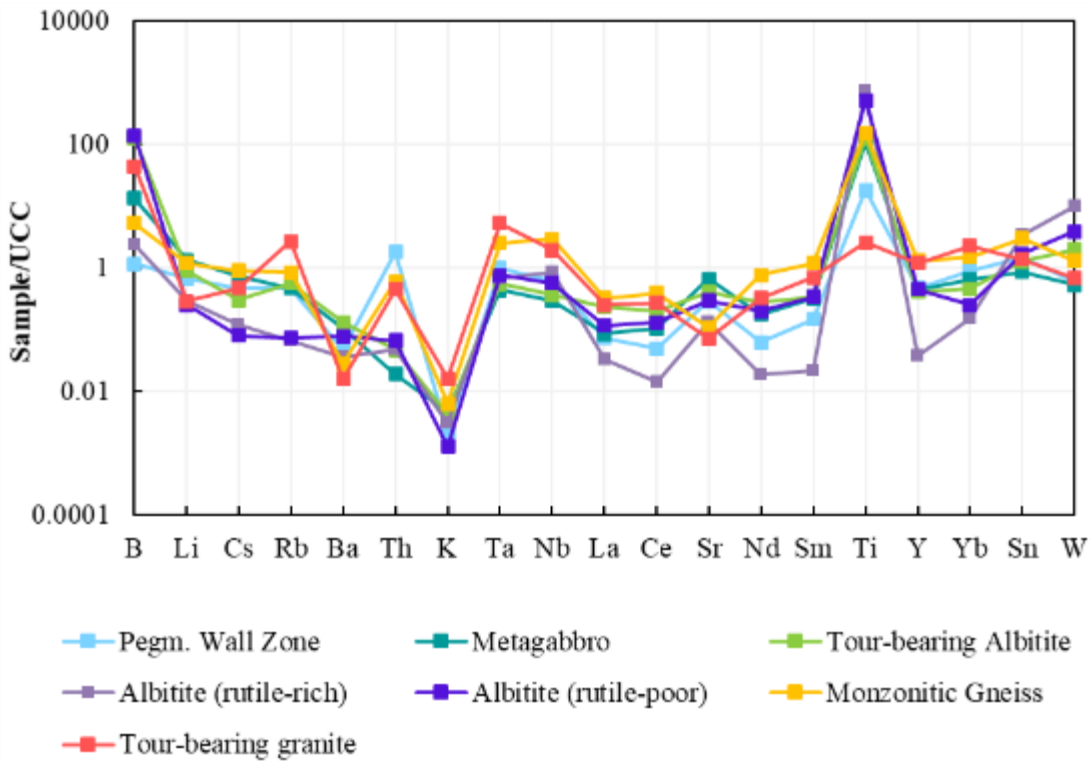

Figure 8-8 - Spidergram of incompatible elements from the Lindvikskollen area rocks normalized to the composition of the UCC (Rudnick & Gao, 2003). In overall, all samples have a similar element distribution. All samples are rich in Ti, and poor in Ba, K, La, Ce, and Nd relatively to the UCC.

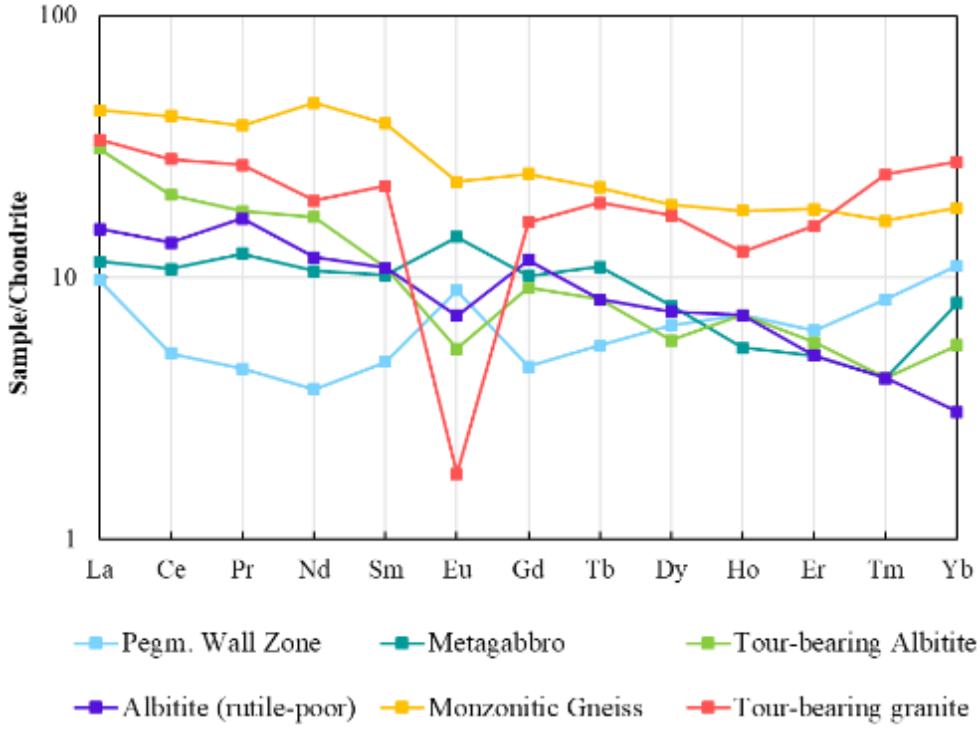

Figure 8-9 - Chondrite normalized REE diagram (Anders & Grevesse, 1989). Ratios of albitite (rutile-rich) are not plotted because several REE values are below the LOD.

8.3. Tourmaline composition

8.3.1. Variation of tourmaline chemistry among different pegmatites

The major and minor element composition of the studied tourmalines were determined by EPMA, and this data was used to calculate the atoms per formula unit (apfu). The trace element chemistry of the tourmalines was obtained by LA-ICP-MS. The analysed samples and their respective analytical method are presented in Table 7-1.

The contents of Li_2O, B_2O_3, and H_2O of the EPMA data were obtained using an Excel calculation spreadsheet. In this approach, B_2O_3 and H_2O were calculated assuming fixed B at 3 apfu and OH + F at 4 apfu. Li was calculated using the method of Burns *et al.* (1994). In some cases, however, the Li calculated values from EPMA data, are not in agreement with the LA-ICP-MS measured values of the same sample. That means that the applied calculations can be unreliable for some tourmalines. Another reason for the difference in results could be that the analyses were made in different places of the tourmaline crystal with large differences in the Li content. However, that seems unlikely because such large intra-crystal variations have not been reported from schorl and dravite tourmalines. Because of this discrepancy the Li concentrations presented in the text are the ones measured by LA-ICP-MS. The averaged results of the EPMA and LA-ICP-MS are presented in Table 8-3 and Table 8-4.

The investigated samples belong to the alkali-tourmaline group based on the dominant occupancy of the X-site (Figure 8-10). The data, however, shows a wide scatter across the alkali group field. The majority of the tourmalines classify as schorl, with Mg/(Mg+Fe) values between 0 and 0.49 (Figure 8-11). Within the schorl field the data occurs in a wide range. Schorls from the Spro and Tangen pegmatites are very Fe-rich, whereas all schorls from the Lindvikskollen pegmatite plot in a relative narrow field closer to dravite compositions. In fact, all Lindvikskollen pegmatite tourmaline compositions are almost indistinguishable in this plot. The sample from the tourmaline-bearing granitic dyke, has a higher Fe content than the pegmatitic tourmaline. The sample from the Dalane pegmatite plots close to the foitite field and, thus, has a rather distinctive composition compared to all other tourmalines.

Tourmalines from the Ramfoss and Havredal pegmatites and host rocks of the Spro and Lindvikskollen pegmatites - metagabbro and albitite - plot in the dravite field (Figure 8-11). These

tourmalines have Mg/(Mg+Fe) values between 0.54 and 0.85. The investigated dravites also show a wide spread of compositions.

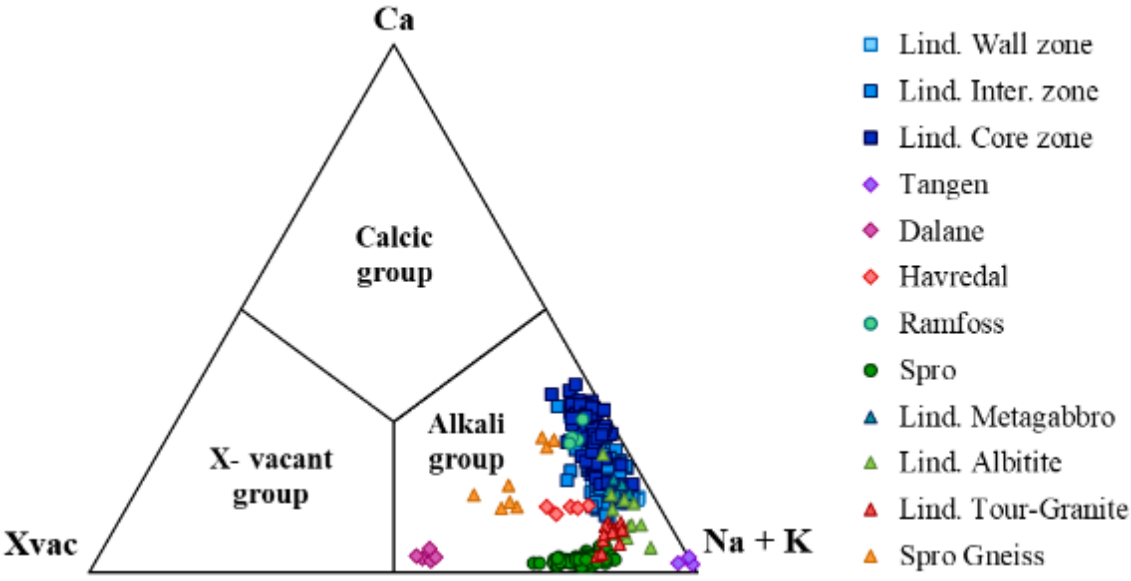

Figure 8-10 - Tourmaline classification according to Henry *et al.* (2011) using the occupancy of the X-site. Lind.: Lindvikskollen; Inter.: Intermediate; Tour-Granite: Tourmaline-bearing granite.

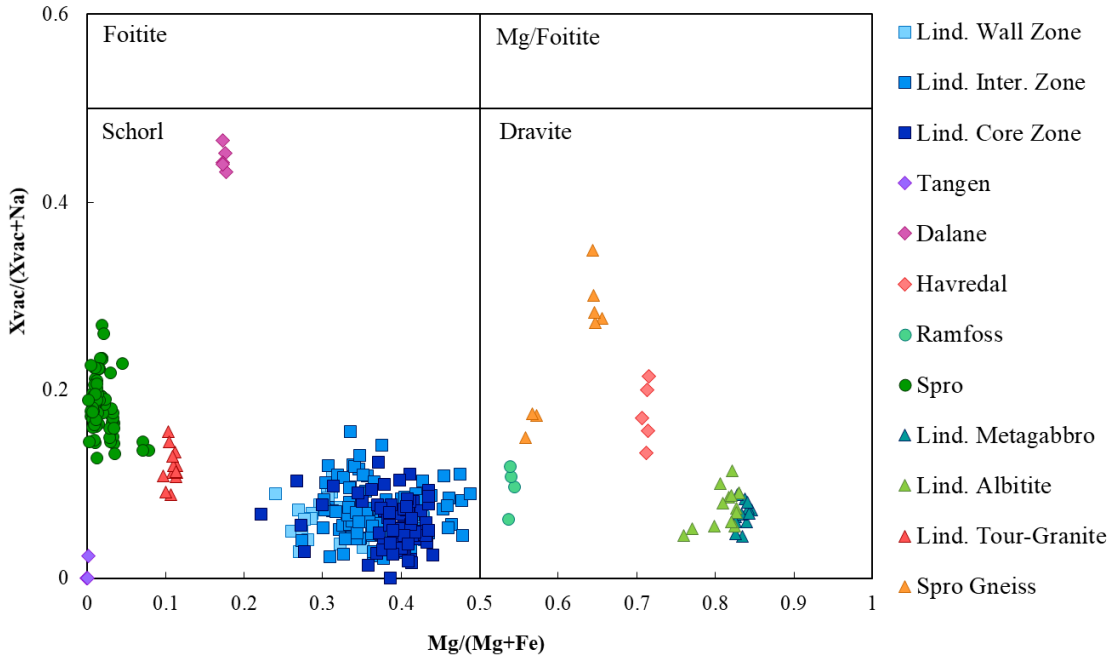

Figure 8-11 - Mg/(Mg+Fe) vs Xvac/(Xvac+Na) classification according to Henry *et al.* (2011). Xvac: X-site vacancy; Lind.: Lindvikskollen; Inter.: Intermediate; Tour-Granite: Tourmaline-bearing granite.

Table 8-3 - Average results of tourmaline EPMA data. Standard deviation in parentheses. LOD are presented in Table 7-3. Z.: zone; L.: Lindvikskollen; MG: metagabbro; Alb.: albitite; Tour-Gr.: tourmaline-bearing granite; Gn.: gneiss; n: number of analyses; X Al: Al apfu allocated to the X-site; Xvac: X site vacancy.

Samples	Lindvikskollen			Tangen	Dalane	Havredal	Ramfoss	Spro	Host Rocks			
	Wall Z.	Inter. Z.	Core Z.						L. MG	L. Alb.	L. Tour-Gr.	Spro Gn.
n	**26**	**97**	**74**	**3**	**5**	**4**	**4**	**81**	**12**	**14**	**13**	**8**
SiO_2	34.97 (0.37)	35.21 (0.30)	35.17 (0.29)	33.55 (0.18)	36.21 (0.20)	36.96 (0.35)	35.92 (0.15)	34.67 (0.31)	37.17 (0.14)	36.98 (0.24)	34.14 (0.21)	36.44 (0.4)
Al_2O_3	25.06 (0.61)	25.31 (1.16)	24.19 (0.59)	21.21 (0.29)	33.75 (0.19)	31.18 (0.29)	28.42 (0.11)	32.33 (0.55)	31.66 (0.27)	31.19 (0.61)	29.98 (0.66)	32.66 (1.31)
TiO_2	1.22 (0.21)	1.19 (0.36)	1.31 (0.14)	1.17 (0.03)	0.08 (0.03)	0.41 (0.04)	1.41 (0.07)	0.14 (0.11)	0.60 (0.04)	0.88 (0.31)	0.39 (0.03)	0.42 (0.15)
FeO	17.27 (1.22)	16.24 (1.23)	16.28 (0.87)	25.11 (0.28)	13.27 (0.19)	6.15 (0.11)	10.22 (0.15)	16.18 (0.59)	3.32 (0.19)	3.79 (0.49)	17.82 (0.67)	7.20 (1.34)
MgO	4.75 (0.99)	5.36 (0.79)	5.91 (0.72)	0.01 (0.01)	1.57 (0.03)	8.55 (0.10)	6.73 (0.14)	0.17 (0.15)	9.44 (0.1)	9.14 (0.30)	1.21 (0.09)	6.43 (0.18)
MnO	0.16 (0.03)	0.18 (0.06)	0.19 (0.04)	3.10 (0.05)	0.14 (0.02)	0.01 (0.02)	0.02 (0.01)	0.31 (0.09)	0.00 (0)	0.01 (0.01)	0.95 (0.18)	0.02 (0.02)
Na_2O	2.21 (0.18)	2.15 (0.11)	1.98 (0.12)	2.66 (0.03)	1.66 (0.04)	2.26 (0.08)	2.02 (0.03)	2.37 (0.08)	2.50 (0.05)	2.62 (0.13)	2.40 (0.04)	1.91 (0.08)
B_2O_3	10.04	10.11	10.06	9.54	10.51	10.71	10.46	10.19	10.81	10.75	10.10	10.67
CaO	1.01 (0.36)	1.15 (0.24)	1.49 (0.26)	0.11 (0.03)	0.18 (0.05)	0.71 (0.04)	1.46 (0.11)	0.13 (0.04)	0.91 (0.07)	0.61 (0.26)	0.40 (0.11)	1.03 (0.32)
Li_2O	0.23	0.24	0.29	0.84	0.30	0.20	0.52	0.22	0.45	0.52	0.06	0.30
H_2O	3.38	3.36	3.36	3.25	3.58	3.68	3.58	3.08	3.61	3.62	3.47	3.60
K_2O	0.10 (0.02)	0.08 (0.002)	0.08 (0.01)	0.13 (0)	0.04 (0.01)	0.07 (0.01)	0.09 (0.01)	0.08 (0.01)	0.04 (0.01)	0.03 (0.01)	0.08 (0.03)	0.06 (0.01)
F	0.18 (0.1)	0.27 (0.1)	0.24 (0.09)	0.09 (0.02)	0.09 (0.1)	0.04 (0.04)	0.05 (0.01)	0.93 (0.16)	0.26 (0.04)	0.18 (0.07)	0.02 (0.08)	0.17 (0.06)
Total	100.49	100.75	100.43	100.75	101.35	100.92	100.88	100.41	100.67	100.23	101.01	100.84
Formula proportions based on 31 oxygen atoms (apfu)												
Si	6.06	6.05	6.08	6.11	5.99	6.00	5.97	5.91	5.98	5.98	5.88	5.93
Al	5.11	5.13	4.92	4.55	6.57	5.96	5.57	6.50	6.00	5.95	6.08	6.26
Ti	0.16	0.15	0.17	0.16	0.01	0.05	0.18	0.02	0.07	0.11	0.05	0.05
Fe^{2+}	2.50	2.34	2.35	3.83	1.84	0.83	1.42	2.31	0.45	0.51	2.57	0.98
Mg	1.22	1.37	1.52	0.00	0.39	2.07	1.67	0.04	2.26	2.20	0.31	1.56
Mn	0.02	0.03	0.03	0.48	0.02	0.00	0.00	0.04	0.00	0.00	0.14	0.00
Na	0.74	0.71	0.66	0.94	0.53	0.71	0.65	0.78	0.78	0.82	0.80	0.60
B	3.00	3.00	3.00	3.00	3.00	3.00	3.00	3.00	3.00	3.00	3.00	3.00
Ca	0.19	0.21	0.28	0.02	0.03	0.12	0.26	0.02	0.16	0.10	0.07	0.18
Li	0.16	0.17	0.20	0.62	0.20	0.13	0.35	0.15	0.29	0.34	0.04	0.19
OH	3.90	3.85	3.87	3.95	3.95	3.98	3.97	3.50	3.87	3.91	3.99	3.91
K	0.02	0.02	0.02	0.03	0.01	0.01	0.02	0.02	0.01	0.01	0.02	0.01
F	0.10	0.15	0.13	0.05	0.05	0.02	0.03	0.50	0.13	0.09	0.01	0.09
X Al	-0.62	-0.62	-0.77	-1.12	0.57	0.03	-0.23	0.43	0.07	0.07	0.03	0.27
X vac	0.05	0.06	0.04	0.01	0.43	0.15	0.07	0.18	0.06	0.07	0.11	0.20

Table 8-4 - Average results of tourmaline LA-ICP-MS data. LOD are presented in Table 7-5.

	Lindvikskollen								Tangen		Dalane		Havredal	
	Wall. Z.		Inter. Z.		Core Z. 1		Core Z. 2							
	n = 9	SD	n = 8	SD	n = 8	SD	n = 8	SD	n = 8	SD	n = 8	SD	n = 8	SD
Li	23.06	2.08	33.77	41.39	14.63	2.32	12.62	0.34	50.04	54.94	55.70	4.19	1.50	0.22
Be	3.40	0.41	3.13	12.84	3.20	1.60	1.09	0.06	4.44	0.68	1.53	0.10	0.41	0.09
Na	17154.31	272	16539.31	1172	15157.72	296	15263.07	124	16695.42	9424	15038.53	364	18266.95	361
Mg	20852.94	2085	28828.78	1506	33839.91	625	35026.97	391	10977.90	18450	8854.02	343	44764.30	1336
Al	143011.6	3482	134141.5	7261	141292.2	3819	142804.2	2455	139909.9	15461	197050.4	6003	160572.2	4854
Si	164351.7	0	164683.6	0	164636.8	0	164365.7	0	175149.5	0	169250.5	0	172756.2	0
P	24.45	8.53	32.46	39.03	41.38	54.04	21.01	1.00	31.75	2.87	21.86	2.87	37.85	4.21
K	809.34	35.91	741.32	124.50	696.95	26.38	534.76	8.22	2618.08	3539.20	450.48	2.74	551.28	37.27
Ca	7955.78	481	8663.62	383	12784.18	686	12424.44	355	1398.64	463	3248.23	270	4169.82	361
Sc	374.10	158.74	263.19	56.46	110.88	21.02	70.61	4.10	12.93	2.48	61.42	5.30	41.62	3.18
Ti	9547.69	356	7596.97	2265	8904.12	407	7039.46	177	7129.82	2813	1232.81	15	2063.19	47
V	67.90	7.07	153.54	57.61	287.78	12.19	209.86	4.89	8.33	1.10	5.55	0.50	199.11	6.44
Cr	10.11	0.62	23.50	4.04	13.81	2.26	11.89	0.79	19.49	2.03	11.07	1.82	78.05	13.25
Mn	1291.65	41	1807.81	260	1284.21	88	1273.19	16	13811.01	3451	1489.04	24	28.25	3
Co	32.35	2.22	33.93	4.96	35.09	0.42	35.42	0.62	3.78	4.93	0.70	0.05	11.33	0.29
Ni	1.17	0.27	16.01	5.04	42.96	6.94	11.60	1.19	5.13	0.33	1.34	0.78	41.28	4.21
Cu	4.19	0.29	4.26	15.18	3.85	0.41	3.66	0.05	10.18	10.66	3.74	0.08	4.55	0.15
Zn	105.24	6.79	149.65	20.09	114.99	6.77	109.82	1.34	1586.46	306.71	826.34	21.97	8.05	0.48
Ga	133.87	5.32	115.55	6.22	88.19	2.49	69.58	0.40	292.52	39.52	129.61	1.97	68.76	2.09
Rb	0.09	0.03	0.64	6.12	0.23	0.19	0.03	0.002	14.71	33.47	0.04	0.01	0.00	0.01
Sr	9.43	0.70	23.00	6.24	54.06	2.19	37.16	0.46	11.11	5.97	1.52	0.08	19.00	2.73
Y	9.88	27.52	2.23	495.04	102.85	254.48	0.20	0.25	2.81	4.48	0.05	0.01	0.16	0.04
Zr	2.24	1.90	1.96	1.69	58.83	77.43	0.49	0.04	1.12	0.14	0.27	0.19	0.94	0.16
Nb	5.38	4.58	2.59	221.97	3.74	5.20	0.68	0.03	6.45	12.50	2.38	0.07	0.14	0.01
Mo	0.08	0.02	0.14	0.01	0.09	0.02	0.08	0.01	0.14	0.05	0.06	0.01	0.13	0.01
Sn	74.29	21.73	43.62	4.50	32.34	3.80	13.58	0.33	153.32	50.97	12.18	0.35	4.72	0.29
Sb	0.06	0.03	0.09	0.71	0.15	0.11	0.00	0.003	0.32	0.23	0.15	0.13	0.00	0.003
Cs	0.01	0.004	0.30	5.11	0.09	0.08	0.02	0.001	0.29	0.31	0.04	0.03	0.00	0.003
Ba	0.09	0.05	1.11	3.43	0.56	0.20	0.16	0.02	7.74	12.58	0.00	0.02	0.72	0.20
La	9.97	1.74	2.86	3.95	4.28	2.12	2.25	0.06	2.58	0.84	3.33	0.05	1.71	0.32
Ce	17.41	3.07	4.49	7.22	8.28	8.40	3.12	0.14	2.38	0.85	6.29	0.22	3.57	0.71
Pr	1.93	0.35	0.47	1.18	1.27	2.17	0.24	0.01	0.10	0.06	0.63	0.01	0.33	0.05
Nd	6.28	1.29	1.42	8.18	5.15	10.20	0.63	0.02	0.22	0.27	1.69	0.03	0.98	0.14
Sm	1.24	0.69	0.32	16.54	3.44	8.20	0.09	0.01	0.06	0.06	0.45	0.01	0.15	0.02
Eu	0.19	0.06	0.16	2.33	0.65	0.99	0.29	0.01	0.02	0.03	0.01	0.001	0.05	0.01
Lu	0.39	0.87	0.13	14.62	2.13	4.97	0.04	0.01	0.64	0.94	0.00	0	0.004	0
Ta	1.81	0.91	0.36	9.19	0.42	0.11	0.07	0.04	1.19	0.57	0.26	0.03	0.06	0.09
W	0.05	0.01	0.03	1.58	0.35	0.28	0.00	0.002	0.31	0.64	0.09	0.05	0.00	0.01
Pb	3.18	1.84	2.85	1.84	4.19	2.56	2.17	0.04	17.41	8.88	4.78	0.10	0.16	0.02
Th	0.18	0.41	0.02	1.93	8.20	8.42	0.0002	0	0.03	0.03	0.003	0.002	0.01	0.001
U	17.89	12.47	0.56	267.69	37.02	47.45	0.11	0.04	3.64	8.28	0.004	0.002	0.00	0.001

	Ramfoss		Spro		Host Rocks							
					L. Metagabbro		L. Albitite		L. Tour-Granite		Spro Gneiss	
	n = 8	SD	n = 23	SD	n = 8	SD	n = 8	SD	n = 4	SD	n = 8	SD
Li	5.78	0.29	416.17	284.74	3.41	0.97	5.80	1.40	130.01	19.14	16.09	2.28
Be	0.86	0.10	8.72	1.51	0.36	0.03	2.41	3.54	7.42	1.08	1.26	0.30
Na	14679.67	459	17492.32	701.17	19712.99	451	19661.15	976	15596.08	541	14494.55	863
Mg	41253.78	1051	1744.07	2557.61	53213.06	1201	58724.83	2336	8355.74	1967	33398.04	1791
Al	167221.6	2337	189715.3	9258.71	166805.8	3619	174721.1	5603	168671.7	7278	177335.5	10618
Si	165800.7	0	162045.7	812.30	173767.8	0	172854.4	0	159565.1	0	162035.5	13
P	26.95	2.74	21.52	2.07	31.91	3.66	34.74	7.58	52.10	30.03	46.32	15.24
K	648.09	25.49	921.52	666.16	243.40	42.62	159.83	53.03	1495.78	684.86	343.64	28.48
Ca	12879.46	2506	1503.09	1663.34	6168.19	741	4408.88	1659	5757.07	475	7067.07	2820
Sc	67.34	3.19	1.29	0.89	38.77	1.33	26.60	2.05	177.83	12.21	30.22	21.30
Ti	7212.96	209	1179.74	1146.58	3605.65	244	4178.61	1186	2362.89	151	3603.02	3290
V	135.20	10.93	13.14	21.16	1091.94	34.08	772.94	304.61	19.83	6.84	234.73	68.57
Cr	57.95	16.54	13.39	10.32	643.13	130.62	259.72	139.93	6.70	0.16	149.86	28.93
Mn	158.40	11	2490.03	541.50	39.39	4	44.31	5.27	5829.22	434	427.22	309
Co	31.21	0.51	34.24	13.12	14.89	0.41	21.17	3.96	3.61	1.93	23.27	3.34
Ni	51.42	2.99	13.48	20.13	315.99	11.61	336.04	27.01	4.54	3.36	161.23	184.77
Cu	4.21	0.82	4.71	1.38	4.47	0.27	4.57	0.56	19.92	4.75	118.49	288.46
Zn	14.52	0.49	824.82	244.14	10.79	1.60	11.41	1.49	343.05	21.38	180.32	11.01
Ga	57.07	1.59	91.63	16.72	46.56	0.61	47.09	1.32	83.68	6.12	32.80	2.52
Rb	0.10	0.03	5.78	11.62	0.00	0.02	0.16	0.01	7.96	5.86	3.16	2.19
Sr	64.55	41.05	16.90	10.86	38.58	5.08	66.39	18.85	2.98	1.28	224.72	145.00
Y	43.36	121.45	1.33	2.10	0.34	0.19	0.71	0.56	4.31	3.00	15.52	21.83
Zr	3.31	2.60	14.19	36.08	2.75	0.43	0.59	0.80	1.93	0.53	57.19	48.93
Nb	0.32	0.03	1.77	1.68	0.02	0.003	0.00	0.004	8.70	1.00	5.68	15.46
Mo	0.09	0.02	0.07	0.01	0.28	0.05	0.25	0.05	0.09	0.01	0.35	0.04
Sn	3.20	0.20	3.38	1.08	2.69	0.23	2.00	1.01	59.31	1.87	2.93	2.44
Sb	0.17	0.10	0.18	0.15	0.00	0.01	0.05	0.02	0.11	0.09	1.01	1.49
Cs	0.04	0.01	0.83	2.18	0.00	0.01	0.07	0.01	2.55	2.99	1.72	0.96
Ba	0.53	0.23	0.88	2.21	0.31	0.07	0.36	0.09	3.47	1.55	0.74	0.67
La	5.39	2.02	1.66	1.04	3.90	0.59	2.88	2.09	12.29	1.43	2.55	1.16
Ce	196.31	530.16	2.72	1.74	7.85	1.85	5.16	4.27	26.76	3.68	4.88	3.19
Pr	21.35	57.88	0.27	0.17	0.78	0.16	0.54	0.48	3.04	0.46	0.68	0.70
Nd	77.26	211.04	0.77	0.49	2.48	0.57	1.84	1.75	9.23	1.44	2.57	3.17
Sm	16.75	46.29	0.17	0.10	0.31	0.06	0.25	0.23	2.33	0.43	0.61	1.08
Eu	2.92	7.07	0.07	0.05	0.11	0.01	0.12	0.04	0.07	0.03	0.55	0.22
Lu	0.36	0.94	0.07	0.11	0.01	0.002	0.02	0.02	0.15	0.10	0.74	0.76
Ta	0.06	0.04	2.25	1.59	0.15	0.29	0.08	0.17	2.04	0.27	0.83	1.05
W	0.04	0.02	0.15	0.41	0.04	0.01	0.00	0.02	0.07	0.04	1.59	1.08
Pb	0.87	1.59	8.02	5.09	0.12	0.13	0.05	0.01	1.88	0.38	6.36	1.67
Th	5.97	8.88	0.13	0.28	0.01	0.003	0.03	0.02	0.14	0.07	0.18	0.15
U	1.88	3.07	0.53	0.78	0.02	0.005	0.11	0.09	1.41	1.20	0.91	1.03

The tourmalines from the **Lindvikskollen** pegmatite are richer in Mg than the Tangen, Dalane and Spro tourmalines. These tourmalines have the highest concentration of Ti, Sc, W, Th, and U among the investigated samples.

Regarding the tourmaline chemistry of the rocks associated to the Lindvikskollen pegmatite, the tourmalines of the metagabbro and albitite are very similar, while the pegmatitic and granitic tourmalines share a few similarities with each other. Still, some variations between the Lindvikskollen tourmalines are described below.

All the investigated Lindvikskollen pegmatite tourmalines have Na concentrations between 0.70 and 0.82 apfu, and the K content is lower than 0.02 apfu. Tourmalines of the host rocks have a higher concentration of Al (~ 6.00 apfu) than the pegmatitic tourmalines (~ 5.05 apfu; Figure 8-12). Al in the X-site is the highest in the metagabbro and the albitite tourmalines. While the X-site of the pegmatitic tourmaline lacks Al but is richer in Ca (0.23 apfu) than the host rocks (0.15 to 0.07 apfu).

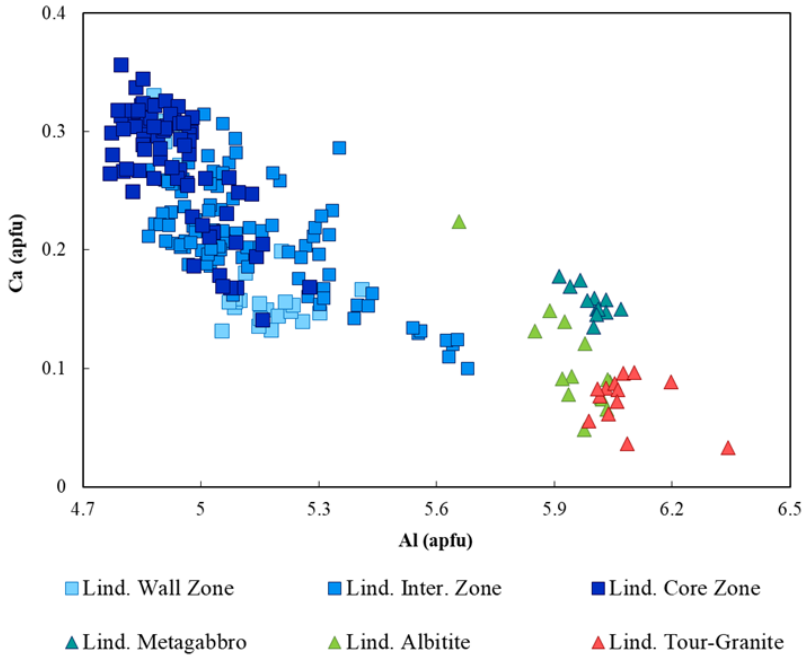

Figure 8-12 - Al vs Ca (apfu) discrimination plot showing that the tourmalines found in the host rocks are richer in Al and poorer in Ca, the opposite of the pegmatitic tourmalines. Lind.: Lindvikskollen; Inter.: Intermediate; Tour-Granite: Tourmaline-bearing granite.

As schorls, the granitic dyke and pegmatite tourmalines are richer in Fe (2.36 and 2.57 apfu) than the dravites from the metagabbro and albitite (0.45 and 0.51 apfu). The granitic dyke tourmaline has very low concentrations of Mg (0.31 apfu), while the metagabbro and the albitite tourmalines are the richest in Mg (2.26 and 2.20 apfu). The tourmaline's Li content in the metagabbro and albitite (3.4 and 5.8 ppm) is lower than in the pegmatite (12.6 to 33.8 ppm) and granitic dyke (130 ppm). The pegmatite tourmaline is richer in Ti (0.16 apfu) than the tourmalines of the host rocks, while the albitite tourmalines have the highest Ti concentration among the host rocks (0.11 apfu). The tourmalines from the granitic dyke have by far the highest concentration of Mn (5829 ppm) in comparison with the tourmalines from the pegmatite (1273 to 1807 ppm), and the metagabbro (39.4 ppm) and albitite (44.3 ppm) tourmalines (Figure 8-13). The pegmatite and metagabbro tourmalines have slightly higher concentrations of F (0.13 apfu) than the albitite tourmaline (0.09 apfu), while the granitic dyke tourmaline is F-poor (0.01 apfu).

Regarding their trace element concentrations (Figure 8-13), the pegmatite's schorl is richer in Sc, Co, Zr, Ga, W, Th, U, but is poorer in P, in comparison with the host rock tourmalines. The metagabbro's dravite has the highest concentrations of V and Cr, yet is depleted in Y, Ta and Cs in comparison with the rest of the Lindvikskollen tourmalines. In contrast, the tourmaline from the albitite is richer in Sr, and has the lowest concentrations of Sc, Zr, Ce, La, Nd and Sm. Tourmalines from both the metagabbro and albitite are richer in Ni, and slightly in Mo, in comparison with the pegmatite and granitic dyke tourmaline, but more depleted in Zn, Ga, Sn, Pb, U, Rb, Ba, Be, Nb. The schorl from the granitic dyke is the richest of the Lindvikskollen tourmalines in REE, Y, Ta, Nb, Mn, Be, Ba, P, among other trace elements. All Lindvikskollen tourmalines have consistent concentrations of Cu and Eu.

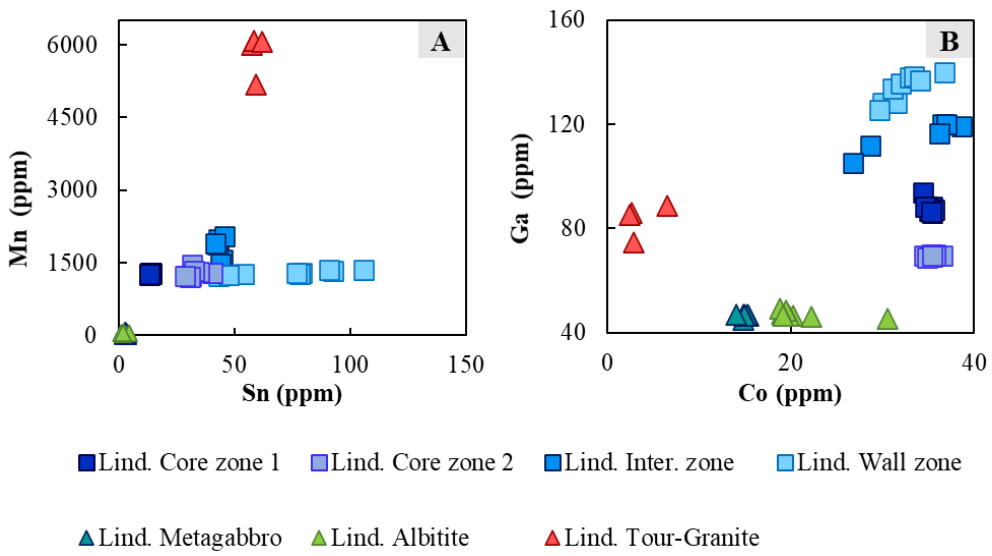

Figure 8-13 - Trace element plots of the tourmalines of the Lindvikskollen pegmatite and other Lindvikskollen area rocks. **A:** Sn vs Mn (ppm) plot showing that tourmalines of the albitite and metagabbro have the lowest concentrations of Sn and Mn, while the granitic dyke tourmalines have the highest concentrations of these elements. **B:** Co vs Ga (ppm) plot showing that the tourmalines of the albitite and metagabbro have the lowest concentrations of Ga, the tourmalines of the granitic dyke have the lowest concentration of Co, whereas the in average the pegmatite tourmalines have the highest concentrations of Ga and Co out of the Lindvikskollen rocks. Lind.: Lindvikskollen; Inter.: Intermediate; Tour-Granite: Tourmaline-bearing granite.

The tourmaline chemistry of the **Tangen** pegmatite differs significantly from the other investigated pegmatites. These tourmalines have the highest concentrations of Fe^{2+} (3.83 apfu), Na (0.94 apfu), Mn (0.48 apfu), and K (0.03 apfu), and the lowest concentrations of Al (4.55 apfu) and Mg (0.003 apfu), as well as very low Ca (0.02 apfu), and Xvac (0.007 apfu). Their Mg/(Mg+Fe) values are the lowest, average of 0.0008, and Xvac/(Xvac+Na) of 0.008. Ti concentration is very similar to the Lindvikskollen and Ramfoss pegmatite (~ 0.16 apfu). The Tangen tourmaline is the richest in Cu, Zn, Ga, Rb, Sn, Ba and Pb (Figure 8-14B, D); it has a relatively high concentration of Sb and Lu. And it has the lowest content of Nd, Sm and Eu out of all the pegmatites.

The **Dalane** tourmaline is the richest in Al (6.57 apfu) and has the highest concentration of Al in the X-site (0.57 apfu). Its Xvac is the highest from all tourmalines, and as such it has the lowest value of Na and K, giving it the closest composition to foitite. Ti is very low in this tourmaline (~ 0.01 apfu), a similar content to the Spro tourmaline. Regarding its trace elements,

Dalane has the highest concentration of Nb, and hosts the lowest concentrations of P, V, Cr, Co, Ni, Sr, Y, Zr and Ba (Figure 8-14A, C, D).

The **Havredal** dravite has the highest concentrations of Mg (2.07 apfu), out of all pegmatite tourmalines, as well as the lowest content of Fe^{2+} (0.83 apfu), Li (1.50 ppm), F (0.02 apfu) and Mn (28.3 ppm). F in the Havredal sample is one of the lowest, 0.02 apfu, close to the content of 0.03 apfu of the Ramfoss dravite. The Havredal tourmaline is the richest in P, V, and Cr; it is the poorest in Be, Zn, Nb, Ta and Pb, and it is depleted of Rb, Sb, W and U (Figure 8-14A, B).

The Ramfoss dravitic tourmaline is richer in Mg (1.67 apfu) than Fe^{2+} (1.42 apfu), yet their apfu values are closer in comparison to other investigated tourmalines. This tourmaline has the highest value of Ca (0.26 apfu) and Ti (0.18 apfu), the latter value is close to the Lindvikskollen and Tangen tourmalines. The Ramfoss sample, just as the Havredal one, has low F and Mn content. This dravite has the highest content of Ni, Sr, Ce, Pr, Nd and Eu, and the lowest content of Ga and Sn (Figure 8-14A, C, D).

The **Spro** pegmatite schorl has one of the highest contents of Al (6.5 apfu), with 0.43 apfu of Al on the X-site, and the lowest concentration of Si from all pegmatites (5.9 apfu). Spro is the most F-rich (0.5 apfu) and Li-rich (416.2 ppm) tourmaline of the studied samples, and it has one the lowest concentrations of Mg (0.04 apfu) and Ti (0.02 apfu). Fe^{2+} content (2.57 apfu) is similar to Lindvikskollen's tourmaline. The Ca content is close to the Tangen and Dalane pegmatites. Regarding its trace element geochemistry, it has the highest concentrations of Be, Cs and Ta, as well as relatively high values of Co and Zr similar to the Lindvikskollen pegmatite schorls, and the lowest concentrations of Sc, La, Ce and Pr (Figure 8-14C).

Regarding the gneissic host rock of the Spro pegmatite, this dravite has a Mg content of 1.56 apfu and Fe^{2+} of 0.98 apfu. It is poorer in Fe^{2+}, Na, F, Mn, Li, and richer in Mg, Ca and Ti than the Spro pegmatite schorl. The trace elements of the pegmatite and the gneiss tourmalines were compared as well. Both tourmalines have similar contents of Sm and Ba. The gneiss dravite has a higher concentration of V, Cu, Eu and Lu than the pegmatite's schorl, it also has relatively high content of Mo and Sb. The pegmatite, instead, is richer in Be, Co, Zn, Ga, Sn, Nb and Ta.

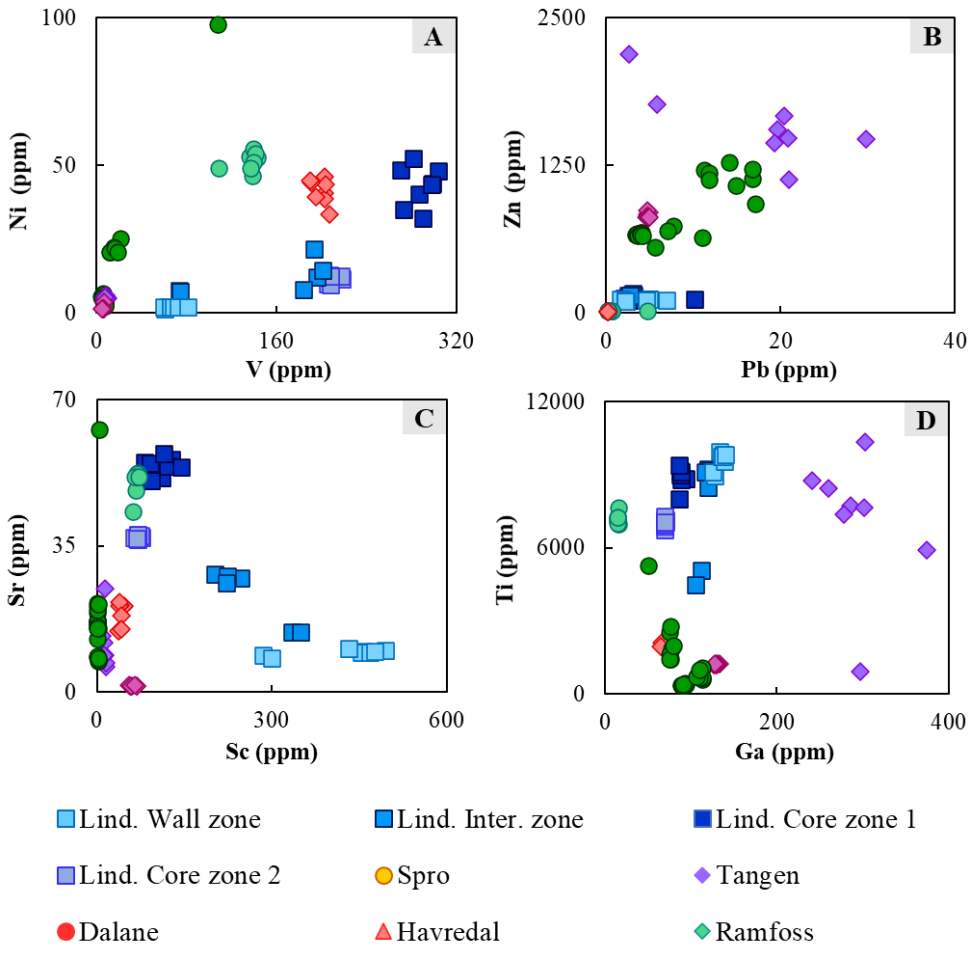

Figure 8-14 - Tourmaline trace element plots of the investigated pegmatites. **A:** V vs Ni (ppm) plot showing a positive correlation between these elements in the Lindvikskollen pegmatite tourmalines, which are the richest in V. The Ramfoss and Havredal dravites are the richest in Ni. **B:** Pb vs Zn (ppm) plot showing that the Tangen tourmaline has the highest concentrations of these elements, followed closely by the Spro and Dalane tourmalines, while most of the other tourmalines have low concentrations of Zn and Pb. **C:** Sr vs Sc (ppm) plot. The Lindvikskollen pegmatite tourmalines show a negative correlation of these elements, illustrating an increase of Sr and a decrease of Sc from the wall towards the core zone. All the other pegmatitic tourmalines have very low Sc. **D:** Ga vs Ti (ppm) plot which shows that the Tangen tourmaline has the highest concentration in Ga, while the Lindvikskollen pegmatite in average has the highest concentration in Ti out of all the analysed tourmalines. Lind.: Lindvikskollen; Inter.: Intermediate.

8.3.2. Pegmatite-internal variation of tourmaline compositions – the Lindvikskollen pegmatite

The major, minor and trace element chemistry of tourmalines from different zones of the Lindvikskollen pegmatite were analysed in order to determine their differences. The Lindvikskollen tourmalines exhibit some chemical variation from one pegmatite zone to another. Table 8-3 and Table 8-4 details the tourmalines average concentrations of major and minor elements of each pegmatite zone, and the plots in Figure 8-15 and Figure 8-16 graphically illustrate the distribution of selected elements.

The tourmaline of the **wall** zone is the richest in Fe^{2+} (2.50 apfu) and Ti (~ 9548 ppm; Figure 8-14D), and slightly richer in Na (0.74 apfu; Figure 8-16A) and K (0.02 apfu) than the other zones, it has the lowest concentration of Mg (1.22 apfu; Figure 8-16F), Ca (0.19 apfu; Figure 8-16E), F (0.10 apfu). Its Al content is similar to the intermediate zone tourmalines (~5.11 apfu), and Mn is similar to the core zone (~ 1284 – 1291 ppm). The wall zone is richer in trace elements than the other zones, namely in Sc, Ga, Sn, La, Ce, Pr and Nd (Figure 8-15B, C; Figure 8-16B, C, D). Yet, V, Ni, Sr and Eu are at their lowest concentration in the wall zone (Figure 8-15C; Figure 8-16G, H).

The tourmaline of the **intermediate** zone usually shows the intermediate concentrations between the core and wall zone, except for Ti, F, Mn and Li. Ti is slightly more depleted in the intermediate zone (0.15 apfu) than in the rest. In contrast, the intermediate zone has the highest concentration of F (0.15 apfu), Mn (1807.8 ppm) and Li (33.8 ppm). The trace elements that are more concentrated in the intermediate zone are Y, Nb, Ta, W and U; others like P, Cr, Cu and Zn, are only slightly richer in the intermediate zone.

The tourmaline of the **core** zone has the highest concentrations of Mg (1.52 apfu) and Ca (0.28 apfu), and it is slightly depleted in Al (4.92 apfu) and Na (0.70 apfu), in comparison with tourmalines of the other zones. It has almost identical concentrations of Fe^{2+} as the intermediate zone (~ 2.34 apfu). V, Sr and Zr are the trace elements with a notable higher concentration in the core zone (Figure 8-16G, H). LA-ICP-MS was performed in two tourmaline samples from two separate core zones of the pegmatite. Overall, they show similar concentrations of most trace elements, nevertheless some differences can be noted: Core 1 (sample 12062018; Figure 8-1), from

the W core mine, is richer in Be, Sc, Sn, Ti, V, Ni, Sr, Y, Zr, Nb, Sb, Cs, Th and U (Figure 8-16B, D, G, H) than core 2 (sample 20252; Figure 8-1), from the E core mine.

Some trace elements in the tourmalines of the wall zone have approximately the same average concentrations as the ones from the core, these include Zn, Nb, Cr, Cu, Be, Sm, Lu, Y, Mo and P. Co has constant concentrations throughout all tourmalines, independent of the pegmatite zone they occur. In addition, Ga shows a positive correlation with K, Sn and Sc, with increasing content from the tourmalines of the core zones outwards to the tourmalines of the wall zone (Figure 8-15A, B, C). In contrast, V and Sr concentrations increase from the wall inwards towards the core zones (Figure 8-15D).

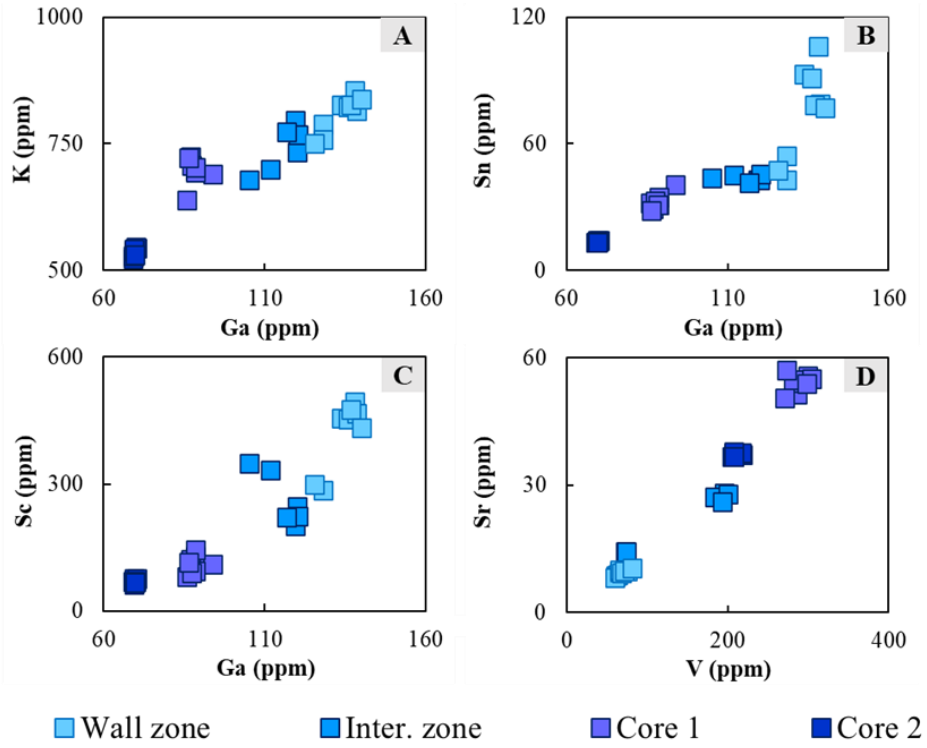

Figure 8-15 - Trace element plots of the tourmalines from each zone of the Lindvikskollen pegmatite. **A:** Ga vs K (ppm) plot displaying a decrease of K and Ga from the wall zone inwards towards the core zones. **B:** Ga vs Sn (ppm) plot showing that Sn and Ga is depleted in tourmaline from the wall towards the core zone. **C:** Ga vs Sc (ppm) plot showing the Sc and Ga depletion in tourmaline from the wall towards the core zone. **D:** V vs Sr (ppm) plot, illustrating a positive correlation between these elements from the wall towards the core zone. Inter: intermediate.

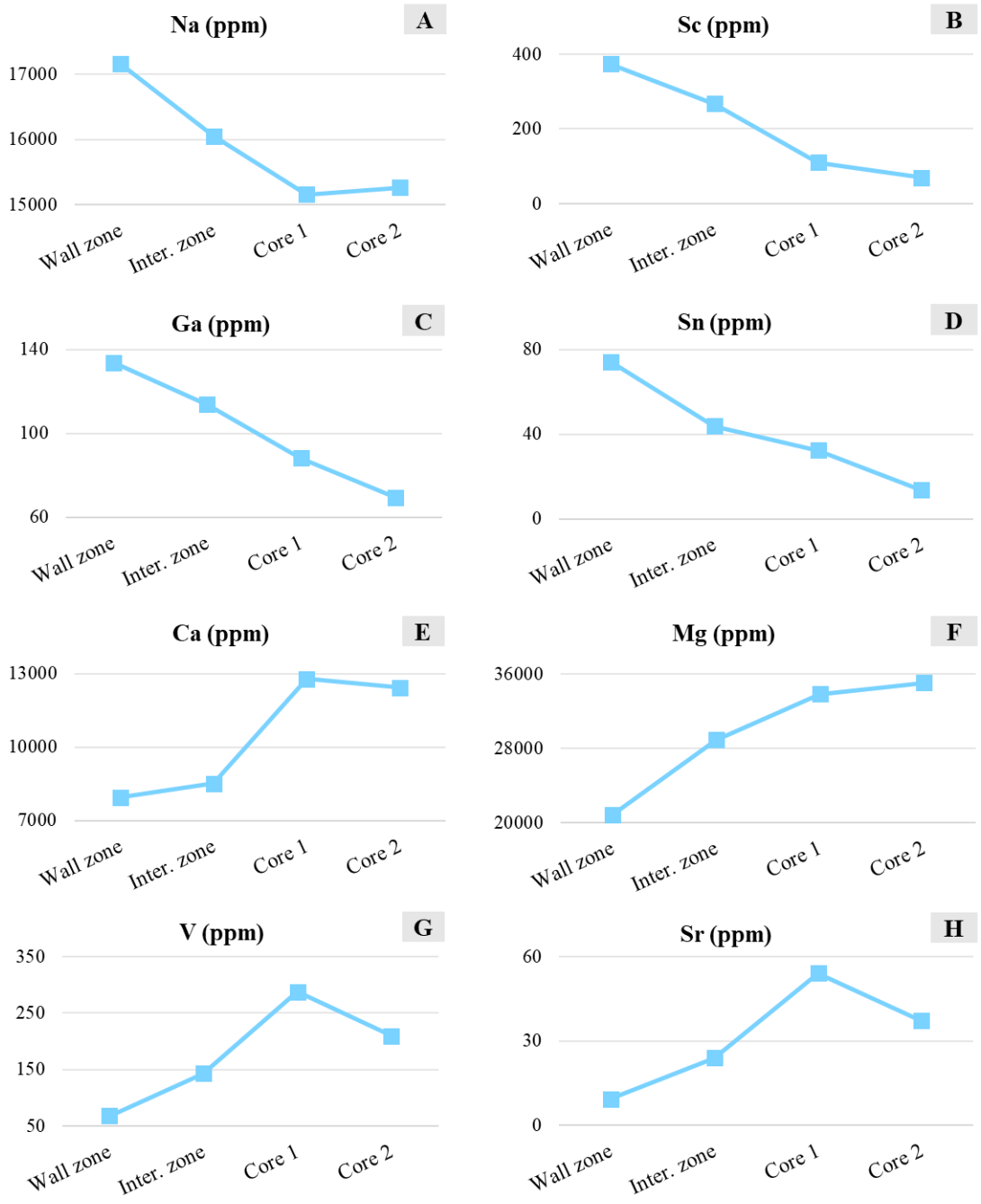

Figure 8-16 - Profile plots of average trace element contents of tourmalines from the Lindvikskollen pegmatite, showing the element content variation between the wall, intermediate and core zones. **A, B**, **C** and **D**: Na, Sc, Ga, and Sn concentrations in tourmaline decrease from the wall zone towards the core zones. **E**, **F**, **G** and **H**: show the increase of Ca, Mg, V, and Sr content in the wall zone tourmalines inwards to the tourmalines in the core zones. Inter.: Intermediate.

8.4. Boron isotopic compositions of tourmaline

One tourmaline sample from each studied pegmatite was analysed with SIMS for boron isotope compositions, as well as a tourmaline crystal from the host rock of the Spro pegmatite. The latter was analysed to complete the boron isotope studies performed by Faria (2019). Sample numbers are presented in Table 7-1.

The B stable isotope analysis of tourmalines yielded $\delta^{11}B$ values ranging from –13.5‰ to +9.7 ‰. The tourmaline $\delta^{11}B$ data of the analysed samples are presented on Table 8-5, and graphically presented on Figure 8-17.

The analyses revealed that the $\delta^{11}B$ values from the Bamble Sector tourmaline samples are relatively similar to each other. The Kragerø area specimens - Lindvikskollen and Tangen pegmatites - show overlapping values: Lindvikskollen's tourmalines display a larger range of $\delta^{11}B$ values from -1.9 to -1.0‰, averaging at -1.4‰. Whereas Tangen's $\delta^{11}B$ range is smaller, from -1.4 to -1.0‰, with an average of -1.3‰

Continuing with tourmalines from the Bamble Sector, samples from the Havredal and Dalane pegmatites have more positive $\delta^{11}B$ values than the previous ones. $^{10}B/^{11}B$ ratios of tourmaline from the Dalane pegmatite vary from +0.6 to +1.0 ‰, with an average of +0.8‰. Pegmatitic tourmaline from Havredal has the more positive $\delta^{11}B$ values from the Bamble sector, its values range from +1.8 to 2.4‰, averaging on +2.1‰.

The other Sveconorwegian tourmalines show extremely different values relative to each other and the Kragerø specimens. The Ramfoss pegmatite tourmaline has the highest $\delta^{11}B$ values, varying from +9.5 to 9.9‰, with an average of +9.7‰. In contrast, the Spro pegmatite tourmalines show negative $\delta^{11}B$ values, from -13.8‰ to -12.5‰, averaging on -13.0‰. This data overlaps with the analysed Spro host rock tourmalines, which yielded the lowest $\delta^{11}B$ values of all analysed tourmalines, ranging from -14.8‰ to -12.9‰, with an average of -13.5‰.

Table 8-5 - Average B isotopic compositions of tourmaline samples represented by $\delta^{11}B$ values (‰). SD: standard deviation; n: number of analyses. *B isotopic data from Faria (2019).

Sample	$\delta^{11}B_{low}$	$\delta^{11}B_{high}$	$\delta^{11}B_{mean}$	SD	n
Lindvikskollen	-1.9	-1.0	-1.4	0.36	5
Tangen	-1.4	-1.0	-1.3	0.17	9
Dalane	0.6	1.0	0.8	0.14	7
Havredal	1.8	2.4	2.1	0.21	5
Ramfoss	9.5	9.9	9.7	0.13	6
Spro host rock	-14.8	-12.9	-13.5	0.59	8
Spro pegmatite*	-13.8	-12.5	-13.0	0.13	41

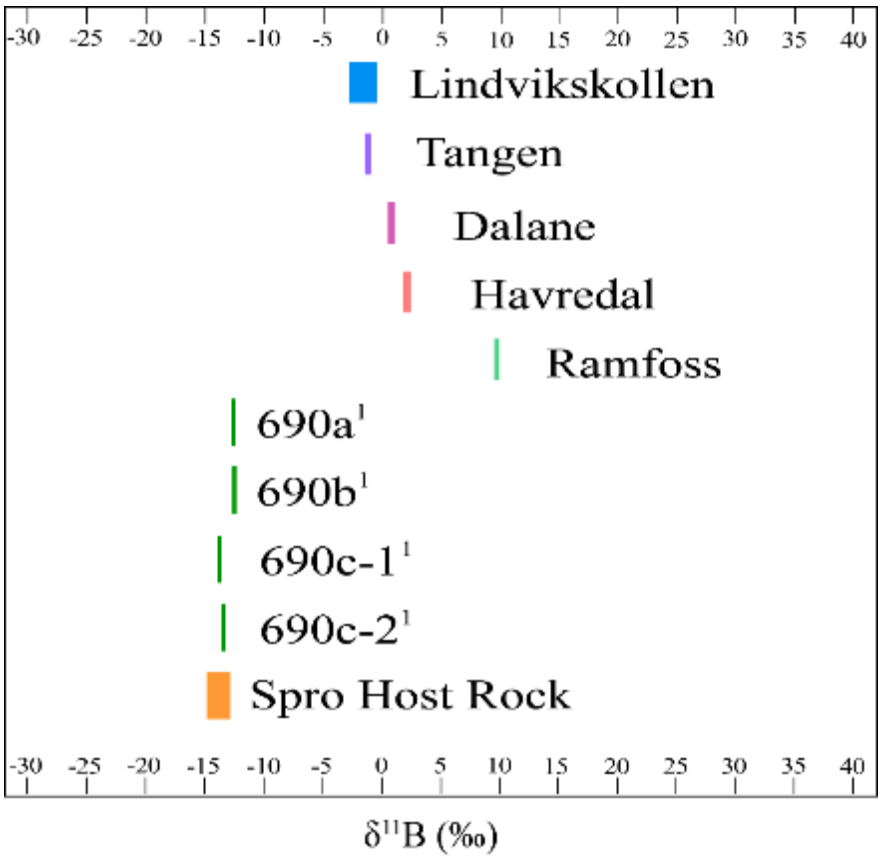

Figure 8-17 - δ^{11} range values of the analysed samples. [1] B isotopic data from Faria (2019).

9. Discussion

9.1. Bulk chemistry of the Lindvikskollen area rocks and implications for the pegmatite melt source

The most surprising result of the bulk rock data is that all samples of the Lindvikskollen area, including metagabbro, albitites, monzonitic gneiss, tourmaline-bearing granite and pegmatite wall rock, have in overall a relative similar element distribution pattern (Figure 8-8, Figure 9-1). All samples are enriched in Ti relatively to the UCC composition and depleted in Ba, K, La, Ce, Sr, and Nd. This indicates that in some way all rocks are genetically linked. This is obvious for the albitites which are metasomatic products of the metagabbro.

The A-type affinity of the pegmatite wall rock shown in Figure 8-7 confirms the mineralogical NYF characteristics of the Lindvikskollen pegmatite. The A-type signature of pegmatite melts can be produced either by residual melts of A-type granite intrusions or by partial melting of meta-igneous rocks. There is no granite pluton exposed in the Kragerø area which has a similar age as the pegmatites (Müller *et al.*, 2017; Rosing-Schow *et al.*, 2021) and A-type intrusions are not known from the Kragerø area. This suggests that the Lindvikskollen pegmatite formed by anatectic melting. Thus, the five possible melt sources are the metagabbro, the albitite, the monzonitic gneiss, tourmaline-bearing granite dyke or a rock that is not exposed at the surface.

The higher content of Rb, Cs, Nb, Ta, and LREE and the lower content of Sr, Ti, and Th of the tourmaline-bearing granite compared to the pegmatite wall zone indicates that the granite is more fractionated than the pegmatite. Even more distinctively is the strong negative Eu anomaly of the tourmaline-bearing granite (Figure 9-1; Figure 8-9). The pegmatite wall zone sample shows a weak positive Eu anomaly suggesting low or no fractionation. Thus, the pegmatite melt cannot originate from the tourmaline-bearing granite.

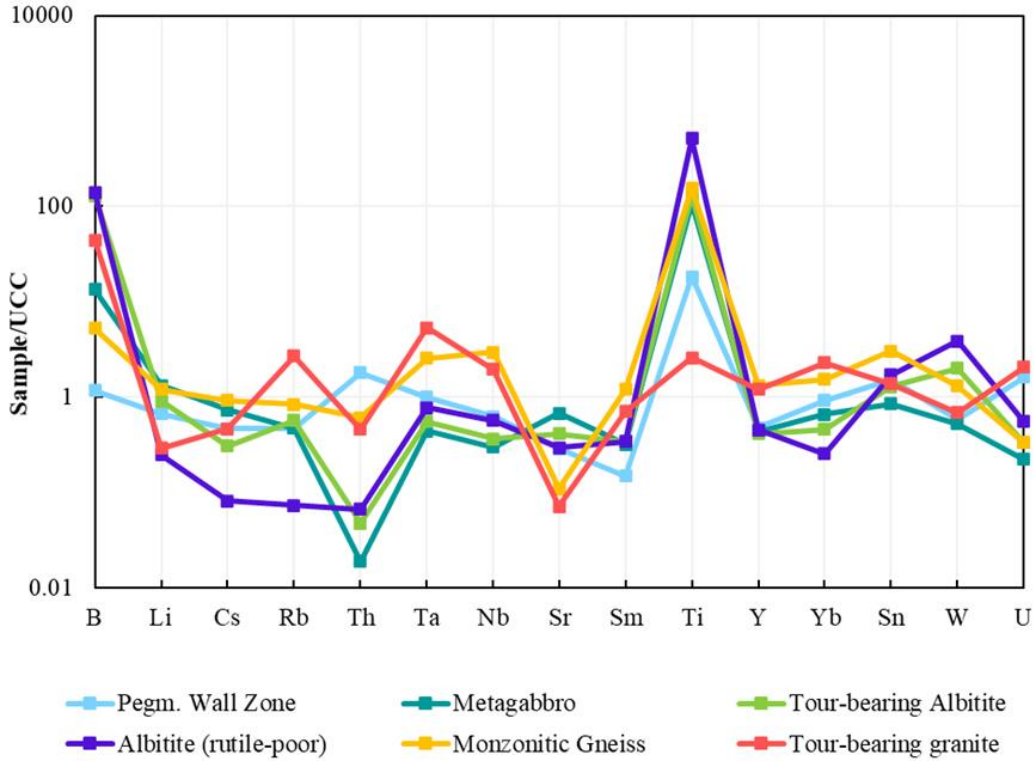

Figure 9-1 Spidergram of incompatible elements from the Lindvikskollen pegmatites and possible melt sources, normalized to the composition of the UCC (Rudnick & Gao, 2003). In comparison with the pegmatite wall zone: The tourmaline bearing granite shows a higher level of fractionation; the monzonitic gneiss has lower Sr; the metagabbro and albitites have very low Th content. The albitites host the highest concentrations of B. Pegm.: pegmatite; Tour: tourmaline.

The element distribution patterns of the metagabbro, the albitites, the monzonitic gneiss and the pegmatite are in general very similar (Figure 9-1; Figure 8-9). This implies that these rocks could be the melt source of the pegmatite. One difference is that the pegmatite wall zone is richer in Th, its content is closer to the monzonitic gneiss. This points to the gneiss being the pegmatite melt source. Nevertheless, in general Th is an incompatible element, including in amphibole, meaning that it would preferentially enter the melt rather than stay in the mineral during rock melting processes. The partial melting of the metagabbro could explain the large difference in Th between the metagabbro and the Th-rich pegmatite wall zone. Another difference in the element distribution pattern is the low Sr of the monzonitic gneiss compared to the metagabbro, the albitites and the pegmatite. In the case of partial melting of the metagabbro or albitites, plagioclase carrying most of the Sr would melt first. Thus, the first melts would be relatively high in Sr similar to that of the pegmatite wall zone. An additional argument in favour of the metagabbro as the pegmatite

melt source is the similar alkali content of those rocks compared to the higher alkali concentrations of the monzonitic gneiss (Figure 8-5). The tourmaline-bearing albitite and the rutile-poor albitite have the highest concentrations of B out of the analysed rocks (Figure 9-1). Thus, it is highly possible that the albitites contributed to the B in the pegmatite melt.

The REE patterns of the monzonitic gneiss and the pegmatite are the opposite of each other, the monzonitic gneiss has high LREE, low HREE, and a weak negative Eu anomaly compared to the pegmatite wall zone (Figure 8-9). The metagabbro and the albitite (rutile-poor) have a flatter LREE and a decreasing HREE trend, in contrast with the pegmatite low LREE and increasing HREE pattern. While the tourmaline-bearing albitite, in general, has the opposite REE pattern of the pegmatite. However, both the metagabbro and pegmatite wall zone have a negative Eu anomaly, as well as a few similar REE concentrations (La, Dy, Yb). In contrast, the albitites have a slightly negative Eu anomaly. Yet, have similar HREE concentrations (Dy, Ho, Er) with the pegmatite wall zone.

In conclusion, it is suggested that from the analysed rocks of the Lindvikskollen area mixed partial melting of the albitites and metagabbro is most likely the melt source of the pegmatite.

9.2. Tourmaline chemistry of pegmatites and their host rocks and implications for pegmatite melt crystallization and origin

This subchapter utilizes the tourmaline chemistry of the investigated pegmatites and host rocks in order to better understand the genesis of pegmatite melt and its crystallization process. Variations in tourmaline chemistry are controlled by (1) the overall availability of the elements in the pegmatite melt, (2) the co-existence of other minerals which may buffer the element availability, (3) the substitution behaviour of the element in respect to the tourmaline crystal structure, (4) the P-T conditions, and/or (5) the oxygen fugacity (fO_2) of the pegmatite melt. These factors are taken into account in the following discussion to explain the observed chemical variation of the investigated tourmalines. Tourmaline is more commonly found in LCT pegmatites, and rarely occur in NYF pegmatites (Ercit, 2005; Ercit *et al.*, 2003; London, 2008). Since the Sveconorwegian pegmatites studied in this thesis have a NYF signature (Müller *et al.*, 2017) and contain tourmaline, the question rises, where does the B come from?

9.2.1. Boron saturation in pegmatite melts with respect to tourmaline

Countless experimental studies have contributed to the understanding of tourmaline crystallization in terms of B_2O_3 content in the melt. For tourmaline to crystallize in peraluminous granites, with ASI between 1.2 and 1.4, as an early liquidus phase it requires ~ 2 wt.% B_2O_3 (~ 6200 pm; London, 1997; Wolf & London, 1997) to be in excess in the initial bulk melt. However, concentrations in the melt lower than 0.5 wt.% B_2O_3 (~ 1550 ppm; Dingwell *et al.*, 1996 and references therein) have been capable of producing tourmaline. Tourmaline stability depends not only on B content in the melt but can also depend on H_2O activity, fO_2, temperature and melt composition. Low H_2O activity and high fO_2 increases the stability field of tourmaline (Scaillet *et al.*, 1995). Temperature can influence the amount of B_2O_3 that is needed for tourmaline to form. At temperatures of 600ºC, 1 wt.% of B_2O_3 in a peraluminous melt can crystallize tourmaline, while ~ 2 wt.% is required at 750ºC (Wolf & London, 1997). Regarding melt composition, for example Al excess in the melt is necessary to produce tourmaline. The presence of F in association with Al in the system will lower the activity of Al in the melt, reducing the stability range of tourmaline (London, 1997; Wolf & London, 1997). Thus, more B_2O_3 is required to produce tourmaline. The average B concentration of the Earth's UCC is 17 ppm (Rudnick & Gao, 2003) (Table 4-1). Thus, in comparison an extreme enrichment of B needs to occur to crystallize tourmaline.

The analysed tourmaline-bearing granite of the Lindvikskollen area has 750 ppm of B, less than half of the B content threshold for tourmaline crystallization published by Dingwell *et al.* (1996), 1550 ppm. The wall zone of the Lindvikskollen pegmatite has 20 ppm B only. These rocks have ASI of 1 to 1.1 (Figure 8-6), which requires at least ~ 6200 ppm B to form tourmaline (London, 1997; Wolf & London, 1997). The pegmatite wall zone represents the least fractionated part of the pegmatite, which is why this value does not represent the B content of the whole pegmatite. In addition, a small amount of B escaped from the pegmatite melt during crystallization as documented by common tourmaline in the pegmatite host rocks near the contact. Thus, the detected B values of the pegmatite wall rock and the tourmaline-bearing granite does not represent the original B content of the melts. The tourmaline-bearing albitite and the rutile-poor albitite have 2210 and 2380 ppm of B, respectively. This amount of B in the melt can produce tourmaline, corroborating that the partial melting of the albitites contributed to the pegmatite forming melt.

9.2.2. Implications of the intra-pegmatite variations of tourmaline chemistry

In the Lindvikskollen pegmatite, schorl tourmaline occurs in every zone of the pegmatite with relative consistent chemistry, apart from a few notable variations in composition which will be discussed further below. The tourmaline distribution in the Lindvikskollen pegmatite is unusual compared to other tourmaline pegmatites worldwide. For example, in the Mt. Mica pegmatite in Maine, (USA; Simmons *et al.*, 2016) tourmaline is also present in all the pegmatite zones, yet its composition varies from zone to zone. In the Mt. Mica pegmatite, tourmaline composition changes from the wall zone to the core and pockets, from black tourmaline (schorl) to colour and colour-zoned tourmalines (elbaite). The tourmaline of the outer zones of the pegmatite are Fe-rich, and its composition evolves inwards with decreasing Fe content and increasing content of Al and Li, towards the core zone and pockets (Simmons *et al.*, 2005a; Simmons *et al.*, 2005b).

Fe/Mg ratio is relatively consistent for all tourmalines in the Lindvikskollen pegmatite, meaning that the pegmatite melt was rich enough in Fe and Mg to crystallize different generation schorl found in the wall, intermediate and core zones. However, there is a slight variation of **Mg** in the tourmalines of each zone (Figure 9-2A). In general, Mg becomes depleted in the melt as a pegmatite crystallizes, so it would be expected for it to be more concentrated in the tourmaline of the wall zone. Yet, in the Lindvikskollen pegmatite the opposite happens. The core zone tourmalines are slightly richer in Mg than the wall zone tourmalines (1.52 to 1.22 apfu / 35000 to 21000 ppm). This could be explained by the substitution of Mg and Fe in the Y- and Z-site in the tourmaline structure due to varying P-T conditions and fO2 (*e.g.*, Benard *et al.*, 1985). Experiments conducted on tourmaline-bearing leucogranites showed that low fO_2 can increase the Fe/(Fe + Mg) ratio of the crystallizing tourmaline, while decreasing temperature lowers Fe/(Fe + Mg) (Benard *et al.*, 1985).

Some element contents in tourmaline from the different zones vary significantly, indicating changing conditions during pegmatite crystallization. In particular, Na, Sc, Ga, and Sn contents in tourmaline decrease from the wall zone towards the core zone, whereas concentrations of Ca, V, and Sr increase (Figure 8-16).

Ca and **Na** have a negative correlation, both occupy the X-site in tourmaline (Figure 9-2B; Figure 8-16A, C). The crystallization of K-feldspar and albite consumes the majority of Na. Therefore, the concentration of Na decreases in the pegmatite melt with progressing crystallization

and increasing fractionation. This would explain why less Na is incorporated in the late-stage tourmalines of the pegmatite core. In pegmatites, Ca is generally absent in late-stage tourmalines (London, 2016; London *et al.*, 1989), as it should become equally depleted in the melt, like Na, as the pegmatite forms. However, the Lindvikskollen tourmalines behave in the opposite way: Ca is highest in the late-stage tourmalines. The increase in Ca in the core zone tourmaline might be the result of contamination of the pegmatite melt by the metagabbro, which is rich in Ca (London, 2016); or flux-rich melts that contain Ca at the late crystallization stage, as proposed by the experimental studies on the differentiation of granitic pegmatites by London (1989). Still, it can also be that the Na content of the wall and intermediate zone tourmalines is so high, that no more Ca can enter the tourmaline structure, because both elements occupy the X-site.

Sc is generally a compatible element. Thus, the observed Sc depletion in late-stage tourmaline reflects its compatible behaviour in the crystallizing pegmatite melt. Its late-stage depletion in the melt is most likely caused by the crystallization of co-genetic Sc-bearing minerals such as micas (*e.g.*, Steffenssen *et al.*, 2019) (Figure 8-16D). **Ga** is in general an incompatible element (Kontak & Martin, 1997; Larsen, 2002). In granitic rocks K-feldspar and micas are rich in Ga, this has been shown by geochemical studies of the Land's End granite (Müller *et al.*, 2006), and the Evje-Iveland, Tørdal and Froland pegmatites (Larsen, 2002; Rosing-Schow *et al.*, 2019). In strongly peraluminous granites Ga concentrations can reach 60 ppm in feldspars and 170 ppm in micas (Breiter *et al.*, 2015). This relative compatibility of Ga in respect to feldspar and mica would explain the observed decrease of Ga in late-stage tourmaline (Figure 8-16F). Because feldspar and mica crystallize in large quantities all the time in the Lindvikskollen pegmatite, these minerals mostly absorb the available Ga in the melt.

Sn is commonly an incompatible element, yet in the Lindvikskollen pegmatite its content is lower in the late-stage tourmalines (Figure 8-16H). However, in pegmatites Sn preferentially enters mica (London, 2008; Rosing-Schow *et al.*, 2019) but it is also compatible to rutile, titanite, and ilmenite. All these accessory minerals occur at Lindvikskollen and incorporate Sn in their structure. Thus, these Sn-compatible minerals most likely buffered the Sn content of the Lindvikskollen pegmatite melt and its availability to be incorporated in the late-stage tourmalines.

V content in tourmaline increases from the wall zone towards the core zone of the Lindvikskollen pegmatite (Figure 8-16E). The experimental tourmaline/melt partitioning studies

of van Hinsberg (2011) show that V partitions easily into tourmaline and biotite. In this thesis it is suggested that V is more compatible to biotite than tourmaline in the Lindvikskollen pegmatite, explaining the observed V decrease in co-existing tourmalines.

The Lindvikskollen tourmalines from the core zone are richer in **Sr** than the wall zone tourmalines (Figure 8-16G). Sr is generally compatible in feldspars, in particular in Ca-poor plagioclase, so it is to be expected that in the late-forming tourmaline Sr content would be low (*e.g.*, Larsen, 2002). One explanation could be that the major feldspar which crystallizes is K-feldspar. K-feldspar does not incorporate as much Sr as plagioclase. Hence, it might be the case that the Lindvikskollen pegmatite melt became slightly richer in Sr with progressing pegmatite crystallization.

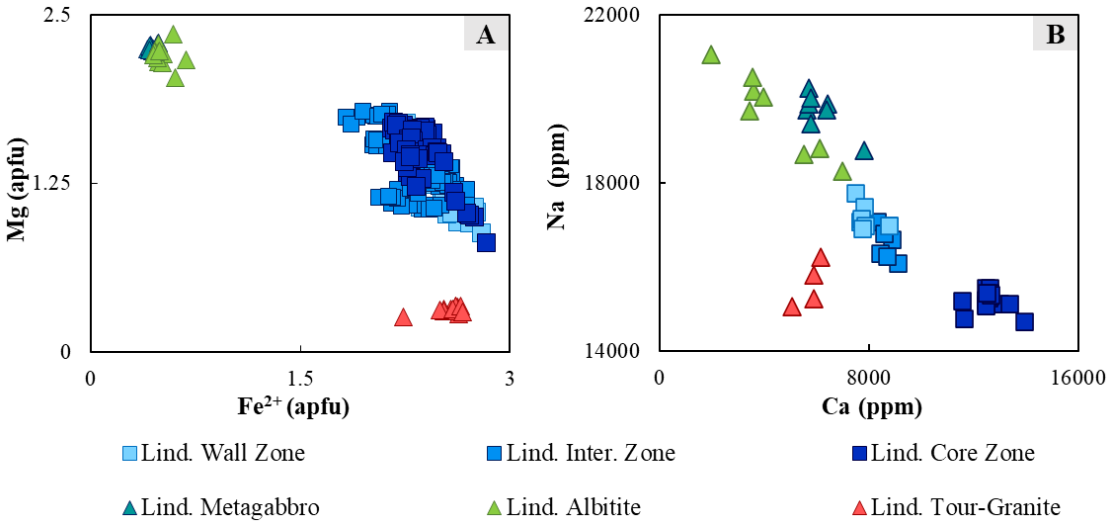

Figure 9-2 Tourmaline's major elements plots of the Lindvikskollen pegmatite, host rocks and granitic dyke. **A:** Fe^{2+} vs Mg (apfu) diagram. A negative correlation is observed in the tourmalines of the Lindvikskollen rocks. Tourmalines from the host rocks are richer in Mg, while the tourmaline-bearing granite is the richest in Fe^{2+}. **B:** Ca vs Na (ppm) diagram, a clear trend between the pegmatite tourmalines and host rock tourmalines can be observed. The tourmalines from the granite plot away from this trend, implying that the pegmatite and granite are unrelated. Lind: Lindvikskollen; Inter.: Intermediate; Tour-Granite: tourmaline-bearing granite.

9.2.3. Variation of tourmaline chemistry of the Lindvikskollen pegmatite and its host rocks: Magmatic versus hydrothermal conditions?

During fieldwork, tourmaline was also found in the host rocks of the Lindvikskollen pegmatite: the metagabbro, as well as its metasomatized albitite parts. Taking into consideration the field descriptions: (1) tourmaline in the host rocks occur only close to the pegmatite contact (< 10 m); And (2) structural evidence implies that this tourmaline crystallized partially along cracks. This suggests that the dravites that are found in the host rocks, near the pegmatite contact, were formed by the infiltration of B-bearing fluids derived from the crystallizing pegmatite. This implies that the crystallization temperature of the host rocks tourmalines was somewhat lower than that of the pegmatite tourmalines and most importantly, they crystallized from an aqueous fluid.

Pegmatites can reach their solidus with a portion of their original boron in the melt or vapour phase in their innermost zones, which will ultimately seep through the host rocks (London, 2008; Morgan & London, 1987). Tourmaline crystallization at lower temperatures (such as those of the host rock) requires less B for saturation of the melt or aqueous vapor than at magmatic conditions (London *et al.*, 1996). These B-rich fluids will react with the host rocks leading to pervasive tourmalinization, since they contain sufficient Mg, Fe and Al to retain the B in tourmaline. When localized, this tourmaline replacement is formed from the late-stage B-rich fluids that originate from pegmatites (London, 2008).

Hydrothermal tourmalines can display unusual compositions that are a consequence of their setting (Henry & Dutrow, 1996). Hydrothermal tourmalines associated with mafic and ultramafic rocks, such as the Lindvikskollen metagabbro, can locally be dravitic in composition, and have an enrichment in Cr, Ni and V (Henry & Dutrow, 1996).

Pirajno & Smithies (1992) distinguish magmatic and hydrothermal tourmalines based on their FeO/(MgO+FeO) ratios. The authors suggest that FeO/(MgO+FeO) ratios > 0.8 indicate magmatic crystallization conditions, and ratios < 0.6 indicate hydrothermal conditions. It is important to clarify that Pirajno & Smithies (1992) study was based on tourmalines associated with granite-related Sn and Sn-W hydrothermal mineralization. Furthermore, the authors suggest that tourmalines that have a non-granitic origin may have the same FeO/(MgO+FeO) ratios as those of distal hydrothermal tourmalines (< 0.6, C field; Figure 9-3). In the case of the

Lindvikskollen tourmalines, the data confirmed this discrimination: the host rocks dravites have ratios < 0.4 and the pegmatite schorls have ratios between ~ 0.6 to 0.9. The latter tourmalines plot mostly in the B field of Figure 9-3, which indicates a mixed origin between magmatic and hydrothermal conditions. Yet, the Lindvikskollen pegmatite tourmalines have a magmatic origin, evidenced by their occurrence as well-developed crystals present in all zones of the pegmatite body with roughly constant composition. Since Pirajno & Smithies (1992) based their work on granite related tourmalines, a discrepancy is noted between their diagram classification and petrological and geochemical observations of the tourmalines of the Lindvikskollen pegmatite, which origin is unrelated to a granite.

The composition of the investigated pegmatite tourmalines and host rock tourmalines are very different. Besides their classification (schorl/dravite), the host rocks tourmalines also differ from the pegmatite tourmalines by higher Mg, Na, Al, Sr, and Mo content, outstandingly higher Cr, V, and Ni concentrations, and lower contents of Fe, Ca, Mn, Ti, K, Zn, Li, Sc, Ga, Sn, Co, Pb, Be, Nb, Ta, and the analysed REE.

The average V content of the metagabbro-hosted tourmaline is outstandingly high. This high V content is most likely caused by leaching of V-bearing amphiboles in the metagabbro by the B-fluids. That means that the pegmatite-derived B fluids interacted with the host rock before crystallizing the tourmalines, documenting the aggressive chemical character of the fluids.

The continuous (linear) Na and Ca correlation trend observed for both host rock and pegmatite tourmaline at Lindvikskollen suggest that the dravites are fluid fractionation products of the pegmatite of one common source (Figure 9-2). The Na content in the albitite tourmalines is higher than in the metagabbro tourmalines, this could be caused by the dissolution of albite in the albitite.

Ti content decreases in the host rocks tourmalines. The B-bearing fluids possibly were not at a temperature and composition proper for the dissolution of Ti from Ti-bearing minerals (titanite, rutile) in the host rocks. Thus, less Ti enters the hydrothermal tourmalines relatively to the magmatic tourmalines.

In comparison with the wall-rock tourmalines of the Blackbird district (stratabound and breccia mineralization) studied by Trumbull *et al.* (2011), the tourmalines from the Lindvikskollen

metagabbro and albitite share some similarities: low Fe/(Fe+Mg) and Na/(Ca+Na) ratios, and consequently their classification as dravites. The authors conclude that the compositions of these tourmalines depend in part of the host rock lithology because in the Blackbird area dravitic tourmaline is only found in the biotite-rich host rock.

Other example of lithology dependent hydrothermal tourmaline is the Tanco granitic pegmatite and its metagabbro host rock (Selway *et al.*, 2000b). The hydrothermal tourmalines associated with this pegmatite formed due to the interaction of the Na-, Al- and B-rich pegmatite-generated fluid infiltration in the Ca- Mg- and Fe-rich metagabbro.

Furthermore, the tourmalines from the host rocks of the Lindvikskollen pegmatite have unusually high content of Mg in comparison with other hydrothermal tourmalines, such as the Blackbird tourmalines (*e.g.*, Trumbull *et al.*, 2011). Most hydrothermal tourmalines have higher Fe content (*e.g.*, experimental tourmaline: Morgan & London, 1989; Tanco pegmatite: Selway *et al.*, 2000a).

We attribute the increase in Mg, Na, Al, V, Cr, Sr, Mo, and Ni in the hydrothermal dravites of the metagabbro and albitite, in part to the interaction of the fluid that originated from the crystallizing pegmatite, with the host rocks mineralogy. These elements are present in the mineral assemblage of the rocks, for example, in the metagabbro: marialite scapolite, amphibole (edenite, pargasite and actinolite), ilmenite, rutile; and in the albitite: albite, magnesio-hornblende, sphene, rutile, diopside (Engvik *et al.*, 2018).

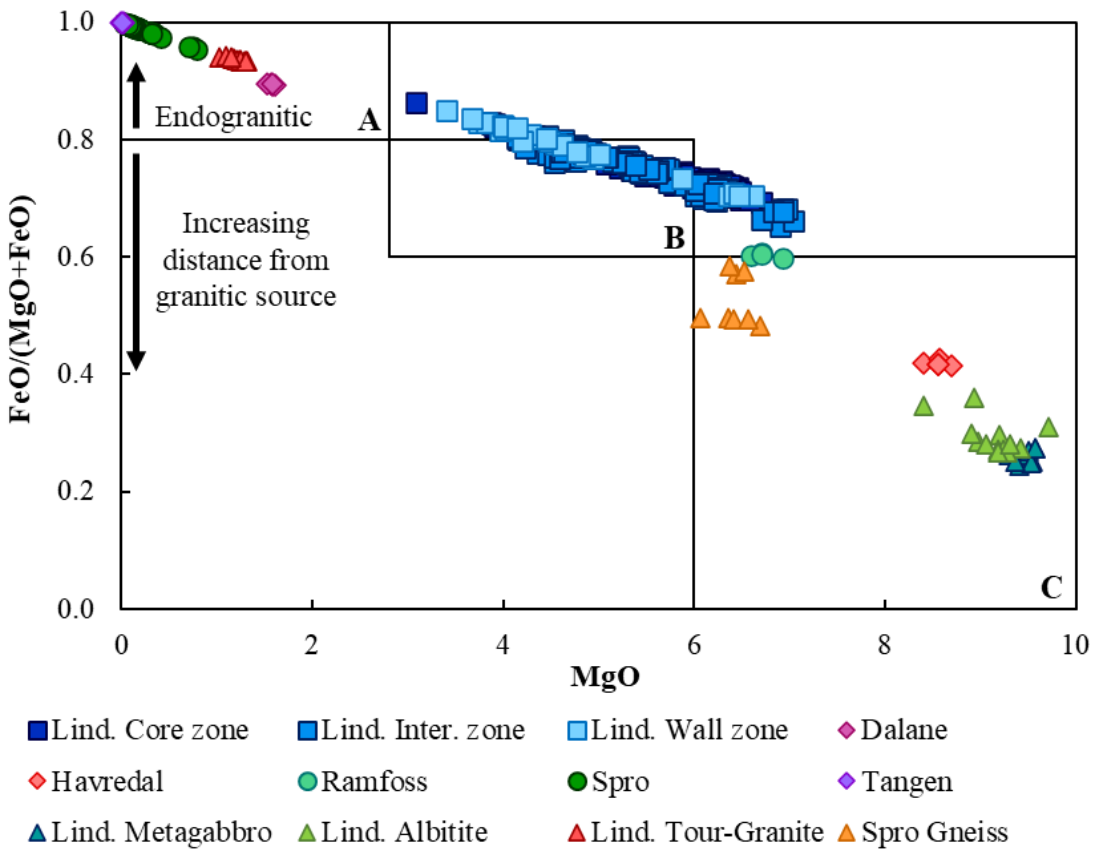

Figure 9-3 - MgO vs FeO/(MgO+FeO) diagram of the analysed tourmalines. This diagram shows a relation between the composition of tourmaline and its formation environment. This diagram was based only on tourmaline-bearing granites associated with Sn and Sn-W hydrothermal mineralization. Therefore, for the analysed pegmatite tourmalines that formed from the partial melting of host rocks this diagram can have diverging results from the petrological and geochemical observations. In relation to the granitic source: **A**: tourmalines associated with endogranitic to proximal environments. **B**: tourmalines from proximal to distal environments. **C:** tourmalines from distal environments, fluid-precipitated tourmalines. In relation to the origin conditions of tourmaline: **ratios > 0.8**: magmatic origin; **ratios < 0.6**: hydrothermal conditions; **ratios between 0.6-0.8**: mixed origin. Diagram modified from Pirajno & Smithies (1992). Lind.: Lindvikskollen; Tour-Granite: Tourmaline-bearing granite.

9.2.4. Differences between the Lindvikskollen pegmatite tourmalines and the granite tourmalines

The composition of the tourmalines in the granite dyke are similar to some granite hosted tourmaline compositions (*e.g.*, Balen & Petrinec, 2011; Buriánek & Novák, 2007; Drivenes *et al.*, 2015; Falster *et al.*, 2018; Yang *et al.*, 2015). The main similarities between the referenced tourmaline-bearing granites and the Lindvikskollen tourmaline granite is their Fe/Mg and Ca/Na

ratios, and schorl composition. In addition, the Lindvikskollen granitic schorls have similar trace element signatures as the tourmalines from the Land's End granite (Drivenes *et al.*, 2015) and the Qitianling batholith (Yang *et al.*, 2015), containing similar concentrations of Li, V, Ba, Nb, Ta, Zn, and Zr.

These compositions are very different to the Lindvikskollen pegmatite tourmalines. The Mg content in the granitic dyke tourmalines (0.31 apfu) is lower than those from the pegmatite (1.40 apfu) and host rocks tourmalines (~2.24 apfu). Also, Al, Fe, Mn, P, Li, Cs and Rb are higher in the granitic tourmalines than in the pegmatite tourmalines. The granite tourmalines show exceptionally lower concentrations of F, Ti, Co and V in comparison with the other Lindvikskollen tourmalines (pegmatite and host rocks). LREE, namely La, Ce, Pr, Nd and Sm, occur in higher concentrations in the granitic tourmalines than in the pegmatitic tourmalines. This further supports the theory that the tourmaline-bearing granite melts are more fractionated/evolved than the pegmatite melt, as it has higher concentrations of REE and incompatible elements, such as Cs and Rb. In addition, this indicates that the Lindvikskollen pegmatite melt has, in overall, a primitive granitic composition and it is unlikely that the melt fractionated from a large (hidden) granite pluton.

The granite dyke tourmalines plot away from the Lindvikskollen pegmatite and hydrothermal tourmaline in the Na and Ca trend shown in Figure 9-2. In addition, in the Pirajno & Smithies (1992) Feo/(MgO+FeO) vs MgO diagram the tourmalines of the granitic dyke plot in the endogranitic field, with FeO/(MgO+FeO) ratios above 0.8, indicating a magmatic origin (Figure 9-3).

Concluding, the tourmaline chemistry confirms that the melt source of the Lindvikskollen pegmatite cannot be the tourmaline-bearing granite, and it suggest that these rocks do not have a common melt source.

9.2.5. Differences between the Kragerø pegmatites.

The tourmalines from the Kragerø pegmatites Lindvikskollen, Dalane, Tangen and Havredal have quite distinctive major and trace element chemistries. Lindvikskollen, Dalane and Tangen pegmatites host schorl tourmalines whereas the Havredal pegmatite tourmalines have a dravitic composition (Figure 8-11).

As previously stated, the Lindvikskollen tourmalines FeO/(MgO+FeO) ratios plot in the magmatic to hydrothermal origin fields (~ 0.6 – 0.9) of the Pirajno & Smithies (1992) diagram. Dalane and Tangen have ratios that point to a purely magmatic formation environment (> 0.8). In contrast, the Havredal pegmatite dravites have ratios that suggest a hydrothermal origin (< 0.6) (Figure 9-3). However, the Havredal tourmalines have a magmatic origin, lacking the typical characteristics of hydrothermal tourmaline. Based on the investigated Sveconorwegian pegmatitic tourmalines, the diagram of Pirajno & Smithies (1992) effectively discriminates tourmalines if their origin is related to a granite. However, if their origin is unrelated to a granitic pluton the conditions of origin result in: schorl tourmalines form under magmatic conditions and dravites under hydrothermal conditions.

The diagram created by Breaks *et al.* (2003) (Figure 9-4) represents the level of host rock-pegmatite melt interaction (y-axis) vs the degree of evolution of a pegmatite (x-axis) depending on the composition of its tourmalines. This pegmatite characterization scheme is centred on tourmalines from granite-related pegmatites. Increasing host rock-pegmatite interaction refers to the contamination of the granitic melt by Ca-Mg-rich host rocks (*e.g.*, London, 1999; London *et al.*, 1996). In the case of the investigated Sveconorwegian pegmatites, their melt source is not related to a granitic pluton, which is why the y-axis of this diagram (Mg+Ti+Ca apfu) will be interpreted as an indicator of calcium-titanium-magnesium enrichment of the pegmatite protolith.

Lindvikskollen tourmalines have higher Ca and Ti content than the other tourmalines, as well as high contents of Sc, V, Sr, Co, Zr, W and relatively high REE, U, and Th. The enrichment in Ti, Sc, V and Sr in the tourmalines indicates that the pegmatite was formed by the partial melting of its host rocks, because the metagabbro and albitites are rich in these elements (Figure 8-8; Table 8-4). The relatively high concentrations in incompatible elements, such as the REE, U and Th indicate a high degree of melt fractionation, although these elements are more concentrated in the accessory minerals of this pegmatite.

The Tangen tourmaline distinguishes itself from the other Kragerø pegmatite tourmalines by having the highest concentrations of most analysed elements, for example: Fe, Na, Mn, Ga, Ba, Rb, etc., in addition to relatively high concentrations of Ti, similar in values to those of the Lindvikskollen tourmaline. Although the Tangen pegmatite intrudes the same metagabbro body as

the Lindvikskollen pegmatite, their tourmalines do not share many similarities regarding its trace element composition. This difference is in part a function of their pegmatite mineralogy, since the Tangen pegmatite lacks muscovite and biotite, the elements that would preferably partition into these minerals may be more easily incorporated in the tourmaline, namely: K, Fe, Mn, Rb, Na, Ba, Zn, and Ti. The Tangen tourmalines have low V, Al, Mg, Ca and Sc, which could signify that the melt is more evolved than the Lindvikskollen pegmatite melt. This is also proven by the fact that high Mn content in pegmatites is indicative of highly fractionated pegmatitic melts, as shown in Figure 9-4 (Breaks *et al.*, 2003). Lower Mg and Ca in the Tangen tourmalines, would suggests less host rock interaction if the pegmatite was related to a granite (Breaks *et al.,* 2003). But, in the case of the Tangen pegmatite it is proposed that this might be a function of the fractionation of the pegmatite melt and a crystallization of a melt with a smaller mafic component in comparison to some of the other investigated tourmalines.

The Dalane schorl displays a composition close to foitite due to its high X-vac and Al in the X-site, and low concentrations of Na, Ca and K (Figure 8-11). The tourmalines have high Al, Nb, relatively high Zn, La, Ce and Nd, and low Ti, Cr, Co, V, Ni, Sr, Y, Zr and Ba in comparison with the other tourmalines. The Dalane tourmaline differs from the Lindvikskollen pegmatite mainly in the concentrations of Ti, Cr, Co, V and Sr. This difference in their trace element signature is related to the pegmatite melt, which in the Dalane pegmatite might have originated from the partial melting of rocks richer in felsic minerals (gneiss) relative to the Lindvikskollen melt, rather than being a highly fractionated pegmatite melt like Tangen. This is also confirmed by their classification as a primitive pegmatite with low Mg+Ti+Ca (apfu) content (Figure 9-4). The high Al content could indicate a late-stage tourmaline.

The Havredal pegmatite hosts the only dravitic tourmaline out of the investigated Kragerø pegmatites. The host rocks of this pegmatite are migmatitic gneiss, amphibolite and metagabbro. The mafic host rocks are rich in apatite-enstatite-phlogopite veins. The high Mg, Cr, Ni, V, Sc, and P in the tourmalines of the Havredal pegmatite is possibly a result of the partial melting of these host rocks, which are rich in these elements. The Havredal dravite has low to very low concentrations of Fe, Mn, Sn, Zn, Li, and commonly incompatible elements such as Y, Nb, Ta, Zr, Cs, Rb, W, Th and U. Consequently, this pegmatite has the characteristics of a primitive pegmatite-forming melt, supported by their low Li+Mn (apfu) plotted in Figure 9-4.

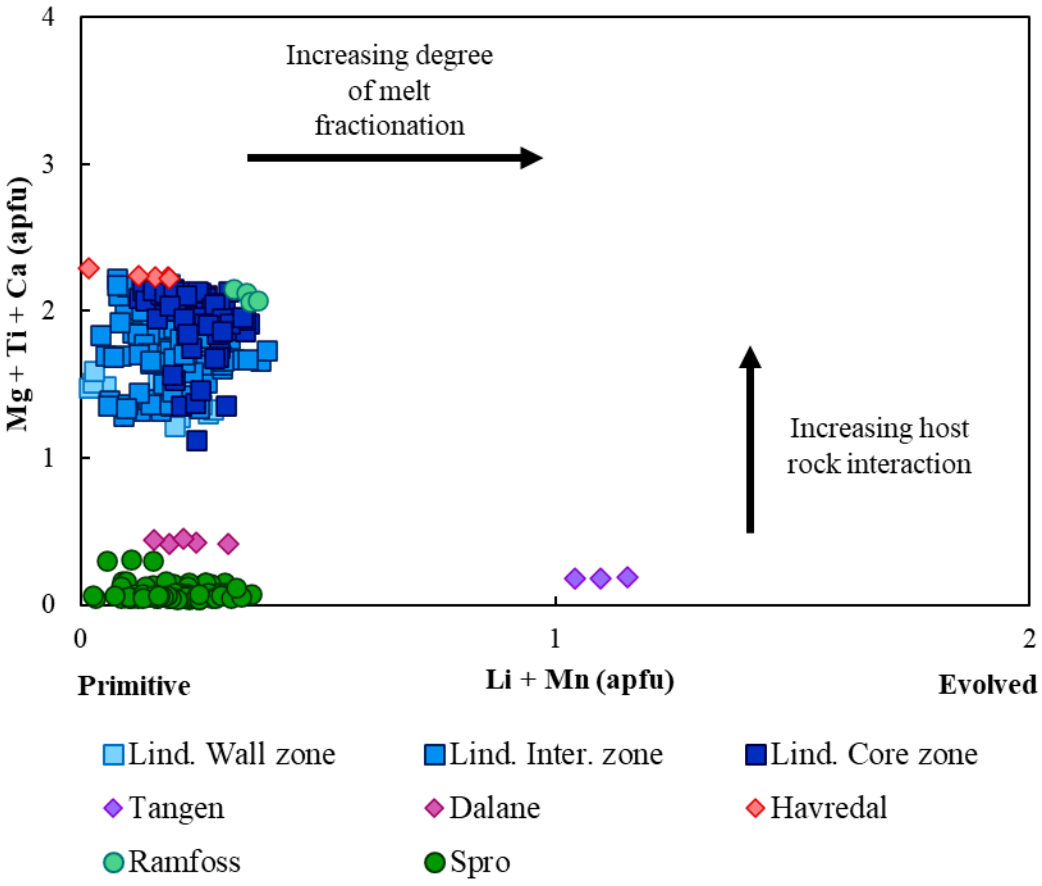

Figure 9-4 - Total Li+Mn vs Mg+Ti+Ca (apfu) diagram for tourmaline compositions. The diagram shows the degree of evolution tourmaline-bearing pegmatites in the x-axis (horizontal arrow), and the level of host rock-pegmatite interaction, represented in the y-axis (vertical arrow). This diagram was based only on granite-related pegmatites, thus for the analysed pegmatites that formed from the partial melting of host rocks, the y-axis is interpreted as Ca, Mg and Ti enrichment of the melt source. Modified from Breaks *et al.* (2003). Lind.: Lindvikskollen; Inter.: Intermediate.

9.2.6. Differences between the tourmalines of the Kragerø, Spro and Ramfoss pegmatites.

The tourmalines from Kragerø, Ramfoss and Spro pegmatites all plot in the schorl and dravite fields (Figure 8-11). Their main difference is the variation in the MgO/(FeO+MgO) ratios of all tourmalines, and to some extent their trace element signature, which mostly depends on the pegmatite protolith as discussed above.

The tourmalines of the Ramfoss pegmatite have outstanding high Ca content, as well as high concentrations of Ti, Ni, Sr, and relatively high Cr, V and REE contents (Ce, Pr, Nd and Eu).

Zn, Ga, and Sn are low, and Mn is very low. The high Ti, Ni, Sr and relatively high REE content in the Ramfoss tourmaline is probably caused by the preferential partitioning of these elements into its structure, such as Ni, Sr and REE, rather than in the other minerals. The notably high Ca concentration could be related to the partial melting of rocks with calcite rich veins, which are common in the Ramfoss area lithologies (Munz *et al.*, 1994). The high Ti concentration in the tourmaline could have resulted from a Ti-rich protolith since the pegmatite also hosts titanite. The same could be the cause of the high REE concentrations in the Ramfoss tourmalines: the pegmatite contains allanite-(Ce) indicating elevated REE contents of the pegmatite melts. Eu concentration has been shown to be correlated to increasing Ca content in the tourmaline-forming melt (*e.g.*, Jolliff *et al.*, 1987). Regarding the notable low trace elements content of the tourmalines, Ramfoss primitive pegmatite melt was not enriched in incompatible elements, thus the tourmaline has low concentrations of Ga and Sn. The low concentration of Mn and Zn seems to be related to the tourmaline MgO/(FeO+MgO) ratio: in this study the investigated pegmatitic dravites all have lower Zn (< 15 ppm) and Mn (< 427 ppm) relative to the schorl tourmalines (> 100 ppm and > 1414 ppm). Zn and Mn occupy the Y site in the tourmaline structure, which is preferentially occupied by Fe^{2+} and Mg.

In comparison with the Kragerø pegmatites the Ramfoss pegmatite tourmalines have more similarities to the Havredal tourmalines – both are dravites. In the MgO vs FeO/(FeO+MgO) diagram by Pirajno & Smithies (1992), they both plot in the hydrothermal origin field (field C; Figure 9-3). However, just like the Havredal tourmalines, the Ramfoss dravites also crystallized from a melt evidenced by their paragenesis with other pegmatite-forming minerals. In the Breaks *et al.* (2003) diagram of Figure 9-4, both these pegmatite tourmalines plot in the primitive magmatic field and with strong signature of calcium-magnesium-rich pegmatite protolith.

The Spro tourmalines occur in the late-stage albite zones of the pegmatite, which clearly distinguishes these tourmalines from the Kragerø and Ramfoss pegmatites, where the tourmalines are found in the entirety of their pegmatite bodies. The Spro pegmatite is hosted by an amphibole gneiss and the deformed Spro granite. According to Faria (2019), the Spro pegmatite originated from the partial melting of a buried peraluminous rock with A-type granite like composition relatively rich in B. The tourmalines crystallized simultaneously with green muscovite, fluorite, topaz, beryl, apatite, calcite and microlite group minerals during a late crystallization stage in vein-

to drop-like batches in the semi-solid pegmatite (Faria, 2019). The Spro pegmatite protolith contributed to the high concentrations of Al, Na, F, Li, Be, Cs, Rb, Co, Zr and Zn in the tourmalines. The low concentrations of Mg, Ti, Sc, Sn, Sr, V and REE were caused not only by the protolith chemistry and the pegmatite melt fractionation, but also by the partition of some of these elements into other minerals rather than tourmaline. Sc and Sn, for example, preferably entered mica (*e.g.*, London, 2008; Rosing-Schow *et al.*, 2019; Steffenssen *et al.*, 2019) and microlite group minerals. Strontium entered feldspars, especially Ca-poor feldspars like albite (*e.g.*, Larsen, 2002) as well as microlite group minerals, and REE preferred to enter, for example, fluorite and microlite group minerals.

The Spro tourmaline is more similar to the Tangen tourmaline from the Kragerø pegmatite field, regarding their extremely low Mg/(Mg+Fe) ratios. Yet, in the case of the Tangen tourmaline the low Mg concentration is caused by the general high level of fractionation of the pegmatite melt, while the low Mg content of the Spro tourmaline is probably related to the source of the pegmatite-forming melt. In addition, both the Spro and Tangen tourmalines plot in the purely magmatic origin field of the Pirajno & Smithies (1992) diagram (Figure 9-3). In the Breaks *et al.* (2003) diagram (Figure 9-4), the Spro pegmatite tourmaline has the lowest values of all investigated tourmalines. According to this diagram the Spro pegmatite melt was Ca-, Mg- and Ti-poor. In this diagram, this tourmaline plots in the primitive pegmatite field (Figure 9-4), which is in agreement with Faria's (2019) mica geochemistry results indicating low melt fractionation degree.

9.2.7. Variation of tourmaline chemistry of the Lindvikskollen pegmatite and its host rocks in comparison with the Spro pegmatite and its host rock.

Lindvikskollen and Spro pegmatite tourmalines are both schorls of magmatic origin (Figure 8-11, Figure 9-3). The host rock tourmalines of both pegmatites are classified as dravites (Figure 8-11). The Lindvikskollen metagabbro and albitites dravites were formed by the hydrothermal fluids that derived from the crystallizing pegmatite (Figure 9-3; see subchapter 9.2.3). The Spro gneiss tourmalines also plot in the C field (hydrothermal conditions) of the Pirajno & Smithies (1992) (Figure 9-3). However, the tourmaline of the Spro gneiss is not present near the pegmatite contact (about 20 m away from the pegmatite), which implies that its origin is not related to the hydrothermal fluids that escaped the crystallizing pegmatite. Faria's (2019) geological

setting descriptions of the Spro pegmatite and host rocks, also suggest that the host rock tourmalines do not derive from the pegmatite.

The Lindvikskollen tourmalines show a clear (linear) Na vs Ca trend, suggesting a continuous evolution from the pegmatite schorls to the hydrothermal dravites (Figure 9-5A). In contrast, for the Spro tourmalines this linear trend is less pronounced (Figure 9-5B). The fact that in the Spro pegmatite tourmaline occurs only on the late-stage albite zones, could be, in part, the reason why the Spro tourmalines lack a continuous evolution trend.

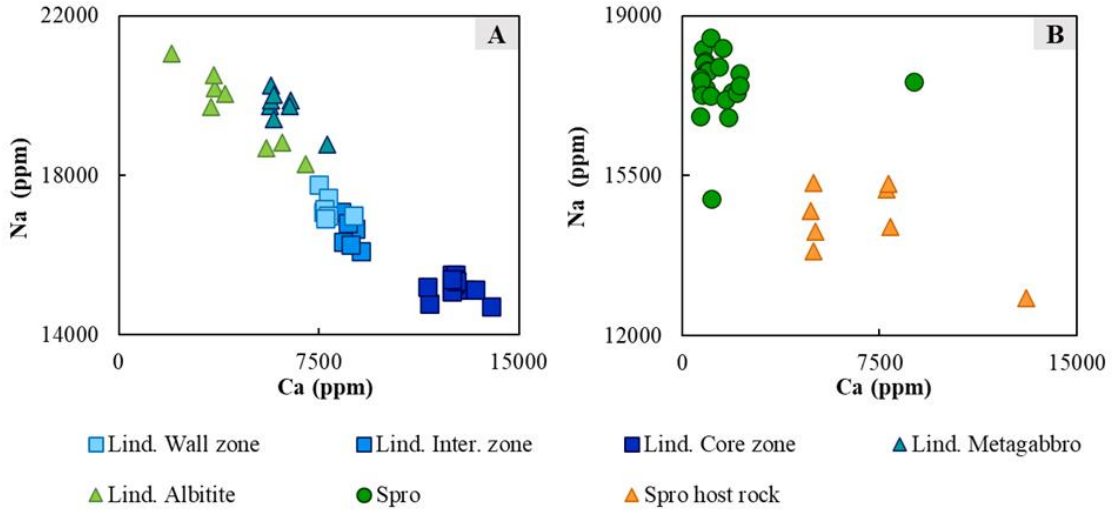

Figure 9-5 - Na vs Ca (ppm) diagram of: **A:** Lindvikskollen tourmalines from the pegmatite and host rocks. **B:** Spro tourmalines from the pegmatite and the host rock. The Lindvikskollen tourmalines show a clear (linear) trend, suggesting a continuous evolution from the pegmatite schorls to the hydrothermal dravites. The Spro tourmalines lack the same clear evolution trend. Lind.: Lindvikskollen; Inter.: Intermediate.

9.3. Genetic implications of the boron isotopic signature of tourmalines

In this study we determined boron isotopes of tourmalines from the Kragerø pegmatites at Lindvikskollen, Tangen, Dalane and Havredal, and the Ramfoss pegmatite of the Kongsberg Sector and the Spro pegmatite of the Idefjorden 'Terrane'.

The tourmaline $\delta^{11}B$ data from four Kragerø pegmatite localities have a narrow range from -1.9 to +2.4‰ (Figure 9-6; Table 8-5). The isotope signatures of individual tourmalines are consistent. This implies that no boron isotope fractionation occurred within the pegmatite melt.

The Lindvikskollen and Tangen pegmatites host tourmalines with overlapping $\delta^{11}B$ values: -1.9 to -1.0 ‰ and -1.4 to -1.0 ‰ $\delta^{11}B$, respectively. Bast *et al.* (2014) investigated various tourmalines from the Bamble Sector, including tourmalines from the Lindvikskollen area. The authors analysed the B isotopes of tourmalines hosted by: albitite (Li-4 and Li-6), a sericitized part of the metagabbro (Li-5) and the pegmatite (Li-8); these samples are presented in the $\delta^{11}B$ diagram of Figure 9-6. The $\delta^{11}B$ data of sample Li-5 (-3.1 to -1.9 ‰) and the analysed Lindvikskollen pegmatite tourmaline overlap slightly. Apart from this, the tourmalines of the Lindvikskollen and Tangen pegmatites investigated in this thesis do not overlap with the data published by Bast *et al.* (2014).

The analysed tourmalines show distinct minor B isotope signature variations among the pegmatite localities. Reiterating, pegmatites from the Lindvikskollen area (Lindvikskollen and Tangen) contain tourmaline with -1.9 to -1.0 ‰ $\delta^{11}B$ and those from Dalane and Havredal have +0.6 to +1.0 ‰ and +1.8 to +2.4 ‰, respectively. These distinct isotopic compositions seem to depend on local variations in the mixed metasedimentary and meta-igneous components from which the pegmatite melts were sourced. The Lindvikskollen and Tangen pegmatites are located near the contact between metagabbro, albitites and banded paragneisses, which could explain the lighter isotopic composition compared to the Dalane and Havredal samples, which intruded metasediments. These results indicate that the pegmatites have different local melt sources even though they occur only a few kilometres apart. It is concluded that the melts formed more likely by local partial melting rather than derivation from a large, buried parental granite pluton.

The tourmalines from the Ramfoss pegmatite of the Kongsberg sector display very different B isotope signature, that range from +9.5 to +9.9 ‰ $\delta^{11}B$. These values reflect a different lithological host of the Ramfoss pegmatite. The Ramfoss data are very different to the common granite and pegmatite isotope ratios suggested by van Hinsberg *et al.* (2011a; and references therein) and presented in Figure 9-6. The Ramfoss data slightly overlap the B isotope ratios of carbonates (Figure 9-6). However, no carbonate rocks occur in the vicinity of the Ramfoss pegmatite according to the local geological map (Viola *et al.*, 2016). The host rocks are quartzite, amphibolite (~2 km away), metagabbro (~1.2 km away) granitic gneisses and metagranodiorites. Nevertheless, the data strongly suggest that carbonates contributed to the pegmatite melt formation. Munz *et al.* (1994) postulated that the Modum Complex was infiltrated by calcareous

fluids based on the common occurrence of calcite rich veins associated with metagabbros. According to the study, the calcite veins might be post- to late-Sveconorwegian (min. 1080 Ma) in age. They concluded that these fluids derived from a crustal reservoir. Considering the crystallisation age of the Ramfoss pegmatite(1045 ± 12 Ma; Andersen & Grorud, 1998), the fluids (carbonate source) were present prior to pegmatite formation.

The isotope signatures of the Spro tourmalines are again very different to the Kragerø and Ramfoss tourmalines, ranging from -13.8 to -12.5‰. They are in fact the only data, which overlap with the common granite-pegmatite ratios. The B ratios are very consistent within the pegmatite body, but also with the ratios of its host rock tourmaline, -14.8 to -12.9 ‰. This implies that the host rock and pegmatite tourmalines are genetically linked. However, the geological settings described by Faria (2019) propose that the host rock tourmalines are not derived from the pegmatite. It is most likely that the tourmalines are originally part of the gneiss host rock. Therefore, it is suggested that the Spro gneissic tourmalines are the B source of the tourmalines found in the pegmatite.

Comparing the B isotopic signature of the investigated pegmatitic tourmalines with published data from other magmatic and pegmatitic tourmalines very few cases had similar $\delta^{11}B$ values determined in this study.

Sunde *et al.* (2020) researched the B isotope composition of coexisting tourmaline and hambergite in alkaline and granitic pegmatites. The authors analysed the $\delta^{11}B$ of tourmaline of peraluminous granite-pegmatites, namely Malkhan pegmatite of Russia, the Fantaziya and Dorozhnaya pegmatites of Tajistan, and the Bulachi pegmatite of Pakistan. These tourmalines yielded light boron ratios, between -12.9 to -4.5‰, overlapping with the common granite-pegmatite ratios (Figure 9-6). The authors conclude that this large range of $\delta^{11}B$ values from the pegmatite tourmalines results from their individual origin history. From the investigated tourmalines, the Spro pegmatite tourmaline $\delta^{11}B$ values overlap with Sunde's *et al.* (2020) data from the Bulachi pegmatite tourmalines (-12.9 to -12‰). This similarity demonstrates that the $\delta^{11}B$ values of tourmalines are related to the source of the pegmatite melt. The Spro pegmatite was formed by shear-zoned-induced partial melting of a peraluminous granitic rock (Faria, 2019) while the Bulachi pegmatite is related to a granite gneiss.

Trumbull *et al.* (2013) determined the tourmaline B isotope compositions from four rare-element pegmatites and one barren pegmatite in the Borborema Province of Brazil, ranging from -20.2 to +1.6‰ $\delta^{11}B$. Around 80% of their analysed tourmalines fall in the "main range" between -17 and -9‰ $\delta^{11}B$ (Figure 9-6). In addition, the authors analysed the black tourmalines from a parental leucogranite, -15.1 to -13.4‰ $\delta^{11}B$. The rare-element Borborema pegmatites display a classic tourmaline zoning, with a composition evolution from the outer to the inner zones of the pegmatite, from schorl-dravite to varicoloured elbaite. Black tourmaline at the barren Fazenda Turmalina pegmatite occurs in all parts of the unzoned pegmatite body. The tourmaline from the wall zone of this pegmatite displays the heaviest $\delta^{11}B$ values of all the Borborema tourmalines investigated by Trumbull *et al.* (2013), from -6.0 to +1.6‰. Nevertheless, the authors did not find a correlation between the B isotope ratios and chemical composition of tourmaline, nor any consistent trend between the B isotope signature and the internal zonation of the crystals, nor any connection related to their occurrence within the pegmatite body and the B isotope composition. Trumbull *et al.* (2013) attribute the heavy B isotope composition, found in the outer zones of the pegmatite, to the interaction with heavy B from the country rocks; in the case of the Borborema Province, marble and calc-silicate rocks. The authors suggest that the influencing factors of B isotope signature vary locally and seem to be specific to each pegmatite and pegmatite zone within it. This statement is in agreement with the hypothesis suggested on this thesis that the B isotope signatures of the investigated pegmatitic tourmalines are related to the local source melt that formed the pegmatites.

Comparing the tourmaline B isotope ratios of the investigated pegmatites with the ones from Trumbull *et al.* (2013) study: the $\delta^{11}B$ values of the tourmalines from Lindvikskollen, Tangen and Dalane pegmatites overlap with the $\delta^{11}B$ of the Fazenda Turmalina pegmatite tourmalines. The B ratios of the Spro pegmatite and host rock tourmalines have similar values to the average "main range" of the Borborema tourmalines and its parental leucogranite. Whereas Ramfoss and Havredal display heavier $\delta^{11}B$ values than the Borborema tourmalines.

Boron isotope signatures are not significantly affected by the partial melting of rocks (Trumbull & Slack, 2018). Several studies have supported this statement, and will be briefly explained further: (1) Kasemann *et al.* (2000) analysed the migmatitic tourmalines, from leucosomes and melanosomes, and the local S-type granites, from NW Argentina. Their

tourmalines B isotope compositions showed no substantial difference between them. (2) The $\delta^{11}B$ values of tourmalines from a S-type granite from Namibia and its melt source, 'tourmalinite'-bearing metapelites, show that B isotope fractionation during melting is negligible (Trumbull *et al.*, 2008). (3) Macgregor *et al.* (2013), published overlapping $\delta^{11}B$ data from tourmaline-bearing paragneiss and anatectic pegmatites in Larsemann Hills, Antarctica. Maner & London (2017) analysed the B isotopic evolution of tourmaline, mica, hambergite, danburite and axinite from the Little Three granite-pegmatites (California, USA). (4) The Little Three granite-pegmatites are hosted by mafic tonalites of the Ramona Complex. $\delta^{11}B$ values of the Little Three pegmatites are higher, -0.1 to +13.8‰ (Figure 9-6), than other pegmatitic tourmaline referenced by the authors (-27 to +9‰; *e.g.*, Palmer & Swihart, 1996; Xiao *et al.*, 2013). They suggest that the heavier B composition of these tourmalines was inherited from an ^{11}B-enriched source, possibly altered oceanic crust. The authors base this hypothesis in the fact that the more probable source of melt of these pegmatites are leucogranitic plutons formed by anatexis in the deep-crust or mantle wedge associated with an influx of water from an underlying oceanic slab. Thus, assuming that B is not lost nor B isotopic fractionation occurs during the whole pegmatite forming process, from melt source to emplacement to crystallization, then the B isotope composition of the pegmatites would be similar to that of the oceanic crust. Their results overlap with the $\delta^{11}B$ values of the Dalane, Havredal and Ramfoss pegmatitic tourmalines. In summary, B isotope data is a useful tool for the study of melt source provenance since B isotope compositions are negligibly affected by the partial melting process.

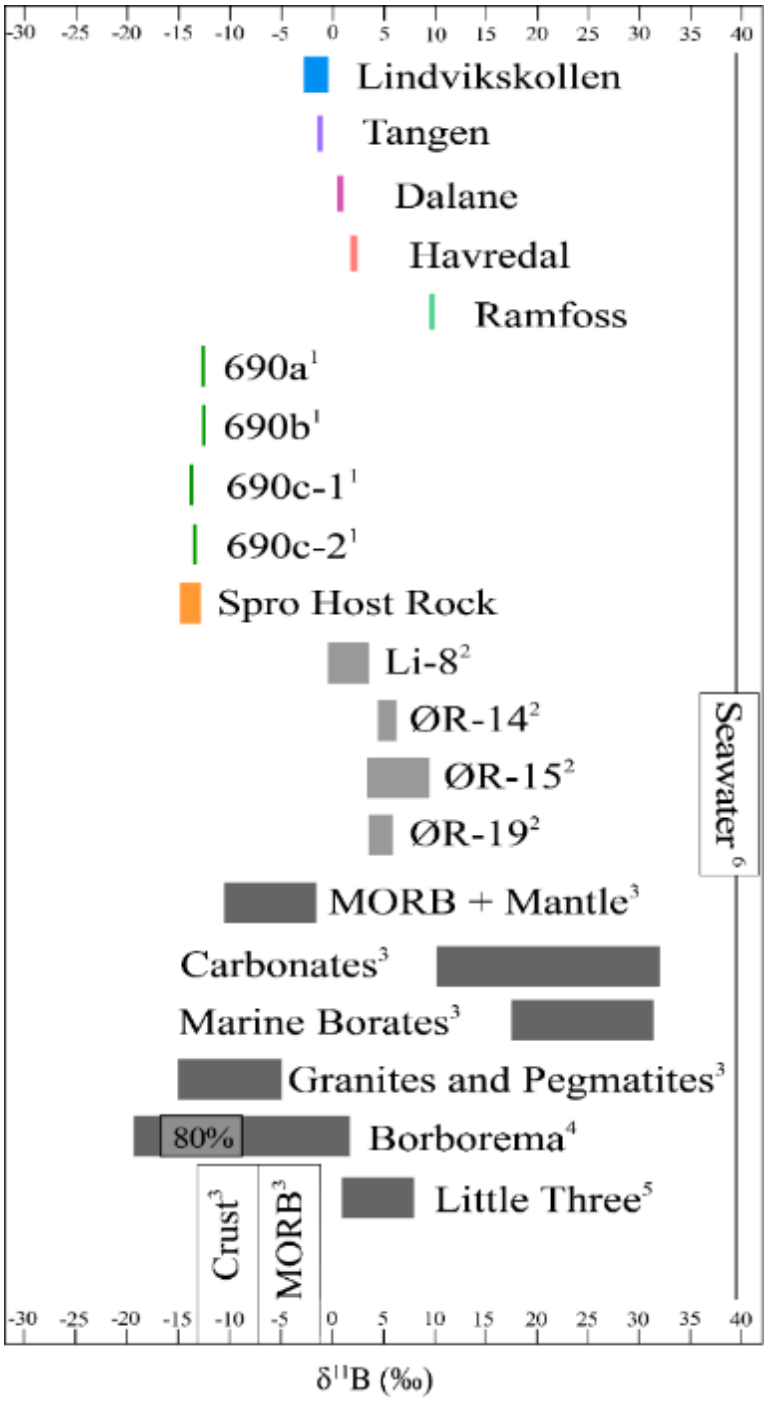

Figure 9-6 - $\delta^{11}B$ value ranges of analysed tourmalines (in colours). To compare results, other $\delta^{11}B$ data of tourmalines from other studies are presented, as well as the $\delta^{11}B$ values of felsic rocks and terrestrial B reservoirs. $\delta^{11}B$ data: [1] Tourmalines of the Spro pegmatite (Faria, 2019). [2] Tourmalines from the Lindvikskollen pegmatite (Li-8) and the Ødegården-Ringsjø albitized rocks (ØR-14, ØR-15, ØR-19) (Bast *et al.*, 2014). [3] B reservoirs (van Hinsberg *et al.*, 2011a) and references therein. [4] Tourmalines from the Borborema pegmatites (Brazil), the inner rectangle represents the "main range" (80%) of the data (Trumbull *et al.*, 2013). [5] Tourmaline from the Little Three pegmatites, USA (Maner & London, 2017). [6] Seawater (Foster *et al.*, 2010).

10. Conclusions

Tourmaline rarely occurs in NYF pegmatites (London, 2008). Yet, in the central Sveconorwegian Pegmatite Province tourmaline is a common mineral in some pegmatites with NYF-affinity (Müller *et al.*, 2017). Tourmaline's chemical complexity and outstanding stability range makes it a great indicator of its host environment. Furthermore, tourmaline's trace elements and B isotope composition provides information about the source of pegmatite melts. Thus, this thesis main objective was to better understand the source of B of the investigated tourmaline-bearing pegmatites using their tourmaline chemistry.

The following pegmatites and their tourmalines were analysed: The Kragerø pegmatites, which include the Lindvikskollen, Tangen, Dalane and Havredal pegmatites of the Bamble Sector; the Ramfoss pegmatite of the Kongsberg Sector and the Spro pegmatite of the Idefjorden 'Terrane'. Because no exposed granite plutons, with similar ages to the pegmatites, are found close to the investigated pegmatites (Müller *et al.*, 2017; Rosing-Schow *et al.*, 2021), the conventional pegmatite genesis model is not suitable to explain the origin of these pegmatites. Thus, it is suggested that these pegmatites were formed by local partial melting.

This thesis had a strong focus on the Lindvikskollen pegmatite. This pegmatite (~500 m in length) intrudes the metagabbro host rock and is characterized by a non-concentric structure of its zones, and multiple cores. Schorl tourmaline occurs in all the pegmatite zones with relative consistent chemistry. This implies that the pegmatite melt was sufficiently rich in Fe, Mg and B to form several generations of schorl in the different pegmatite zones, with crystal length of up to 20 cm. This distribution is uncommon compared to other pegmatites worldwide, where tourmaline compositions evolve drastically from the outer to the inner zones (*e.g.*, Mt. Mica pegmatite; Simmons *et al.*, 2016). The bulk chemistry of the Lindvikskollen pegmatite wall zone determined its A-type affinity, which confirms its mineralogical NYF characteristics. The Lindvikskollen area rocks all have a relatively similar element distribution pattern, implying that somehow these rocks are all genetically linked. Thus, a few candidates for the origin of the Lindvikskollen pegmatite melt were considered. The tourmaline-bearing granite dyke is more fractionated than the pegmatite, therefore it could not have been the pegmatite melt source. Although, the pegmatite shares some similarities with the monzonitic gneiss, its REE pattern and lower Sr content makes it a less likely candidate than the metagabbro. In general, the metagabbro and albitites have a

similar element distribution pattern as the pegmatite. In addition, the B content found in the albitites is enough to produce tourmaline by the partial melting of these rocks. It is important to note that a non-exposed rock might be the melt source of the pegmatite. However, from the rocks analysed in this thesis the most likely candidate for the melt source of the Lindvikskollen pegmatite is the mixed partial melting of metagabbro and albitite.

The geochemistry of the Lindvikskollen pegmatite schorls and host rocks dravites suggest that the pegmatitic tourmalines have a magmatic origin, while the dravites were formed by the hydrothermal fluids that escaped the crystallizing pegmatite and infiltrated the surrounding host rocks. This statement is also supported by the occurrence of tourmaline in the metagabbro and albitite close to the pegmatite contact (< 10 m), and nowhere else.

From tourmaline geochemistry and B isotope analysis it is obvious that tourmaline composition, and subsequently pegmatite composition, highly depend on the melt source. This is clearly seen in the Kragerø pegmatites. These pegmatites occur a few kilometres apart, but still their tourmaline compositions show key differences that hint to separate melt sources. The tourmaline chemistry and the overlapping B isotopes of the Lindvikskollen and Tangen pegmatites suggest they share the same melt source but have different fractionation degrees: Lindvikskollen is poorly fractionated while Tangen is highly fractionated. The higher $\delta^{11}B$ values of the Dalane and Havredal pegmatites are possibly the result of partial melting of metasediments. The Dalane pegmatite tourmaline chemistry points to the gneissic and amphibolitic host rock suite to be its melt source. The melt source of the Havredal pegmatite is most likely the amphibolitic host rocks since its tourmaline is rich in P and the host rocks are mineralized in apatite.

Comparing with the Kragerø pegmatite tourmalines, the Ramfoss and Spro pegmatite tourmalines are very different in their trace element and B isotope geochemistry. The $\delta^{11}B$ values of the Ramfoss pegmatite tourmaline shows affinity with B isotope signatures of carbonates, which occur in the form of calcite veins in the rocks of the Modum Complex. The Spro pegmatite only contains tourmalines in its late-stage albite zone, differentiating it from the other investigated pegmatites. Its tourmalines $\delta^{11}B$ values overlap with the host rock gneiss tourmalines. Considering the B isotopic composition and the previous studies by Faria (2019) of the Spro rocks and minerals, it is suggested that the partial melting of the tourmaline-bearing gneiss is the B source of the Spro pegmatite.

Considering that partial melting negligibly affects B isotope signatures (Trumbull & Slack, 2018), and that the trace elements and B isotope compositions of the investigated tourmalines are highly related to the pegmatite-forming melts, which vary locally and are specific for each pegmatite, it is concluded that the source of B of the investigated pegmatites is the result of:

(1) Low degree partial melting of their respective host rocks that contain B-bearing minerals, such as tourmaline, other borosilicates, and/or micas.

(2) Fractional crystallization of the melts, where the low H_2O activity, high fO_2 and melt composition (low F content), increases the stability range of tourmaline, and allows for its crystallization.

Further studies for the Lindvikskollen pegmatite could focus on the geochemical analysis of feldspar and micas in order to obtain a full understanding of the formation of this pegmatite, as well as more thorough study of the monzonitic gneiss as to confidently exclude it as the melt source of the pegmatite. Also, more geochemical analyses of the Tangen pegmatite could corroborate if its melt source is the same as the Lindvikskollen pegmatite. Additional geochemical and B isotope analysis of the other pegmatites and their host rocks would improve the current understanding of the origin of B, and subsequently of tourmaline, in the NYF Sveconorwegian pegmatites.

11. References

Actlabs. 2021. *Lithogeochemistry and whole rock analysis* [Online]. Ontario, Canada. [Accessed 28.05.2021].

Åhäll, K.-I. & Connelly, J. N. 2008. Long-term convergence along SW fennoscandia: 330 M. Y. of proterozoic crustal growth. *Precambrian Research,* 161**,** 452-474.

Åhäll, K.-I. & Larson, S. Å. 2000. Growth-related 1.85–1.55 Ga magmatism in the Baltic Shield; a review addressing the tectonic characteristics of Svecofennian, TIB 1-related, and Gothian events. *GFF,* 122**,** 193-206.

Ahlin, S., Hegardt, E. A. & Cornell, D. 2006. Nature and stratigraphic position of the 1614 Ma Delsjön augen granite-gneiss in the Median Segment of south-west Sweden. *GFF,* 128**,** 21-32.

Akizuki, M., Kuribayashi, T., Nagase, T. & Kitakaze, A. 2001. Triclinic liddicoatite and elbaite in growth sectors of tourmaline from Madagascar. *American Mineralogist,* 86**,** 364-369.

Åmli, R. 1975. Mineralogy and rare earth geochemistry of apatite and xenotime from the Gloserheia granite pegmatite, Froland, southern Norway. *American Mineralogist,* 60**,** 607-620.

Åmli, R. 1977. Internal structure and mineralogy of the Gloserheia granite pegmatite, Froland, southern Norway. *Norsk Geologisk Tiddsskrift,* 57**,** 243 - 262.

Anders, E. & Grevesse, N. 1989. Abundances of the elements: Meteoritic and solar. *Geochimica et Cosmochimica Acta,* 53**,** 197-214.

Andersen, T. 1997. Radiogenic isotope systematics of the Herefoss granite, South Norway: an indicator of Sveconorwegian (Grenvillian) crustal evolution in the Baltic Shield. *Chemical Geology,* 135**,** 139-158.

Andersen, T. 2005. Terrane analysis, regional nomenclature and crustal evolution in the Southwest Scandinavian Domain of the Fennoscandian Shield. *GFF,* 127**,** 159-168.

Andersen, T., Andresen, A. & Sylvester, A. G. 2001. Nature and distribution of deep crustal reservoirs in the southwestern part of the Baltic Shield: Evidence from Nd, Sr and Pb isotope data on late Sveconorwegian granites. *Journal of the Geological Society,* 158**,** 253-267.

Andersen, T., Graham, S. & Sylvester, A. G. 2009. The geochemistry, Llu-hf isotope systematics, and petrogenesis of late mesoproterozoic A-Type granites in southwestern fennoscandia. *Canadian Mineralogist* 47**,** 1399-1422.

Andersen, T., Griffin, W. L., Jackson, S. E., Knudsen, T. L. & Pearson, N. J. 2004. Mid-Proterozoic magmatic arc evolution at the southwest margin of the Baltic Shield. *Lithos,* 73**,** 289-318.

Andersen, T., Griffin, W. L. & Pearson, N. J. 2002. Crustal Evolution in the SW Part of the Baltic Shield: the Hf Isotope Evidence. *Journal of Petrology,* 43**,** 1725-1747.

Andersen, T. & Grorud, H.-F. 1998. Age and lead isotope systematics of uranium-enriched cobalt mineralization in the Modum complex, south Norway: implications for Precambrian crustal evolution in the SW part of the Baltic Shield. *Precambrian Research,* 91**,** 419-432.

Andersen, T., Hagelia, P. & Whitehouse, M. J. 1994. Precambrian multi-stage crustal evolution in the Bamble sector of south Norway: Pb isotopic evidence from a Sveconorwegian deep-seated granitic intrusion. *Chemical Geology,* 116**,** 327-343.

Andersen, T., Sylvester, A. G. & Graham, S. 2007. Timing and tectonic significance of Sveconorwegian A-type granitic magmatism in Telemark, southern Norway: New results from laser-ablation ICPMS U-Pb dating of zircon.

Andersson, J., Möller, C. & Johansson, L. 2002. Zircon geochronology of migmatite gneisses along the Mylonite Zone (S Sweden): a major Sveconorwegian terrane boundary in the Baltic Shield. *Precambrian Research,* 114**,** 121-147.

Andersson, M., Lie, J. & Husebye, E. 1996. Tectonic setting of post-orogenic granites within SW Fennoscandia based on deep seismic and gravity data. *Terra Nova,* 8**,** 558-566.

Anthony, J. W., Bideaux, R. A., Bladh, K. W. & Nichols, M. C. 1995. *II. Silica, Silicates,* Tucson, Arizona, Mineral Data Publishing.

Austrheim, H., Putnis, C. V., Engvik, A. K. & Putnis, A. 2008. Zircon coronas around Fe–Ti oxides: a physical reference frame for metamorphic and metasomatic reactions. *Contributions to Mineralogy and Petrology,* 156**,** 517-527.

Balen, D. & Petrinec, Z. 2011. Contrasting tourmaline types from peraluminous granites: a case study from Moslavačka Gora (Croatia). *Mineralogy and Petrology,* 102**,** 117-134.

Barth, S. 1993. Boron isotope variations in nature: a synthesis. *Geologische Rundschau,* 82**,** 640-651.

Bast, R., Scherer, E. E., Mezger, K., Austrheim, H., Ludwig, T., Marschall, H. R., Putnis, A. & Löwen, K. 2014. Boron isotopes in tourmaline as a tracer of metasomatic processes in the Bamble sector of Southern Norway. *Contributions to Mineralogy and Petrology,* 168.

Benard, F., Moutou, P. & Pichavant, M. 1985. Phase Relations of Tourmaline Leucogranites and the Significance of Tourmaline in Silicic Magmas. *The Journal of Geology,* 93**,** 271-291.

Beurlen, H., De Moura, O. J., Soares, D. R., Da Silva, M. R. & Rhede, D. 2011. Geochemical and geological controls on the genesis of gem-quality "Paraíba Tourmaline" in granitic pegmatites from northeastern Brazil. *The Canadian Mineralogist,* 49**,** 277-300.

Bingen, B., Andersson, J., Söderlund, U. & Möller, C. 2008a. The Mesoproterozoic in the Nordic countries. *Episodes,* 31.

Bingen, B., Birkeland, A., Nordgulen, Ø. & Sigmond, E. M. O. 2001. Correlation of supracrustal sequences and origin of terranes in the Sveconorwegian orogen of SW Scandinavia: SIMS data on zircon in clastic metasediments. *Precambrian Research,* 108**,** 293-318.

Bingen, B., Davis, W., Hamilton, M., Engvik, A., Stein, H., Skår, Ø. & Nordgulen, O. 2008b. Geochronology of high-grade metamorphism in the Sveconorwegian belt, S. Norway: U-Pb, Th-Pb and Re-Os data. *Norsk Geologisk Tidsskrift,* 88**,** 13-42.

Bingen, B., Nordgulen, O. & Viola, G. 2008c. A four-phase model for the Sveconorwegian orogeny, SW Scandinavia. *Norsk Geologisk Tidsskrift,* 88**,** 43-72.

Bingen, B., Skår, Ø., Marker, Sigmond, Nordgulen, Ragnhildsveit, Mansfeld, J., Tucker, R. & Liégeois, J. P. 2005. Timing of continental building in the Sveconorwegian orogen, SW Scandinavia. *Norsk Geologisk Tiddsskrift,* 85**,** 87-116.

Bingen, B. & Viola, G. 2018. The early-Sveconorwegian orogeny in southern Norway: Tectonic model involving delamination of the sub-continental lithospheric mantle. *Precambrian Research,* 313**,** 170-204.

Bjorlykke, H. 1935. The mineral paragenesis and classification of the granite pegmatites of Iveland, Setesdal, southern Norway. Norsk Geol. Tidsskrift.

Bjørlykke, H. 1937. The granite pegmatites of southern Norway. *American Mineralogist: Journal of Earth and Planetary Materials,* 22**,** 241-255.

Blereau, E., Johnson, T., Clark, C., Taylor, R., Kinny, P. & Hand, M. 2016. Reappraising the P–T evolution of the Rogaland–Vest Agder Sector, southwestern Norway. *Geoscience Frontiers,* 8**,** 1-14.

Bogdanova, S., Bingen, B., Gorbatschev, R., Kheraskova, T., Kozlov, V. I., Puchkov, V. & Volozh, Y. A. 2008. The East European Craton (Baltica) before and during the assembly of Rodinia. *Precambrian Research,* 160**,** 23-45.

Breaks, F. W., Selway, J. B. & Tindle, A. G. 2003. Fertile peraluminous granites and related rare-element mineralization in pegmatites, Superior Province, northwest and northeast Ontario: Operation Treasure Hunt. *Ontario Geological Survey* 179.

Breiter, K., Vašinová_Galiová, M., Korbelová, Z., Vaňková, M. & Kanický, V. 2015. Abundances of gallium, indium, and thallium in granitoids and their rock-forming minerals: Case study of Bohemian Massif. *Zprávy o geologických výzkumech v roce*.

Brewer, T., Ahall, K. I., Darbyshire, D. P. & Menuge, J. 2002. Geochemistry of late Mesoproterozoic volcanism in southwestern Scandinavia: Implications for Sveconorwegian/Grenvillian plate tectonic models. *Journal of The Geological Society* 159**,** 129-144.

Brewer, T. S., Daly, J. S. & Åhäll, K.-I. 1998. Contrasting magmatic arcs in the Palaeoproterozoic of the south-western Baltic Shield. *Precambrian Research,* 92**,** 297-315.

Brøgger, W. 1903. Über der Hellandit, ein neues Mineral. *Nyt Magazin For Naturvidenska Berne Kristainia,* 41**,** 213-221.

Bugge, A. 1936. *Kongsberg-Bamble Formasjonen*, I kommisjon hos H. Aschehoug & Co.

Bugge, A. 1965. Iakttagelser fra Rektangelbladet Kragerø og Den store Grunnfjellsbreksje.

Bugge, J. a. W. 1943. *Geological and Petrographical Investigations in the Kongsberg-Bamble Formation,* Oslo, I kommisjon hos H. Aschehoug & Company.

Bugge, J. a. W. 1978. Norway. *In:* Bowie, S. H. U., Kvalhein, A. & Haslam, H. W. (eds.) *Mineral deposits of Europe, northwest Europe.* London: Institute Mining Metal Mineral Society of London.

Buriánek, D. & Novák, M. 2007. Compositional evolution and substitutions in disseminated and nodular tourmaline from leucocratic granites: Examples from the Bohemian Massif, Czech Republic. *Lithos,* 95**,** 148-164.

Burns, P. C., Macdonald, D. J. & Hawthorne, F. C. 1994. The crystal chemistry of manganese-bearing elbaite. *The Canadian Mineralogist,* 32**,** 31-41.

Büttner, S. 2005. Deformation-controlled cation diffusion in compositionally zoned tourmaline. *Mineralogical Magazine*

69**,** 471-490.

BüTtner, S. H. & Kasemann, S. A. 2007. Deformation-controlled cation diffusion in tourmaline: A microanalytical study on trace elements and boron isotopes. *American Mineralogist,* 92**,** 1862-1874.

Bybee, G. M., Ashwal, L. D., Shirey, S. B., Horan, M., Mock, T. & Andersen, T. B. 2014. Pyroxene megacrysts in Proterozoic anorthosites: Implications for tectonic setting, magma source and magmatic processes at the Moho. *Earth and Planetary Science Letters,* 389**,** 74-85.

Cady, W. G. 1930. Electroelastic and Pyro-Electric Phenomena. *Proceedings of the Institute of Radio Engineers,* 18**,** 1247-1262.

Cameron, E. N., Jahns, R. H., Mcnair, A. H. & Page, L. R. 1949. Internal structure of granitic pegmatites. *Economic Geology Monograph,* 2**,** 115.

Catanzaro, E. J. 1970. *Boric acid: isotopic and assay standard reference materials,* National Bureau of Standards, Institute for Materials Research.

Cawood, P. A. & Pisarevsky, S. A. 2006. Was Baltica right-way-up or upside-down in the Neoproterozoic? *Journal of the Geological Society,* 163**,** 753.

Černý, P. 1991a. Rare-element granitic pegmatites. Part I: anatomy and internal evolution of pegmatitic deposits. *Geoscience Canada*.

Černý, P. 1991b. Rare-element Granitic Pegmatites. Part II: Regional to Global Environments and Petrogenesis. *Geoscience Canada,* 18**,** 68-81.

Černý, P. & Ercit, T. S. 2005. The classification of granitic pegmatites revisited. *The Canadian Mineralogist,* 43**,** 2005-2026.

Černý, P., London, D. & Novák, M. 2012. Granitic pegmatites as reflections of their sources. *Elements,* 8**,** 289-294.

Chappell, B. W. & White, A. J. 2001. Two contrasting granite types: 25 years later. *Australian journal of earth sciences,* 48**,** 489-499.

Coint, N., Slagstad, T., Roberts, N. M. W., Marker, M., Røhr, T. & Sørensen, B. E. 2015. The Late Mesoproterozoic Sirdal Magmatic Belt, SW Norway: Relationships between magmatism and metamorphism and implications for Sveconorwegian orogenesis. *Precambrian Research,* 265**,** 57-77.

Collins, W., Beams, S., White, A. & Chappell, B. 1982. Nature and origin of A-type granites with particular reference to southeastern Australia. *Contributions to mineralogy and petrology,* 80**,** 189-200.

Condie, K. C. 1997. *Plate tectonics and crustal evolution,* Oxford, Butterworth-Heinemann.

Cosca, Michael a., Mezger, K. & Essene, Eric j. 1998. The Baltica-Laurentia Connection: Sveconorwegian (Grenvillian) Metamorphism, Cooling, and Unroofing in the Bamble Sector, Norway. *The Journal of Geology,* 106**,** 539-552.

Culshaw, N. G., Slagstad, T., Raistrick, M. & Dostal, J. 2013. Geochemical, geochronological and isotopic constraints on the origin of members of the allochthonous Shawanaga and basal Parry Sound domains, Central Gneiss Belt, Grenville Province, Ontario. *Precambrian Research,* 228**,** 131-150.

De Haas, G.-J. L. M., Nijland, T. G., Andersen, T. & Corfu, F. 2002. New constraints on the timing of deposition and metamorphism in the Bamble sector, south Norway: Zircon and titanite U-Pb data from the Nelaug area. *GFF,* 124**,** 73-78.

De Haas, G.-J. L. M., Verschure, R. H. & Maijer, C. 1993. Isotopic constraints on the timing of crustal accretion of the Bamble Sector, Norway, as evidenced by coronitic gabbros. *Precambrian Research,* 64**,** 403-417.

De Haas, G., X, Jan, L. M., Andersen, T. & Vestin, J. 1999. Detrital Zircon Geochronology: New Evidence for an Old Model for Accretion of the Southwest Baltic Shield. *The Journal of Geology,* 107**,** 569-586.

Dietrich, R. V. 1985. *The tourmaline group,* New York, van Nostrand.

Dingwell, D., Romano, C. & Hess, K.-U. 1996. The effect of water on the viscosity of a haplogranitic melt under PTX conditions relevant to silicic volcanism. *Contributions to Mineralogy and Petrology,* 124**,** 19-28.

Drivenes, K., Larsen, R. B., Müller, A., Sørensen, B. E., Wiedenbeck, M. & Raanes, M. P. 2015. Late-magmatic immiscibility during batholith formation: assessment of B isotopes and trace elements in tourmaline from the Land's End granite, SW England. *Contributions to Mineralogy and Petrology,* 169.

Drüppel, K., Elsäßer, L., Brandt, S. & Gerdes, A. 2012. Sveconorwegian Mid-crustal Ultrahigh-temperature Metamorphism in Rogaland, Norway: U–Pb LA-ICP-MS Geochronology and

Pseudosections of Sapphirine Granulites and Associated Paragneisses. *Journal of Petrology,* 54**,** 305-350.

Dutrow, B. L., Foster, C. T. & Henry, D. Tourmaline-rich pseudomorphs in sillimanite zone metapelites: Demarcation of an infiltration front. 1999.

Dutrow, B. L. & Henry, D. J. 2000. Complexy zoned fibrous tourmaline, Cruzeiro Mine, Minas Gerais, Brazil: A record of evolving magmatic and hydrothermal fluids. *The Canadian Mineralogist,* 38**,** 131-143.

Dutrow, B. L. & Henry, D. J. 2011. Tourmaline: A Geologic DVD. *Elements,* 7**,** 301-306.

Dutrow, B. L. & Henry, D. J. 2016. Fibrous Tourmaline: a Sensitive Probe of Fluid Compositions and Petrologic Environments. *The Canadian Mineralogist,* 54**,** 311-335.

Dutrow, B. L. & Henry, D. J. 2018. Tourmaline compositions and textures: reflections of the fluid phase. *Journal of Geosciences,* 63**,** 99-110.

Ebbing, J., Afework, Y., Olesen, O. & Nordgulen, Ø. 2005. Is there evidence for magmatic underplating beneath the Oslo Rift? *Terra Nova,* 17**,** 129-134.

Eby, G. N. 1990. The A-type granitoids: A review of their occurrence and chemical characteristics and speculations on their petrogenesis. *Lithos,* 26**,** 115-134.

Eby, G. N. 1992. Chemical subdivision of the A-type granitoids:Petrogenetic and tectonic implications. *Geology,* 20**,** 641-644.

Echlin, P. 2009. *Handbook of Sample Preparation for Scanning Electron Microscopy and X-Ray Microanalysis,* New York, NY, Springer US : Imprint: Springer.

Elliott, R. B. 1966. The Association of Amphibolite and Albitite, Kragerø, South Norway. *Geological Magazine,* 103**,** 1-7.

Engvik, A., Putnis, A., Fitz Gerald, J. & Austrheim, H. 2008. Albitization of granitic rocks: The mechanism of replacement of oligoclase by albite. *Canadian Mineralogist,* 46**,** 1401-1415.

Engvik, A. K., Golla-Schindler, U., Berndt, J., Austrheim, H. & Putnis, A. 2009. Intragranular replacement of chlorapatite by hydroxy-fluor-apatite during metasomatism. *Lithos,* 112**,** 236-246.

Engvik, A. K., Ihlen, P. M. & Austrheim, H. 2014. Characterisation of Na-metasomatism in the Sveconorwegian Bamble Sector of South Norway. *Geoscience Frontiers,* 5**,** 659-672.

Engvik, A. K., Mezger, K., Wortelkamp, S., Bast, R., Corfu, F., Korneliussen, A., Ihlen, P., Bingen, B. & Austrheim, H. 2011. Metasomatism of gabbro – mineral replacement and

element mobilization during the Sveconorwegian metamorphic event. *Journal of Metamorphic Geology,* 29**,** 399-423.

Engvik, A. K., Taubald, H., Solli, A., Grenne, T. & Austrheim, H. 2018. Dynamic metasomatism: stable isotopes, fluid evolution, and deformation of albitite and scapolite metagabbro (Bamble lithotectonic domain, South Norway). *Geofluids,* 2018.

Ercit, T. S. 2005. REE-Enriched Granitic Pegmatites.

Ercit, T. S., Groat, L. A. & Gault, R. A. 2003. Granitic Pegmatites of the O'Grady Batholith, N.W.T., Canada: A Case Study of the Evolution of the Elbaite subtype of Rare-Element Granitic Pegmatite. *The Canadian Mineralogist,* 41**,** 117-137.

Ertl, A., Hughes, J. M., Prowatke, S., Ludwig, T., Prasad, P. S. R., BrandstäTter, F., KöRner, W., Schuster, R., Pertlik, F. & Marschall, H. 2006. Tetrahedrally coordinated boron in tourmalines from the liddicoatite-elbaite series from Madagascar: Structure, chemistry, and infrared spectroscopic studies. *American Mineralogist,* 91**,** 1847-1856.

Falster, A. U., Simmons, W. B., Webber, K. L. & Boudreaux, A. P. 2018. Mineralogy and Geochemistry of the Erongo Sub-Volcanic Granite-Miarolitic-Pegmatite Complex, Erongo, Namibia. *The Canadian Mineralogist,* 56**,** 425-449.

Faria, P. 2019. *The mineralogy and chemistry of the Spro pegmatite mine, Nesodden, and their genetic implications.* Master's thesis, University of Oslo.

Fenn, P. M. 1986. On the origin of graphic granite. *American Mineralogist,* 71**,** 325-330.

Field, D., Smalley, P. C., Lamb, R. C. & Råheim, A. 1985. Geochemical Evolution of the 1.6 — 1.5 Ga-Old Amphibolite-Granulite Facies Terrain, Bamble Sector, Norway: Dispelling the Myth of Grenvillian High-Grade Reworking. *In:* Tobi, A. C. & Touret, J. L. R. (eds.) *The Deep Proterozoic Crust in the North Atlantic Provinces.* Dordrecht: Springer Netherlands.

Ford, W. E. & Dana, E. S. 1932. *A Textbook of Mineralogy*, Wiley.

Foster, G. L., Pogge Von Strandmann, P. a. E. & Rae, J. W. B. 2010. Boron and magnesium isotopic composition of seawater. *Geochemistry, Geophysics, Geosystems,* 11.

Gao, S., Luo, T.-C., Zhang, B.-R., Zhang, H.-F., Han, Y.-W., Zhao, Z.-D. & Hu, Y.-K. 1998. Chemical composition of the continental crust as revealed by studies in East China. *Geochimica et Cosmochimica Acta,* 62**,** 1959-1975.

Ginsburg, A. I., Timofeyev, I. N. & Feldman, L. G. 1979. *Principles of Geology of the Granitic Pegmatites,* Moscow, USSR, Nedra.

Goodenough, K., Lusty, P., Roberts, N., Key, R. & Garba, A. 2014. Post-collisional Pan-African granitoids and rare metal pegmatites in western Nigeria: Age, petrogenesis, and the 'pegmatite conundrum'. *Lithos,* 200**,** 22-34.

Gorbatschev, R. & Bogdanova, S. 1993. Frontiers in the Baltic Shield. *Precambrian Research,* 64**,** 3-21.

Graham, S., Andersen, T. & De Haas, G.-J. Lu-Hf and U-Pb of zircon from the Jomasknutene Gabbro, Bamble Area, southern Norway *In:* Vuollo, J. & Mertanen, S., eds. 5th International Dyke Conference, 31 July - 3 August 2005, 2005 Rovaniemi, Finland. 17.

Graversen, O. 1984. Geology and structural evolution of the Precambrian rocks of the Oslofjord-Øyeren area, Southeast Norway.

Griffin, W. 2008. GLITTER: data reduction software for laser ablation ICP-MS. *Laser Ablation ICP-MS in the Earth Sciences: Current practices and outstanding issues***,** 308-311.

Harlov, D. E. 2011. Formation of monazite and xenotime inclusions in fluorapatite megacrysts, Gloserheia Granite Pegmatite, Froland, Bamble Sector, southern Norway. *Mineralogy and Petrology,* 102**,** 77.

Harlov, D. E., FöRster, H.-J. R. & Nijland, T. G. 2002. Fluid-induced nucleation of (Y + REE)-phosphate minerals within apatite: Nature and experiment. Part I. Chlorapatite. *American Mineralogist,* 87**,** 245-261.

Hawthorne, F. C. & Henry, D. J. 1999. Classification of the minerals of the tourmaline group. *European Journal of Mineralogy,* 11**,** 201-215.

Heaman, L. M. & Smalley, P. C. 1994. A U-Pb study of the Morkheia Complex and associated gneisses, southern Norway: Implications for disturbed Rb-Sr systems and for the temporal evolution of Mesoproterozoic magmatism in Laurentia. *Geochimica et Cosmochimica Acta,* 58**,** 1899-1911.

Henry, D. & Dutrow, B. 1996. Metamorphic Tourmaline and its petrologic applications. *In:* Grew, E. S. & Anovitz, L. M. (eds.) *Boron: Mineralogy, Petrology and Geochemistry.* Chantilly, Virginia: Mineral Society of America.

Henry, D., Dutrow, B. & Selverstone, J. 2004. Compositional asymmetry in replacement tourmaline—An example from the Tauern Window, Eastern Alps. *American Mineralogist,* 88**,** 1399-1399.

Henry, D. J. & Dutrow, B. L. 2012. Tourmaline at diagenetic to low-grade metamorphic conditions: Its petrologic applicability. *Lithos,* 154**,** 16-32.

Henry, D. J. & Dutrow, B. L. 2018. Tourmaline studies through time: contributions to scientific advancements. *Journal of Geosciences,* 63**,** 77-98.

Henry, D. J., Kirkland, B. L. & Kirkland, D. W. 1999. Sector-zoned tourmaline from the cap rock of a salt dome. *European Journal of Mineralogy,* 11**,** 263-280.

Henry, D. J., NováK, M., Hawthorne, F. C., Ertl, A., Dutrow, B. L., Uher, P. & Pezzotta, F. 2011. Nomenclature of the tourmaline-supergroup minerals. *American Mineralogist,* 96**,** 895-913.

Hoffman, P. F. 1991. Did the Breakout of Laurentia Turn Gondwanaland Inside-Out? *Science,* 252**,** 1409.

Högdahl, K., Andersson, U. B. & Eklund, O. 2004. The transscandinavian Igneous Belt (TIB) in Sweden: A review of its character and evolution. *Special Paper of the Geological Survey of Finland***,** 1-125.

Holtz, F. & Johannes, W. 1991. Effect of tourmaline on melt fraction and composition of first melts in quartzofeldspathic gneiss. *European Journal of Mineralogy,* 3**,** 527-536.

Høy, I. U. Sveconorwegian magmatic and metamorphic evolution of southwestern Norway. 2016.

Hughes, J. M., Rakovan, J., Ertl, A., Rossman, G. R., Baksheev, I. & Bernhardt, H.-J. 2011. Dissymmetrization in tourmaline: the atomic arrangement of sectorally zoned triclinic Ni-bearing dravite. *The Canadian Mineralogist,* 49**,** 29-40.

Jacobsen, S. B. 1975. *Geochronological, Geochemical and petrological investigations of Precambrian rocks in the Kongsberg area.* . Cand. real thesis, University of Oslo.

Jacobsen, S. B. & Heier, K. S. 1978. Rb-Sr isotope systematics in metamorphic rocks, Kongsberg sector, south Norway. *Lithos,* 11**,** 257-276.

Jahns, R. H. 1953. The genesis of pegmatites: I. Occurrence and origin of giant crystals. *American Mineralogist: Journal of Earth and Planetary Materials,* 38**,** 563-598.

Jahns, R. H. 1955. The study of pegmatites. *Econ. Geol.***,** 1025-1130.

Jahns, R. H. & Burnham, C. W. 1969. Experimental studies of pegmatite genesis; l, A model for the derivation and crystallization of granitic pegmatites. *Economic Geology,* 64**,** 843-864.

Jahns, R. H. & Tuttle, O. F. 1963. Layered pegmatite-aplite intrusives. *Mineralogical Society of America Special Paper,* 1**,** 78-92.

Jensen, E. & Corfu, F. 2016. The U–Pb age of the Finse batholith, a composite bimodal Sveconorwegian intrusion. *Norwegian Journal of Geology,* 96.

Jolliff, B. L., Papike, J. J. & Laul, J. C. 1987. Mineral recorders of pegmatite internal evolution: REE contents of tourmaline from the Bob Ingersoll pegmatite, South Dakota. *Geochimica et Cosmochimica Acta,* 51**,** 2225-2232.

Jøsang, O. 1966. Geologiske og petrografiske undersøkelser i Modumfeltet. *Norges Geologiske Undersøkelse Bulletin,* 235**,** 148.

Karlstrom, K. E., Åhäll, K.-I., Harlan, S. S., Williams, M. L., Mclelland, J. & Geissman, J. W. 2001. Long-lived (1.8–1.0 Ga) convergent orogen in southern Laurentia, its extensions to Australia and Baltica, and implications for refining Rodinia. *Precambrian Research,* 111**,** 5-30.

Kasemann, S., Erzinger, J. & Franz, G. 2000. Boron recycling in the continental crust of the central Andes from the Palaeozoic to Mesozoic, NW Argentina. *Contributions to Mineralogy and Petrology,* 140**,** 328-343.

Kawakami, T. 2004. Tourmaline and boron as indicators of the presence, segregation and extraction of melt in pelitic migmatites: Examples from the Ryoke metamorphic belt, SW Japan. *Transactions of the Royal Society of Edinburgh: Earth Sciences,* 95**,** 111-123.

Kawakami, T. & Ikeda, T. 2003. Boron in metapelites controlled by the breakdown of tourmaline and retrograde formation of borosilicates in the Yanai area, Ryoke metamorphic belt, SW Japan. *Contributions to Mineralogy and Petrology,* 145**,** 131-150.

Keller, P., Roda Robles, E., Pesquera Pérez, A. & Fontan, F. 1999. Chemistry, paragenesis and significance of tourmaline in pegmatites of the Southern Tin Belt, central Namibia. *Chemical Geology,* 158**,** 203-225.

Knudsen, T.-L. & Andersen, T. 1999. Petrology and Geochemistry of the Tromøy Gneiss Complex, South Norway, an Alleged Example of Proterozoic Depleted Lower Continental Crust. *Journal of Petrology,* 40**,** 909-933.

Knudsen, T. L., Andersen, T., Whitehouse, M. J. & Vestin, J. 1997. Detrital zircon ages from southern Norway – implications for the Proterozoic evolution of the southwestern Baltic Shield. *Contributions to Mineralogy and Petrology,* 130**,** 47-58.

Kontak, D. J. & Martin, R. F. 1997. Alkali feldspar in the peraluminous South Mountain Batholith, Nova Scotia; trace-element data. *The Canadian Mineralogist,* 35**,** 959-977.

Konzett, J., Schneider, T., Nedyalkova, L., Hauzenberger, C., Melcher, F., Gerdes, A. & Whitehouse, M. 2018. Anatectic Granitic Pegmatites from the Eastern Alps: A Case of Variable Rare-Metal Enrichment During High-Grade Regional Metamorphism–I: Mineral Assemblages, Geochemical Characteristics, and Emplacement Ages. *The Canadian Mineralogist,* 56**,** 555-602.

Krosse, S. 1995. *Hochdrucksynthese, Stabilität und Eigenschaften der Borsilikate Dravit und Kornerupin sowie Darstellung und Stabilitätsverhalten eines neuen Mg-Al-Borates*.

Kullerud, L. & Machado, N. End of a controversy: U–Pb geochronological evidence for significant Grenvillian activity in the Bamble area, Norway. Terra Abstracts, supplement to Terra Nova, 1991. 504.

Lang, S. 2005. Pyroelectricity: From Ancient Curiosity to Modern Imaging Tool. *Physics Today,* 58**,** 31-36.

Lang, S. B. 1974. *Sourcebook of pyroelectricity,* London, New York, Gordon and Breach Science Publishers.

Larsen, R. B. 2002. The Distribution of Rare-Earth Elements in K-Feldspar as an indicator of Petrogenetic Processes in Granitic Pegmatites: Examples from two pegmatite fields in Southern Norway. *The Canadian Mineralogist,* 40**,** 137-152.

Le Maitre, R. W., Streckeisen, A., Zanettin, B., Le Bas, M., Bonin, B. & Bateman, P. 2005. *Igneous rocks: a classification and glossary of terms: recommendations of the International Union of Geological Sciences Subcommission on the Systematics of Igneous Rocks*, Cambridge University Press.

Leeman, W. P. & Sisson, V. B. 1996. Geochemistry of boron and its implications for crustal and mantle processes. *In:* Grew, E. S. & Anovitz, L. M. (eds.) *Boron: Mineralogy, Petrology and Geochemistry.* Chantilly: Mineralogical Soc Amer & Geochemical Soc.

Leeman, W. P. & Tonarini, S. 2001. Boron Isotopic Analysis of Proposed Borosilicate Mineral Reference Samples. *Geostandards Newsletter,* 25**,** 399-403.

Lemarchand, D., Gaillardet, J., Lewin, É. & Allègre, C. J. 2000. The influence of rivers on marine boron isotopes and implications for reconstructing past ocean pH. *Nature,* 408**,** 951-954.

Lieftink, D. J., Nijland, T. G. & Maijer, C. 1994. The behavior of rare-earth elements in high-temperature Cl-bearing aqueous fluids: results from the Ødegårdens Verk natural laboratory. *Canadian Mineralogist,* 32**,** 149 - 158.

Linge, K. L. & Jarvis, K. E. 2009. Quadrupole ICP-MS: Introduction to Instrumentation, Measurement Techniques and Analytical Capabilities. *Geostandards and Geoanalytical Research,* 33**,** 445-467.

London, D. 1989. Lithophile rare element concentration in silicic rocks: The alkaline trend in granitic systems. *Geological and Mineralogical Associations of Canada, Program with Abstracts,* 14**,** A21.

London, D. 1997. Estimating Abundances of Volatile and Other Mobile Components in Evolved Silicic Melts Through Mineral–Melt Equilibria. *Journal of Petrology,* 38**,** 1691-1706.

London, D. 1999. Stability of tourmaline in pei aluminous granite systems: the boron cycle from anatexis to hydrothermal aureoles. *European Journal of Mineralogy***,** 253-262.

London, D. 2008. *Pegmatites,* Ottawa, Mineralogical Association of Canada.

London, D. 2011. Experimental synthesis and stability of tourmaline: a historical overview. *The Canadian Mineralogist,* 49**,** 117-136.

London, D. 2014. A petrologic assessment of internal zonation in granitic pegmatites. *Lithos,* 184**,** 74-104.

London, D. 2016. Reading Pegmatites—Part 2: What Tourmaline Says. *Rocks & Minerals,* 91**,** 132-149.

London, D., Morgan, G. B. & Hervig, R. L. 1989. Vapor-undersaturated experiments with Macusani glass+ H 2 O at 200 MPa, and the internal differentiation of granitic pegmatites. *Contributions to Mineralogy and Petrology,* 102**,** 1-17.

London, D., Morgan, G. B. & Wolf, M. B. 1996. Boron in granitic rocks and their contact aureoles. *Boron - Mineralogy, Petrology and Geochemisty.* De Gruyter, Mineralogical Society of America.

Lussier, A., Ball, N. A., Hawthorne, F. C., Henry, D. J., Shimizu, R., Ogasawara, Y. & Ota, T. 2016. Maruyamaite, $K(MgAl_2)(Al_5Mg)Si_6O_{18}(BO_3)_3(OH)_{3O}$, a potassium-dominant tourmaline from the ultrahigh-pressure Kokchetav massif, northern Kazakhstan: Description and crystal structure. *American Mineralogist,* 101**,** 355.

Macgregor, J., Grew, E. S., De Hoog, J. C. M., Harley, S. L., Kowalski, P. M., Yates, M. G. & Carson, C. J. 2013. Boron isotopic composition of tourmaline, prismatine, and grandidierite from granulite facies paragneisses in the Larsemann Hills, Prydz Bay, East

Antarctica: Evidence for a non-marine evaporite source. *Geochimica et Cosmochimica Acta,* 123**,** 261-283.

Magnusson, N. H. 1960. Age determinations of Swedish Precambrian rocks. *Geologiska Föreningen i Stockholm Förhandlingar,* 82**,** 407-432.

Maner, J. L. & London, D. 2017. The boron isotopic evolution of the Little Three pegmatites, Ramona, CA. *Chemical Geology,* 460**,** 70-83.

Marker, M., Solli, A., Slagstad, T., Bjerkgård, T. & Gjelle, S. 2020. *Berggrunnskart BAMBLE - KRAGERØ, M 1:50 000*. Norges geologiske undersøkelse.

Marschall, H. & Jiang, S.-Y. 2011. Tourmaline Isotopes: No Element Left Behind. *Elements,* 7**,** 313-319.

Marschall, H. R., Korsakov, A. V., Luvizotto, G. L., Nasdala, L. & Ludwig, T. 2009. On the occurrence and boron isotopic composition of tourmaline in (ultra)high-pressure metamorphic rocks. *Journal of the Geological Society,* 166**,** 811-823.

Mcnutt, R. & Dickin, A. 2012. A comparison of Nd model ages and U-Pb zircon ages of Grenville granitoids: Constraints on the evolution of the Laurentian margin from 1.5 to 1.0Ga. *Terra Nova,* 24.

Möller, C. 1998. Decompressed eclogites in the Sveconorwegian (–Grenvillian) orogen of SW Sweden: petrology and tectonic implications. *Journal of Metamorphic Geology,* 16**,** 641-656.

Möller, C., Andersson, J., Dyck, B. & Antal Lundin, I. 2015. Exhumation of an eclogite terrane as a hot migmatitic nappe, Sveconorwegian orogen. *Lithos,* 226**,** 147-168.

Möller, C., Andersson, J., Lundqvist, I. & Hellström, F. 2007. Linking deformation, migmatite formation and zircon U–Pb geochronology in polymetamorphic orthogneisses, Sveconorwegian Province, Sweden. *Journal of Metamorphic Geology,* 25**,** 727-750.

Momma, K. & Izumi, F. 2011. VESTA 3 for three-dimensional visualization of crystal, volumetric and morphology data. *Journal of Applied Crystallography,* 44**,** 1272-1276.

Morgan, G. B. & London, D. 1989. Experimental reactions of amphibolite with boron-bearing aqueous fluids at 200 MPa: implications for tourmaline stability and partial melting in mafic rocks. *Contributions to Mineralogy and Petrology,* 102**,** 281-297.

Morgan, V. I. & London, D. 1987. Alteration of amphibolitic wallrocks around the Tanco rare-element pegmatite, Bernic Lake, Manitoba. *The American mineralogist,* 72**,** 1097-1121.

Morton, R., O'nions, R. & Batey, R. 1970. Geological investigations in the Bamble sector of the Fennoscandian Shield South Norway. I. The geology of eastern Bamble.

Mulch, A. 2004. *Integrated high-spatial resolution 40Ar/39Ar geochronology, stable isotope geochemistry, and structural analysis of extensional detachment systems: case studies from the Porsgrunn-Kristiansand Shear Zone (S-Norway) and the Shuswap Metamorphic Core Complex (Canada).* Université de Lausanne, Faculté des sciences.

Müller, A., Ihlen, P. M., Snook, B., Larsen, R. B., Flem, B., Bingen, B. & Williamson, B. J. 2015. The chemistry of quartz in granitic pegmatites of southern Norway: Petrogenetic and economic implications. *Economic Geology,* 110**,** 1737-1757.

Müller, A., Larsen, R. B., Wanvik, E. E., Friis, H., De La Cruz, E. & Rosing-Schow, N. 2021. Norwegian Pegmatites II: Tørdal, Kragerø, Frolans. *Geological Society of Norway Geological Guides* 2021-8.

Müller, A., Romer, R. & Pedersen, R.-B. 2017. The Sveconorwegian Pegmatite Province – Thousands of Pegmatites Without Parental Granites. *The Canadian Mineralogist,* 55**,** 283-315.

Müller, A., Seltmann, R., Halls, C., Siebel, W., Dulski, P., Jeffries, T., Spratt, J. & Kronz, A. 2006. The magmatic evolution of the Land's End pluton, Cornwall, and associated pre-enrichment of metals. *Ore Geology Reviews,* 28**,** 329-367.

Munz, I. A., Wayne, D. & Austrheim, H. 1994. Retrograde fluid infiltration in the high-grade Modum Complex South Norway: evidence for age, source and REE mobility. *Contributions to Mineralogy and Petrology,* 116**,** 32.

Munz, I. A., Yardley, B. W. D., Banks, D. A. & Wayne, D. 1995. Deep penetration of sedimentary fluids in basement rocks from southern Norway: Evidence from hydrocarbon and brine inclusions in quartz veins. *Geochimica et Cosmochimica Acta,* 59**,** 239-254.

Nabelek, P. I., Russ-Nabelek, C. & Denison, J. 1992a. The generation and crystallization conditions of the Proterozoic Harney Peak leucogranite, Black Hills, South Dakota, USA: petrologic and geochemical constraints. *Contributions to Mineralogy and Petrology,* 110**,** 173-191.

Nabelek, P. I., Russ-Nabelek, C. & Haeussler, G. 1992b. Stable isotope evidence for the petrogenesis and fluid evolution in the Proterozoic Harney Peak leucogranite, Black Hills, South Dakota. *Geochimica et Cosmochimica Acta,* 56**,** 403-417.

Nijland, T. & Touret, J. 2001. Replacement of graphic pegmatite by graphic albite-actinoliteclinopyroxene intergrowths (Mjåvatn, southern Norway). *European Journal of Mineralogy,* 13**,** 41-50.

Nijland, T. G. 1993. *The Bamble amphibolite to granulite facies transitions zone, Norway*. Doctor, Rijksuniversiteit te Utrecht.

Nijland, T. G., Harlov, D. E. & Andersen, T. 2014. The Bamble Sector, South Norway: A review. *Geoscience Frontiers,* 5**,** 635-658.

Nijland, T. G., Liauw, F., Visser, D., Maijer, C. & Senior, A. 1993. Metamorphic petrology of the Froland corundum-bearing rocks: The cooling and uplift history of the Bamble sector, South Norway. *Bull Nor Geol Unders,* 424**,** 51-63.

Nijland, T. G. & Maijer, C. 1993. The regional amphibolite to granulite facies transition at Arendal, Norway. Evidence for a thermal dome. *Neues Jahrbuch für Mineralogie. Abhandlungen,* 165**,** 191-221.

Norton, J. J. 1966. *Ternary diagrams of the quartz-feldspar content of pegmatites in Colorado*, US Government Printing Office.

Norton, J. J. 1983. Sequence of mineral assemblages in differentiated granitic pegmatites. *Economic Geology,* 78**,** 854-874.

Ota, T., Kobayashi, K., Katsura, T. & Nakamura, E. 2008. Tourmaline breakdown in a pelitic system: implications for boron cycling through subduction zones. *Contributions to Mineralogy and Petrology,* 155**,** 19-32.

Palmer, M. R. & Swihart, G. H. 1996. Boron Isotope Geochemistry: An Overview. *In:* Lawrence, M. A. & Edward, S. G. (eds.) *Boron: Mineralogy, Petrology and Geochemistry.* De Gruyter.

Park, R. G., Åhäll, K. I. & Bland, M. P. 1991. The Sveconorwegian shear-zone network of SW Sweden in relation to mid-Proterozoic plate movements. *Precambrian Research,* 49**,** 245-260.

Pauling, L. 1929. The principle determining the structure of complex ionic crystals. *Journal of the American Chemical Society,* 51**,** 101-1026.

Pedersen, S. 1978. Rb/Sr-dating of the plutonic and tectonic evolution of the Sveconorwegian Province, southern Norway.

Pedersen, S., Andersen, T., Konnerup-Madsen, J. & Griffin, W. L. 2009. Recurrent mesoproterozoic continental magmatism in South-Central Norway. *International Journal of Earth Sciences,* 98**,** 1151-1171.

Pirajno, F. & Smithies, R. H. 1992. The FeO/(FeO+MgO) ratio of tourmaline: A useful indicator of spatial variations in granite-related hydrothermal mineral deposits. *Journal of geochemical exploration,* 42**,** 371-381.

Pozer, B. E. 2008. *Age and origin of the Mesoproterozoic basement of the Nesodden Peninsula, SE Norway: A geochronological and isotopic study.* Msc Master Thesis, University of Oslo.

Raade, G. 1965. *The minerals of the granite pegmatite at Spro, Nesodden, near Oslo,* NGU.

Rivers, T. & Corrigan, D. 2000. Convergent margin on southeastern Laurentia during the Mesoproterozoic: Tectonic implications. *Canadian Journal of Earth Sciences,* 37**,** 359-383.

Robbins, C. R. & Yoder, H. S., Jr 1962. Stability relations of dravite, a tourmaline. *Carnegie Institution of Washington***,** 106-108.

Roberts, N. & Slagstad, T. 2015. Continental growth and reworking on the edge of the Columbia and Rodinia supercontinents; 1.86–0.9 Ga accretionary orogeny in southwest Fennoscandia. *International Geology Review,* 57**,** 1582-1606.

Roberts, N. M. W., Parrish, R. R. & Horstwood, M. S. A. 2011. The 1.23 Ga Fjellhovdane rhyolite, Grøssæ-Totak; a new age within the Telemark supracrustals, southern Norway. *Norsk Geologisk Tiddsskrift,* 91**,** 239-246.

Roberts, N. M. W., Slagstad, T., Parrish, R. R., Norry, M. J., Marker, M. & Horstwood, M. S. A. 2013. Sedimentary recycling in arc magmas: geochemical and U–Pb–Hf–O constraints on the Mesoproterozoic Suldal Arc, SW Norway. *Contributions to Mineralogy and Petrology,* 165**,** 507-523.

Roda Robles, E., Pesquera Perez, A., Velasco Roldan, F. & Fontan, F. 1999. The granitic pegmatites of the Fregeneda area (Salamanca, Spain); characteristics and petrogenesis. *Mineralogical Magazine,* 63**,** 535-558.

Rosing-Schow, N., Müller, A., Romer, R. L. & Friis, H. 2019. New age constraints on the formation of Sveconorwegian pegmatites. *The Canadian Mineralogist,* 57**,** 787-790.

Rosing-Schow, N., Romer, R. L., Müller, A., Corfu, F. & Friis, H. 2021. Breaking the paradigm: Orogen-wide, two-stage pegmatite formation by anatexis during the assembly of Rodinia. New insights in the formation of Sveconorwegian pegmatites, southern Norway. *Precambrian Research*.

Rudnick, R. & Gao, S. 2003. Composition of the continental crust. *The crust,* 3**,** 1-64.

Scaillet, B., Pichavant, M. & Roux, J. 1995. Experimental Crystallization of Leucogranite Magmas. *Journal of Petrology,* 36**,** 663-705.

Schauble, E. A. 2004. Applying Stable Isotope Fractionation Theory to New Systems. *Reviews in Mineralogy and Geochemistry,* 55**,** 65-111.

Selway, J., Novák, M. & Hawthorne, F. 2000a. The Tanco pegmatite at Bernic Lake, Manitoba. XIII. Exocontact tourmaline. *The Canadian Mineralogist,* 38**,** 869-876.

Selway, J. B., Cerny, P., Hawthorne, F. C. & Novak, M. 2000b. The Tanco Pegmatite at Bernic Lake, Manitoba. XIV. Internal Tourmaline. *The Canadian Mineralogist,* 38**,** 877-891.

Selway, J. B., Novak, M., Cerny, P. & Hawthorne, F. C. 1999. Compositional evolution of tourmaline in lepidolite-subtype pegmatites. *European Journal of Mineralogy,* 11**,** 569-584.

Shtukenberg, A., Rozhdestvenskaya, I., Frank-Kamenetskaya, O., Bronzova, J., Euler, H., Kirfel, A., Bannova, I. & Zolotarev, A. 2007. Symmetry and crystal structure of biaxial elbaite-liddicoatite tourmaline from the Transbaikalia region, Russia. *American Mineralogist,* 92**,** 675-686.

Simmons, W. B., Falster, A. U., Webber, K., Roda-Robles, E., Boudreaux, A. P., Grassi, L. R. & Freeman, G. 2016. Bulk composition of Mt. Mica Pegmatite, Maine, USA; implications for the origin of an LCT type pegmatite by anatexis. *Canadian mineralogist,* 54**,** 1053-1070.

Simmons, W. B., Freeman, G., Falster, A., Laurs, B. & Webber, K. 2005a. New tourmaline production: From Mount Mica, Maine America's First gem pegmatite. *Rocks & minerals,* 80**,** 396-408.

Simmons, W. B., Laurs, B. M., Falster, A. U., Koivula, J. I. & Webber, K. L. 2005b. Mt. Mica: A Renaissance in Maine's Gem Tourmaline Production. *Gems & Gemology,* 41.

Simmons, W. B. S. & Webber, K. L. 2008. Pegmatite genesis: state of the art. *European Journal of Mineralogy,* 20**,** 421-438.

Skiöld, T. 1976. The interpretation of the Rb-Sr and K-Ar ages of late Precambrian rocks in south-western Sweden. *Geologiska Föreningen i Stockholm Förhandlingar,* 98**,** 3-29.

Slack, J. F. 1996. Tourmaline associations with hydrothermal ore deposits. *Reviews in Mineralogy,* 33**,** 558-643.

Slack, J. F. & Trumbull, R. B. 2011. Tourmaline as a recorder of ore-forming processes. *Elements,* 7**,** 321-326.

Slagstad, T., Marker, M., Roberts, N. M. W., Saalmann, K., Kirkland, C. L., Kulakov, E., Ganerød, M., Røhr, T. S., Møkkelgjerd, S. H. H., Granseth, A. & Sørensen, B. E. 2020. The Sveconorwegian orogeny – Reamalgamation of the fragmented southwestern margin of Fennoscandia. *Precambrian Research,* 350**,** 105877.

Slagstad, T., Roberts, N. M. W. & Kulakov, E. 2017. Linking orogenesis across a supercontinent; the Grenvillian and Sveconorwegian margins on Rodinia. *Gondwana Research,* 44**,** 109-115.

Slagstad, T., Roberts, N. M. W., Marker, M., Røhr, T. S. & Schiellerup, H. 2012. A non-collisional, accretionary Sveconorwegian orogen. *Terra Nova,* 25**,** 30-37.

Söderlund, U., Elming, S.-Å., Ernst, R. E. & Schissel, D. 2006. The Central Scandinavian Dolerite Group—Protracted hotspot activity or back-arc magmatism?: Constraints from U–Pb baddeleyite geochronology and Hf isotopic data. *Precambrian Research,* 150**,** 136-152.

Söderlund, U., Hellström, F. & Kamo, S. 2008. Geochronology of high-pressure mafic granulite dykes in SW Sweden: Tracking the P-T-t path of metamorphism using Hf isotopes in zircon and baddeleyite. *Journal of Metamorphic Geology,* 26**,** 539-560.

Söderlund, U., Isachsen, C. E., Bylund, G., Heaman, L. M., Jonathan Patchett, P., Vervoort, J. D. & Andersson, U. B. 2005. U–Pb baddeleyite ages and Hf, Nd isotope chemistry constraining repeated mafic magmatism in the Fennoscandian Shield from 1.6 to 0.9 Ga. *Contributions to Mineralogy and Petrology,* 150**,** 174.

Söderlund, U., Jarl, L.-G., Persson, P.-O., Stephens, M. B. & Wahlgren, C.-H. 1999. Protolith ages and timing of deformation in the eastern, marginal part of the Sveconorwegian orogen, southwestern Sweden. *Precambrian Research,* 94**,** 29-48.

Söderlund, U., Möller, C., Andersson, J., Johansson, L. & Whitehouse, M. 2002. Zircon geochronology in polymetamorphic gneisses in the Sveconorwegian orogen, SW Sweden:

ion microprobe evidence for 1.46–1.42 and 0.98–0.96 Ga reworking. *Precambrian Research,* 113**,** 193-225.

Sperlich, R., Giere, R. & Frey, M. 1996. Evolution of compositional polarity and zoning in tourmaline during prograde metamorphism of sedimentary rocks in the Swiss Central Alps. *American Mineralogist,* 81**,** 1222-1236.

Spicer, E., Stevens, G. & Buick, I. 2004. The low-pressure partial-melting behaviour of natural boron-bearing metapelites from the Mt. Stafford area, central Australia. *Contributions to Mineralogy and Petrology,* 148**,** 160-179.

Starmer, I. C. 1972. The Sveconorwegian regeneration and earlier orogenic events in the Bamble series, South Norway. *Norges Geologiske Undersokelse,* 277**,** 37-52.

Starmer, I. C. 1985. The evolution of the south Norwegian Proterozoic as revealed by major and mega-tectonics of the Kongsberg and Bamble sectors. *In:* Tobi, A. C. & Touret, J. L. R. (eds.) *The deep Proterozoic crust in the North Atlantic provinces.* Dordrecht: Reidel.

Starmer, I. C. 1987. Geological map of the Bamble Sector, South Norway (1:100,000). *In:* Maijer, C. & Padget, P. (eds.) *The Geology of Southernmost Norway* Norges Geologiske Undersøkelse.

Starmer, I. C. 1996. Accretion, rifting, rotation and collision in the North Atlantic supercontinent, 1700-950 Ma. *Geological Society, London, Special Publications,* 112**,** 219.

Steffenssen, G., Müller, A., Rosing-Schow, N. & Friis, H. 2019. The distribution and enrichment of scandium in garnets from the Tørdal pegmatites, south Norway, and its economic implications. *The Canadian Mineralogist,* 57**,** 799-801.

Stephens, M. B., Wahlgren, C.-H., Weijermars, R. & Cruden, A. R. 1996. Left-lateral transpressive deformation and its tectonic implications, Sveconorwegian orogen, Baltic Shield, southwestern Sweden. *Precambrian Research,* 79**,** 261-279.

Sunde, Ø., Friis, H., Andersen, T., Trumbull, R. B., Wiedenbeck, M., Lyckberg, P., Agostini, S., Casey, W. H. & Yu, P. 2020. Boron isotope composition of coexisting tourmaline and hambergite in alkaline and granitic pegmatites. *Lithos,* 352-353**,** 105293.

Swensson, E. 1990. Cataclastic rocks along the Nesodden Fault, Oslo Region, Norway: a reactivated Precambrian shear zone. *Tectonophysics,* 178**,** 51-65.

Thomas, R. 2013. *Practical Guide to ICP-MS: A Tutorial for Beginners,* USA, Taylor & Francis Group.

Torsvik, T. H., Smethurst, M. A., Meert, J. G., Van Der Voo, R., Mckerrow, W. S., Brasier, M. D., Sturt, B. A. & Walderhaug, H. J. 1996. Continental break-up and collision in the Neoproterozoic and Palaeozoic — A tale of Baltica and Laurentia. *Earth Science Reviews,* 40**,** 229.

Touret, J. 1971. Le facies granulite en norvege meridionale: I. Les associations minéralogiques. *Lithos,* 4**,** 239-249.

Touret, J. & Nijland, T. 2012. Prograde, peak and retrograde metamorphic fluids and associated metasomatism in upper amphibolite to granulite facies transition zones. *Metasomatism and the Chemical Transformation of Rock.* Springer.

Touret, J. & Olsen, S. N. 1985. Fluid inclusions in migmatites. *In:* Ashworth, J. R. (ed.) *Migmatites.* Boston, MA: Springer.

Tröger, W. E., Bambauer, H. U., Taborszky, F. & Trochim, H. D. 1971. *Optische Bestimmung der gesteinsbildenden Minerale,* Stuttgart, Schweizerbart.

Trumbull, R., Krienitz, M.-S., Gottesmann, B. & Wiedenbeck, M. 2008. Chemical and boron-isotope variations in tourmalines from an S-type granite and its source rocks: the Erongo granite and tourmalinites in the Damara Belt, Namibia. *Contributions to Mineralogy and Petrology,* 155**,** 1-18.

Trumbull, R. B., Beurlen, H., Wiedenbeck, M. & Soares, D. R. 2013. The diversity of B-isotope variations in tourmaline from rare-element pegmatites in the Borborema Province of Brazil. *Chemical Geology,* 352**,** 47-62.

Trumbull, R. B. & Slack, J. F. 2018. Boron isotopes in the continental crust: granites, pegmatites, felsic volcanic rocks, and related ore deposits. *Boron Isotopes.* Springer.

Trumbull, R. B., Slack, J. F., Krienitz, M. S., Belkin, H. E. & Wiedenbeck, M. 2011. Fluid sources and metallogenesis in the Blackbird Co-Cu-Au-Bi-Y-REE district, Idaho, U.S.A.: Insights from major-element and boron isotopic compositions of tourmaline. *Canadian Mineralogist,* 49**,** 225-244.

Uebel, P. J. 1977. Internal structure of pegmatites, its origin and nomenclature. *Neues Jarbuch für Mineralogie Abhandlungen,* 131**,** 83-113.

Van Hinsberg, V., Henry, D. J. & Marschall, H. 2011a. Tourmaline: An ideal indicator of its host environment. *Canadian Mineralogist,* 49**,** 1-16.

Van Hinsberg, V. J. 2011. Preliminary experimental data on trace-element partitioning between tourmaline and silicate melt. *The Canadian Mineralogist,* 49**,** 153-163.

Van Hinsberg, V. J., Henry, D. J. & Dutrow, B. L. 2011b. Tourmaline as a Petrologic Forensic Mineral: A Unique Recorder of Its Geologic Past. *Elements,* 7**,** 327-332.

Van Hinsberg, V. J. & Schumacher, J. C. 2007. Intersector element partitioning in tourmaline: a potentially powerful single crystal thermometer. *Contributions to Mineralogy and Petrology,* 153**,** 289-301.

Van Hinsberg, V. J. & Schumacher, J. C. 2011. Tourmaline as a petrogenetic indicator mineral in the Haut-Allier metamorphic suite, Massif Central, France. *The Canadian Mineralogist,* 49**,** 177-194.

Van Hinsberg, V. J. V., Franz, G. & Wood, B. J. Determining subduction-zone fluid composition using a tourmaline mineral probe. 2017.

Vander Auwera, J., Bolle, O., Bingen, B., Liégeois, J. P., Bogaerts, M., Duchesne, J. C., De Waele, B. & Longhi, J. 2011. Sveconorwegian massif-type anorthosites and related granitoids result from post-collisional melting of a continental arc root. *Earth-Science Reviews,* 107**,** 375-397.

Versteeve, A. J. 1974. Isotope geochronology in the high-grade metamorphic Precambrian of southwestern Norway. Rijksuniversiteit Utrecht (Netherlands).

Viola, G., Bingen, B. & Solli, A. 2016. *Berggrunnskart: Kongsberg litotektoniske enhet, Kongsberg - Modum - Hønefoss M 1:100 000*. Norges geologiske undersøkelse.

Viola, G., Henderson, I., Bingen, B. & Hendriks, B. 2011. The Grenvillian–Sveconorwegian orogeny in Fennoscandia: Back-thrusting and extensional shearing along the "Mylonite Zone". *Precambrian Research,* 189**,** 368-388.

Visser, D. & Senior, A. 1990. Aluminous reaction textures in orthoamphibole-bearing rocks: the pressure–temperature evolution of the high-grade Proterozoic of the Bamble sector, south Norway. *Journal of Metamorphic Geology,* 8**,** 231-246.

Von Goerne, G., Franz, G. & Wirth, R. 1999. Hydrothermal synthesis of large dravite crystals by the chamber method. *European Journal of Mineralogy,* 11**,** 1061-1077.

Watenphul, A., Burgdorf, M., Schlüter, J., Horn, I., Malcherek, T. & Mihailova, B. 2016. Exploring the potential of Raman spectroscopy for crystallochemical analyses of complex hydrous silicates: II. Tourmalines. *American Mineralogist,* 101**,** 970-985.

Webber, K. L., Simmons, W. B., Falster, A. U. & Hanson, S. L. 2019. Anatectic pegmatites of the Oxford County pegmatite field, Maine, USA. *The Canadian Mineralogist,* 57**,** 811-815.

Werding, G. & Schreyer, W. 1984. Alkali-free tourmaline in the system MgO-Al2O3-B2O3-SiO2-H2O. *Geochimica et Cosmochimica Acta,* 48**,** 1331-1344.

Whalen, J. B., Currie, K. L. & Chappell, B. W. 1987. A-type granites: geochemical characteristics, discrimination and petrogenesis. *Contributions to Mineralogy and Petrology,* 95**,** 407-419.

Williams, P. A., Hatert, F., Pasero, M. & Mills, S. J. 2010. New minerals and nomenclature modifications approved in 2010. *Mineralogical Magazine,* 74**,** 859-862.

Williamson, B. J., Spratt, J., Adams, J. T., Tindle, A. G. & Stanley, C. J. 2000. Geochemical Constraints from Zoned Hydrothermal Tourmalines on Fluid Evolution and Sn Mineralization: an Example from Fault Breccias at Roche, SW England. *Journal of Petrology,* 41**,** 1439-1453.

Wolf, M. B. & London, D. 1997. Boron in granitic magmas: stability of tourmaline in equilibrium with biotite and cordierite. *Contributions to Mineralogy and Petrology,* 130**,** 12-30.

Xiao, J., Xiao, Y. K., Jin, Z. D., He, M. Y. & Liu, C. Q. 2013. Boron isotope variations and its geochemical application in nature. *Australian Journal of Earth Sciences,* 60**,** 431-447.

Yang, S.-Y., Jiang, S.-Y., Zhao, K.-D., Dai, B.-Z. & Yang, T. 2015. Tourmaline as a recorder of magmatic–hydrothermal evolution: an in situ major and trace element analysis of tourmaline from the Qitianling batholith, South China. *Contributions to Mineralogy and Petrology,* 170.

Appendix A

Appendix A Table 1 Extended sample list

Sample number	Locality	Rock/ Mineral type	Location within pegmatite	UTM Zone	UTM E	UTM N	Preparation	Analyses	Sample source
20252	Lindvikskollen	Tourmaline	Core	-	-	-	Epoxy mount 41/64	EPMA, LA-ICP-MS, SIMS (B-isotope)	NHM collection
20241	Tangen	Tourmaline	Core	32 V	520421	6525815	Epoxy mount 41/64	EPMA, LA-ICP-MS, SIMS (B-isotope)	NHM collection
20216	Havredal	Tourmaline	Intermediate zone	32V	532350	6535388	Epoxy mount 41/64	EPMA, LA-IP-MS, SIMS (B-isotope)	NHM collection
13051920	Dalane	Tourmaline	Intermediate zone	32V	513750	6527923	Epoxy mount 41/64	EPMA, LA-ICP-MS, SIMS (B-isotope)	NHM collection
20091	Ramfoss	Tourmaline	-	32V	c. 545400	c. 6661200	Epoxy mount 41/64	EPMA, LA-ICP-MS, SIMS (B-isotope)	NHM collection
05061804	Spro	Tourmaline	Host rock Gneiss	32V	589119	6626473	Epoxy mount 41/64	EPMA, LA-ICP-MS, SIMS (B-isotope)	NHM collection
12062004	Lindvikskollen W mine	Coarse tourmaline in quartz	Core	32 V	521492	6525135	Thick section	EPMA, LA-ICP-MS	Field
12062007	Lindvikskollen W mine	Fine grained, collomorph tourmaline	Intermediate zone	32 V	521496	6525125	Thick section	EPMA, LA-ICP-MS	Field
12062008	Lindvikskollen W mine	Large tourmaline crystal	Intermediate zone	32 V	521496	6525125	Thick section	EPMA, LA-ICP-MS	Field
12062009	Lindvikskollen W mine	Large tourmaline	Wall zone 0.5 m from contact	32 V	521493	6525117	Epoxy mount 42	EPMA, LA-ICP-MS	Field
12062014	Lindvikskollen W mine	Bulk wall zone	Wall zone	32 V	521493	6525117	Crushing	WR analysis	Field
12062015	Lindvikskollen W mine	Amphibolite	Host rock	32V	521490	6525111	Thick section; crushing	EPMA, LA-ICP-MS WR analysis	Field

12062016	Lindvikskollen W mine	Albitite with tourmaline	Host rock	32V	521487	6525110	Thick section; crushing	EPMA, LA-ICP-MS WR analysis	Field
12062018	Lindvikskollen W mine	Tourmaline	Core (not *in situ*)	32V	521492	6525135	Epoxy mount 44	EPMA, LA-ICP-MS	Field
12062020	Lindvikskollen W mine	Isometric tourmaline in amphibolite	Host rock	32 V	521487	6525110	Epoxy mount 43	EPMA, LA-ICP-MS	Field
12062021	Lindvikskollen E mine	Large tourmaline in K-feldspar	Intermediate zone	32 V	521709	6525139	Epoxy mount 43	EPMA, LA-ICP-MS	Field
12062022	Lindvikskollen E mine	Large tourmaline in quartz	Core	32 V	521709	6525139	Epoxy mount 45	EPMA, LA-ICP-MS	Field
12062023	Lindvikskollen E mine	Small tourmaline in quartz	Core	32 V	521709	6525139	Epoxy mount 46	EPMA, LA-ICP-MS	Field
12062024	Lindvikskollen E mine	Small tourmalines in K-feldspar megacryst	Intermediate zone	32 V	521709	6525139	Thick section	EPMA, LA-ICP-MS	Field
12062025	Lindvikskollen E mine	Small tourmalines in veinlets in K-feldspar	Intermediate zone	32 V	521709	6525139	Thick section	EPMA, LA-ICP-MS	Field
12062026	Lindvikskollen rutile mine tailings	Mineralized albitite (rutile-rich)	Host rock	32 V	52139	6525180	Thick section; crushing	EPMA, LA-ICP-MS WR analysis	Field
12062027	Lindvikskollen rutile mine tailings	Non-mineralized albitite (rutile-poor)	Host rock	32 V	52139	6525180	Thick section; crushing	WR analysis	Field
12062029	Lindvikskollen road cut	Monzonitic gneiss	Host rock	32 V	521360	6525279	Thick section; crushing	WR analysis	Field
12062030	Lindvikskollen road cut	Tourmaline in granitic dyke	Host rock	32 V	521360	6525279	Thick section	EPMA, LA-ICP-MS	Field
12062031	Lindvikskollen road cut	Tourmaline-bearing Granite dyke	Host rock	32 V	521360	6525279	Crushing	WR analysis	Field
690a	Spro	Large tourmaline in quartz and K-feldspar	Pegmatite	-	-	-	Epoxy mount	EPMA, LA-ICP-MS	NHM collection
690b	Spro	Tourmaline in quartz	Pegmatite	-	-	-	Epoxy mount	EPMA, LA-ICP-MS	NHM collection
690c	Spro	Fine-grained tourmaline in albite vein	Pegmatite	-	-	-	Epoxy mount	EPMA, LA-ICP-MS	NHM collection
20160	Spro	Large tourmaline in quartz	Pegmatite	-	-	-	Epoxy mount	EPMA	NHM collection
18081715	Spro	Fine tourmaline in albite	Pegmatite	32 V	589134	6626548	Epoxy mount	EPMA	NHM collection

Appendix B

Standard and Reference Samples

Table A: LA-ICP-MS

Tables B: SIMS

Appendix B Table 1 Tourmaline LA-ICP-MS Standard and Reference samples Average, Standard deviation (SD) and Standard error of Mean (StEM)

LA-ICP-MS Standard and Reference samples									
Element ppm	NIST SRM 610			BCR-2G-07			Tourmaline-Black		
	Average	SD	StEM	Average	SD	StEM	Average	SD	StEM
Li	470.62	39.94	6.48	8.93	0.90	0.24	5.93	0.79	0.32
Be	477.05	37.27	6.05	2.41	0.20	0.05	2.11	1.15	0.47
Na	99493.84	2480.62	402.41	23230.57	794.29	212.28	15512.46	1647.85	672.73
Mg	432.63	31.01	5.03	21084.35	1624.80	434.25	37927.06	5181.22	2115.22
Al	10321.20	768.21	124.62	80479.27	4195.30	1121.24	187589.75	18760.03	7658.75
Si	325806.05	0.07	0.01	254287.02	0.04	0.01	168278.17	0.004	0.002
P	411.33	28.08	4.55	1409.26	122.62	32.77	21.85	1.75	0.72
K	463.68	27.05	4.39	14296.80	988.35	264.15	467.52	49.64	20.27
Ca	81680.69	5835.68	946.67	53649.77	4023.72	1075.38	5803.70	3379.46	1379.66
Sc	457.11	44.68	7.25	36.23	2.77	0.74	17.38	1.55	0.63
Ti	451.52	42.37	6.87	14257.60	484.79	129.57	3748.71	865.46	353.32
V	450.42	26.39	4.28	430.58	25.02	6.69	60.78	15.67	6.40
Cr	407.78	16.34	2.65	26.54	3.79	1.01	48.67	6.74	2.75
Mn	443.20	18.84	3.06	1547.01	49.86	13.32	1186.84	804.40	328.39
Co	409.42	15.97	2.59	37.62	1.83	0.49	19.42	7.73	3.15
Ni	458.21	14.48	2.35	10.61	6.43	1.72	36.08	2.92	1.19
Cu	441.42	12.42	2.02	20.68	1.03	0.28	3.67	0.46	0.19
Zn	464.08	46.23	7.50	150.10	19.46	5.20	173.79	92.26	37.67
Ga	432.96	16.30	2.64	107.64	16.22	4.34	70.84	15.42	6.30
Rb	426.69	26.44	4.29	46.47	3.61	0.96	0.03	0.02	0.01
Sr	516.75	40.92	6.64	362.35	24.26	6.48	12.68	9.85	4.02
Y	464.01	42.67	6.92	36.68	3.02	0.81	0.07	0.05	0.02
Zr	449.74	40.67	6.60	198.79	15.35	4.10	0.27	0.06	0.02
Nb	466.73	38.88	6.31	12.87	0.89	0.24	0.38	0.17	0.07
Mo	417.80	26.23	4.25	245.88	20.28	5.42	0.05	0.02	0.01
Sn	430.55	25.83	4.19	2.22	0.20	0.05	1.77	0.25	0.10
Sb	396.86	26.89	4.36	0.27	0.05	0.01	0.01	0.005	0.002
Cs	367.32	27.00	4.38	1.13	0.09	0.02	0.01	0.001	0.001
Ba	454.08	40.93	6.64	716.33	55.64	14.87	0.27	0.24	0.10
La	442.48	42.52	6.90	27.74	2.20	0.59	1.54	0.56	0.23
Ce	455.15	37.92	6.15	54.86	4.69	1.25	2.50	1.27	0.52
Pr	449.46	37.56	6.09	7.32	0.51	0.14	0.24	0.15	0.06
Nd	431.04	36.76	5.96	30.78	1.96	0.52	0.71	0.47	0.19
Sm	454.22	39.61	6.43	7.18	0.49	0.13	0.12	0.09	0.04
Eu	447.95	37.60	6.10	2.13	0.16	0.04	0.12	0.10	0.04
Lu	441.19	42.40	6.88	0.55	0.04	0.01	0.003	0.001	0.001
Ta	447.63	40.41	6.56	0.82	0.23	0.06	0.17	0.10	0.04
W	444.81	27.40	4.44	0.48	0.05	0.01	0.01	0.004	0.002
Pb	428.26	34.28	5.56	9.85	1.04	0.28	1.99	0.68	0.28
Th	463.84	58.00	9.41	6.74	0.67	0.18	0.003	0.004	0.002
U	468.08	56.15	9.11	1.74	0.19	0.05	0.31	0.60	0.24

Appendix B Table 2 - B isotope analysis of the standard samples used for the calculation of $\delta^{11}B$ of the samples. IMF: initial mass function.

Sample		**11B/10B**	**1 σ (%)**	**IMF**	**11/10B corrected**	**$\delta^{11}B$**
Schorl	Schorl@1	3.9031	0.0118	0.9774	3.998	-11.2
	Schor-g2l@2	3.9015	0.0098	0.9771	3.997	-11.6
	Schor-g2l@3	3.9013	0.0118	0.9770	3.997	-11.6
	Schorl-3g@1	3.9009	0.0093	0.9769	3.996	-11.7
	Schorl-3g@2	3.9011	0.0143	0.9770	3.996	-11.7
	Schorl-3g@3	3.8990	0.0097	0.9764	3.994	-12.2
	Schorl-3g@4	3.8991	0.0073	0.9765	3.994	-12.2
	Schorl-3g@5	3.8990	0.0075	0.9764	3.994	-12.2
	Schorl-3g@6	3.9000	0.0085	0.9767	3.995	-11.9
	Schorl-g1@7	3.9016	0.0083	0.9771	3.997	-11.5
	Schorl-g1@8	3.9021	0.0135	0.9772	3.997	-11.4
	Schorl-g1@9	3.9003	0.0061	0.9767	3.996	-11.9
	Schorl-g1@10	3.9003	0.0074	0.9768	3.996	-11.9
Mean				0.9769		-11.8
Repeat permil	0.32					
		11B/10B	**1 σ (%)**	**Delta Inst**	**11/10B corrected**	**$\delta^{11}B$**
Dravite	Dravite-g4@1	3.9190	0.0109	0.9756	4.0147	-7.1
	Dravite-g4@2	3.9184	0.0138	0.9755	4.0141	-7.3
	Dravite-g3@3	3.9175	0.0100	0.9753	4.0133	-7.5
	Dravite-g3@4	3.9175	0.0102	0.9753	4.0132	-7.5
	Dravite-g3@5	3.9174	0.0117	0.9752	4.0131	-7.5
	Dravite-g3@6	3.9171	0.0103	0.9752	4.0128	-7.6
	Dravite-g3@7	3.9160	0.0080	0.9749	4.0117	-7.9
	Dravite-g3@8	3.9169	0.0095	0.9751	4.0126	-7.7
	Dravite-g3@9	3.9194	0.0131	0.9757	4.0152	-7.0
	Dravite-g4@10	3.9206	0.0106	0.9760	4.0163	-6.7
	Dravite-g3@11	3.9182	0.0091	0.9754	4.0139	-7.3
	Dravite-g4@12	3.9180	0.0075	0.9754	4.0137	-7.4
				0.9754		-7.4
Mean						
Repeat permil	0.31					
		11B/10B	**1 σ (%)**	**Delta Inst**	**11/10B corrected**	**$\delta^{11}B$**
Elbaite	Elbaite-g2@1	3.8939	0.0143	0.9731	4.0000	-10.8
	Elbaite-g2@2	3.8939	0.0123	0.9731	4.0000	-10.8
	Elbaite-g1@3	3.8991	0.0138	0.9744	4.0054	-9.5
	Elbaite-g1@4	3.8983	0.0110	0.9742	4.0045	-9.7
	Elbaite-g2@6	3.8944	0.0088	0.9733	4.0005	-10.7
	Elbaite-g2@7	3.8931	0.0070	0.9729	3.9991	-11.0
	Elbaite-g2@8	3.8935	0.0100	0.9730	3.9995	-10.9
	Elbaite-g2@9	3.8937	0.0073	0.9731	3.9998	-10.8
	Elbaite-g2@10	3.8967	0.0159	0.9738	4.0029	-10.1
	Elbaite-g1@11	3.8992	0.0171	0.9745	4.0055	-9.4
	Elbaite-g2@12	3.8935	0.0053	0.9730	3.9996	-10.9
	Elbaite-g1@13	3.8939	0.0062	0.9731	4.0000	-10.8
Mean				0.9735		-10.4
Repeat permil	0.61					

Appendix C

Analytical Results

Table 3: SIMS Appendix C Table 1 - Tourmaline B isotope results analysed on the SIMS.

Sample		11B/10B	1σ (%)	11/10B corrected	Int. Precision ‰	$\delta^{11}B$
Lindvikskollen	1	3.9433	0.0068	4.0397	0.07	-1.0
	2	3.9413	0.0082	4.0376	0.08	-1.5
	3	3.9411	0.0099	4.0374	0.10	-1.5
	4	3.9398	0.0087	4.0361	0.09	-1.9
	5	3.9429	0.0083	4.0392	0.08	-1.1
Average						-1.4
SD						0.32
Tangen	1	3.9432	0.0096	4.0395	0.10	-1.0
	2	3.9432	0.0083	4.0395	0.08	-1.0
	3	3.9428	0.0071	4.0391	0.07	-1.1
	4	3.9416	0.0098	4.0379	0.10	-1.4
	5	3.9417	0.0093	4.0380	0.09	-1.4
	6	3.9419	0.0088	4.0382	0.09	-1.3
	7	3.9416	0.0072	4.0379	0.07	-1.4
	8	3.9423	0.0103	4.0387	0.10	-1.2
	9	3.9416	0.0064	4.0379	0.06	-1.4
Average						-1.3
SD						0.17
Dalane	1	3.9507	0.0131	4.0472	0.13	0.9
	2	3.9512	0.0134	4.0477	0.13	1.0
	3	3.9498	0.0074	4.0463	0.07	0.7
	4	3.9501	0.0070	4.0466	0.07	0.7
	5	3.9503	0.0116	4.0468	0.12	0.8
	6	3.9497	0.0085	4.0462	0.08	0.6
	7	3.9497	0.0083	4.0462	0.08	0.6
Average						0.8
SD						0.14
Havredal	1	3.9544	0.0094	4.0510	0.09	1.8
	2	3.9553	0.0076	4.0519	0.08	2.0
	3	3.9561	0.0085	4.0527	0.08	2.3
	4	3.9557	0.0090	4.0523	0.09	2.1
	5	3.9565	0.0093	4.0532	0.09	2.4
Average						2.1
SD						0.21
Ramfoss	1	3.9861	0.0100	4.0835	0.10	9.9
	2	3.9853	0.0089	4.0827	0.09	9.7
	3	3.9857	0.0129	4.0831	0.13	9.8
	4	3.9855	0.0109	4.0828	0.11	9.7
	5	3.9861	0.0101	4.0835	0.10	9.9
	6	3.9848	0.0083	4.0822	0.08	9.5
Average						9.7
SD						0.13
Spro Gneiss	1	3.8956	0.0102	3.9908	0.10	-13.1
	2	3.8964	0.0114	3.9916	0.11	-12.9
	3	3.8937	0.0096	3.9888	0.10	-13.5
	4	3.8942	0.0093	3.9893	0.09	-13.4
	5	3.8935	0.0116	3.9886	0.12	-13.6
	6	3.8889	0.0092	3.9839	0.09	-14.8
	7	3.8952	0.0105	3.9904	0.11	-13.2
	8	3.8949	0.0115	3.9901	0.12	-13.2
Average						-13.5
SD						0.55

Appendix D

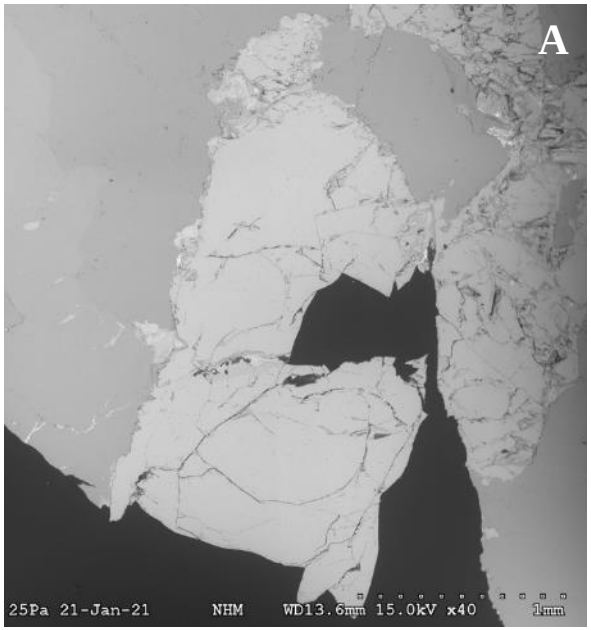

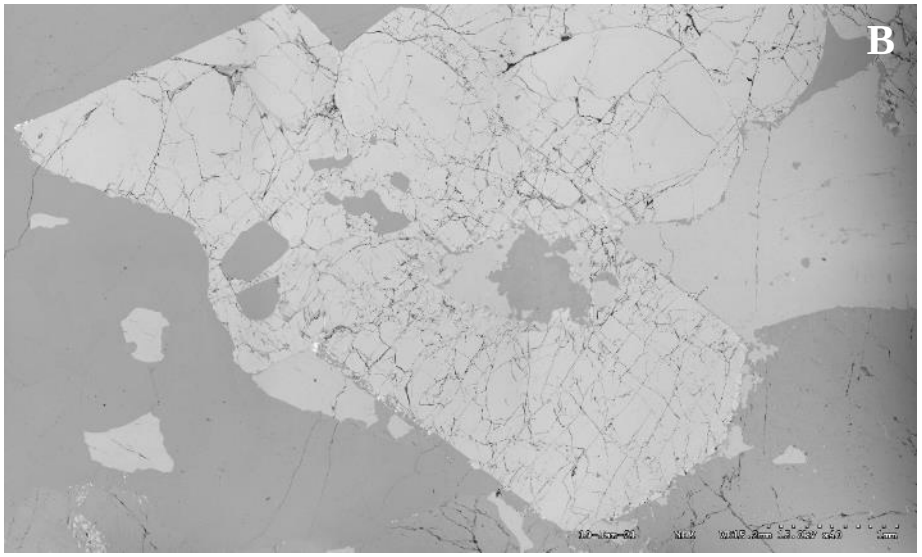

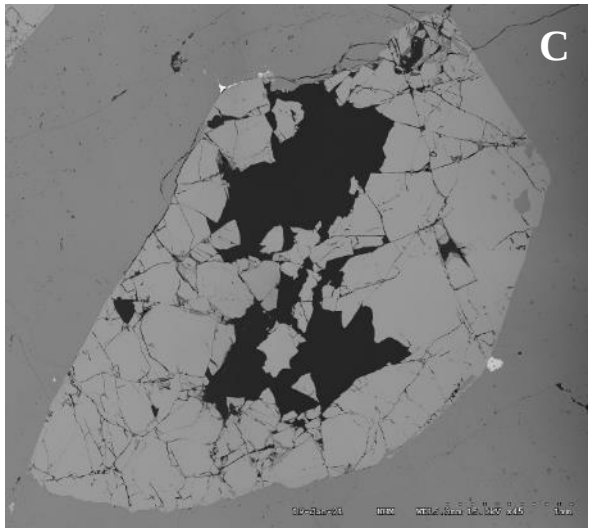

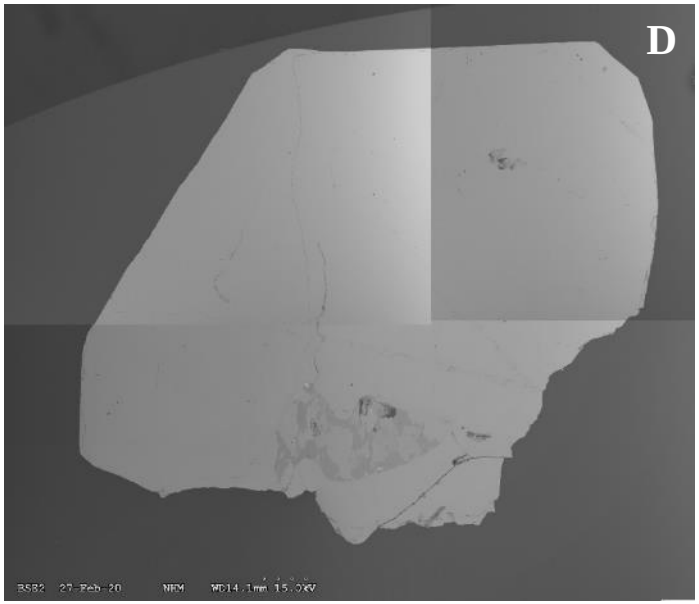

SEM Images

A – Lindvikskollen pegmatite tourmaline of the wall zone (12062009).

B – Lindvikskollen pegmatite tourmaline of the intermediate zone (12062024).

C - Lindvikskollen pegmatite tourmaline of the core zone (12062023).

D - Lindvikskollen pegmatite tourmaline of the core zone (20252)

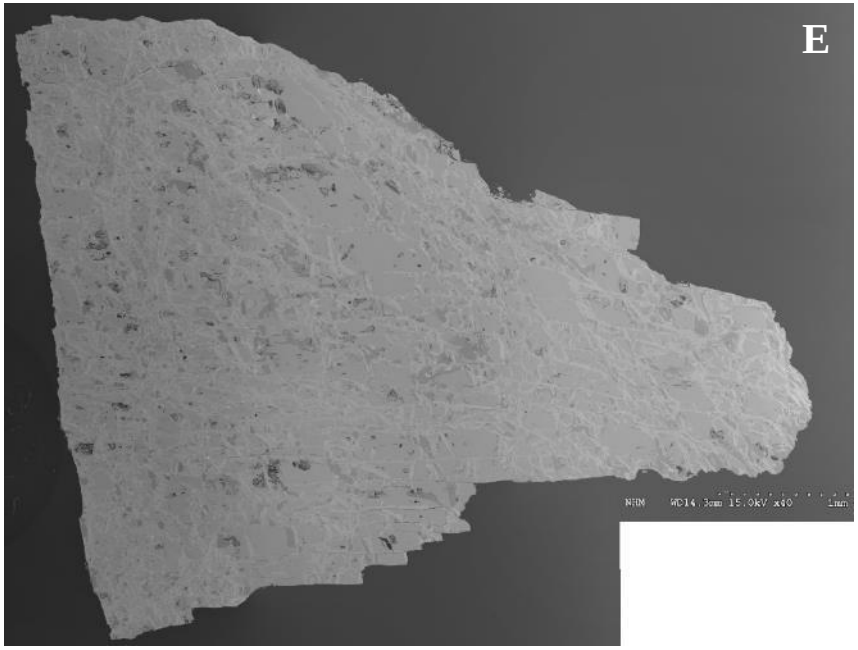

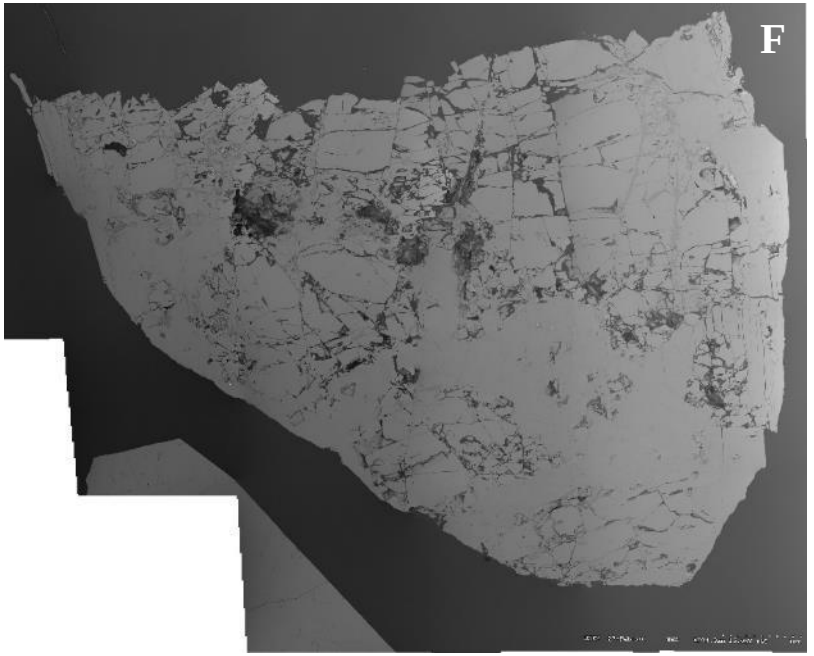

E – Tangen pegmatite tourmaline (20241).

F – Dalane pegmatite tourmaline (20216).

G – Havredal pegmatite tourmaline (13051920).

H – Ramfoss pegmatite tourmaline (20091)

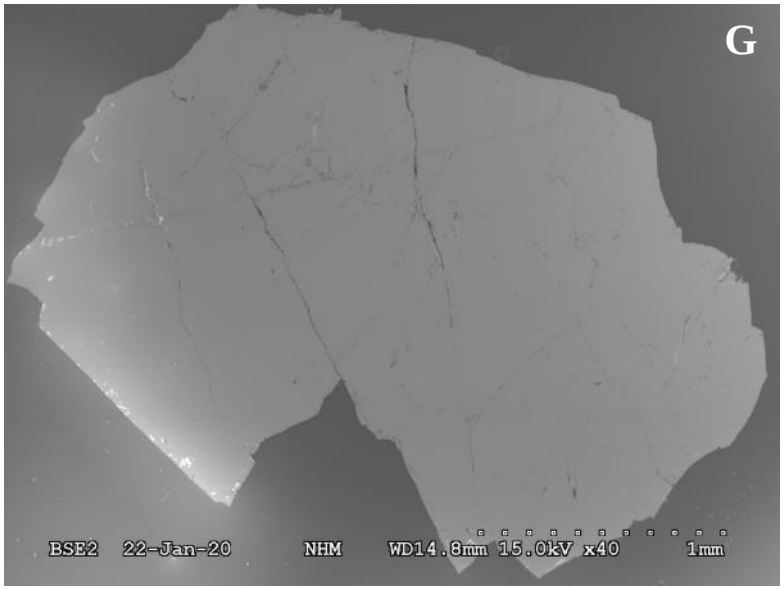

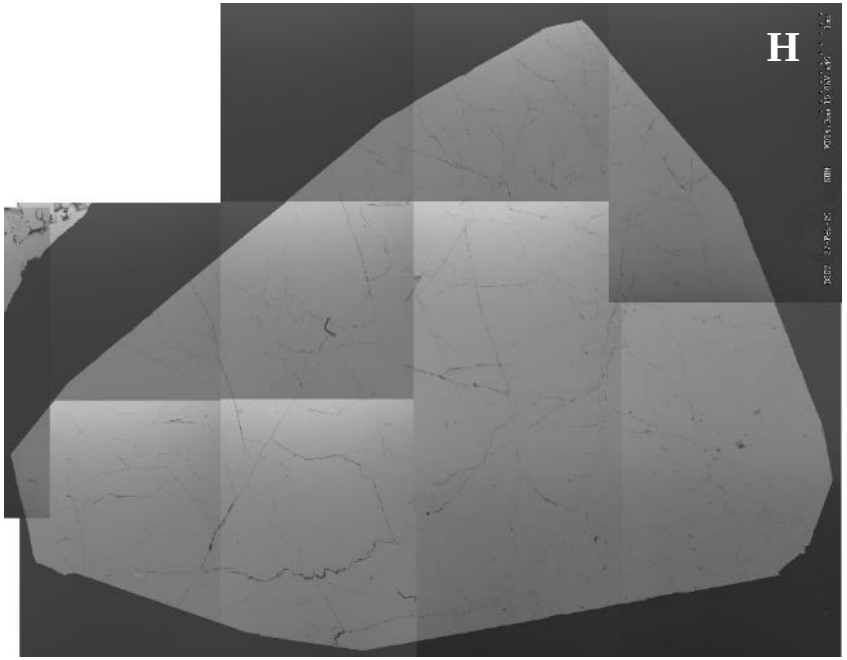

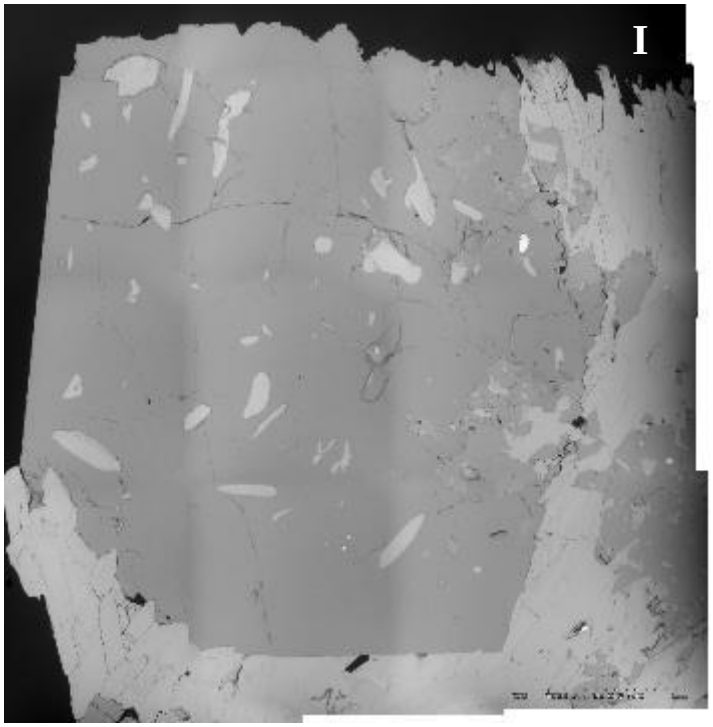

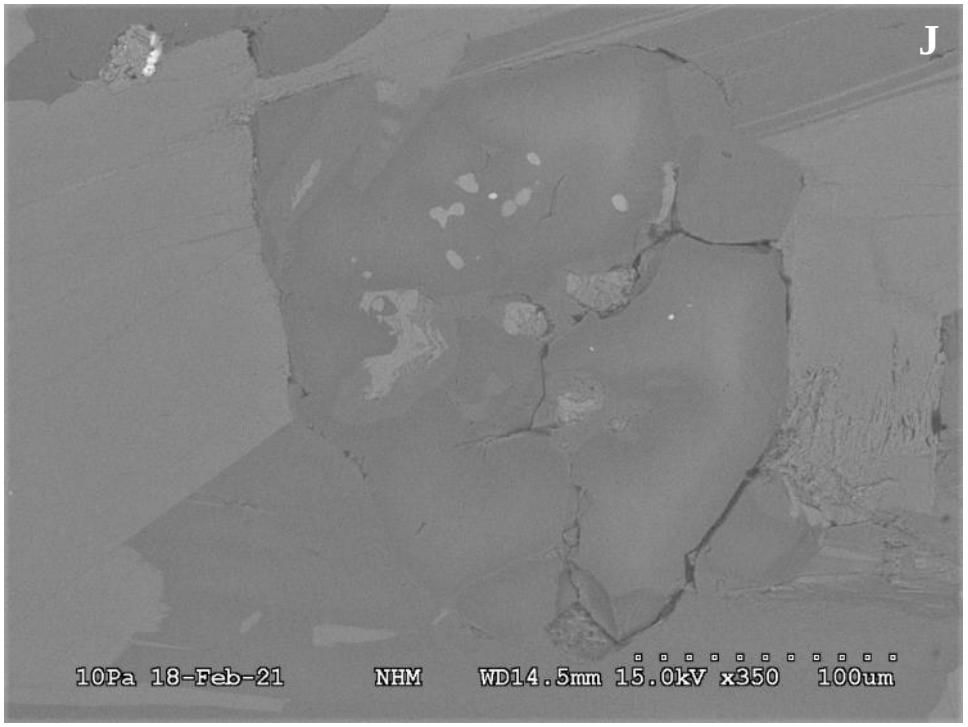

I – Tourmaline from the Lindvikskollen host rock, metagabbro (12062020).

J – Tourmaline from the Spro host rock, gneiss (05061804).